Spin and Thermal Transport in Lateral Spin Valves

Kathryn Moran
University of Leeds
School of Physics and Astronomy

Submitted in accordance with the requirements for the degree of
Doctor of Philosophy

July, 2021

Intellectual Property Statement

The candidate confirms that the work submitted is her own and that appropriate credit has been given where reference has been made to the work of others.

The right of Kathryn Moran to be identified as Author of this work has been asserted by her in accordance with the Copyright, Designs and Patents Act 1988.

Acknowledgements

I would like to wholeheartedly thank my supervisors, Prof. Bryan J Hickey, Dr Olga Kazakova and Dr Gavin Burnell; a triumvirate without whom this work would not have been possible. Their patience, understanding and advice throughout the rollercoaster ride of my PhD has been invaluable. I am particularly grateful to Bryan for his willingness to listen to my frequently incoherent ramblings about failed samples, broken equipment and the value of Friday afternoon Condensed Matter Group meetings. I am also eternally grateful for the support and advice from Dr. Mannan Ali; not to mention the first-class training on all things lab related and the much needed coffee breaks. Despite my best efforts to break every piece of sensitive equipment within the Laboratory over the past four years, there appeared to be nothing that Mannan couldn't resolve. I would also like to thank Dr. Mark Rosamond, he performed all of the electron beam lithography for the samples in this work and was a veritable font of clean room knowledge upon which I was only too glad draw.

Behind every successful academic or researcher there is invariably an army of highly skilled technical support staff. I am no different, and I am all too aware that my efforts would have come to nothing if it hadn't been for their expertise and assistance. In no particular order I therefore wish to place on record my thanks to: David Chapman; John Turton; Brian Gibbs; Luke Bone; Stuart Weston; Phillip Thornton; Richard Oliver; and, Adam Foster.

I would also like to thank Dr Joe Batley for his help and training at the beginning of this project. Special thanks to Dr Georgios Stefanou for his constant help, discussions and chocolate; I am not sure I could have survived my PhD with my sanity intact without you. A huge thanks to Gregory Simon, Jack Adams, Ben Steele, Craig Knox, Josh Gretton, Amy Westerman and Shoug Alghamdi for listening to me complain over the years when things would get difficult. I am grateful to all members of the Condensed Matter Group who have given me advice, training and support.

Finally, I would like to thank my parents for their unwavering support and encouragement throughout.

Abstract

This thesis is focused upon spin and thermal transport in lateral spin valves (LSVs) composed of the technologically relevant pairing Cu/$Co_{70}Fe_{30}$. Spin injection and diffusion was examined in shadow deposited LSVs with different CoFe thicknesses. High spin polarisations were obtained compared to previous CoFe/Cu LSVs fabricated with a two-step method. It was found that the spin diffusion length was strongly affected by the amount of CoFe deposited, as a result of magnetic impurities introduced during the deposition procedure.

Thermal background voltages always accompany spin transport in an electrical spin injection technique. In the second part of this thesis the sources of thermal voltages arising in LSVs and their dependence on temperature and length are reported.

Finally, measurements of the spin diffusion lengths of ferromagnets are lacking in the literature, particularly those in nanowire structures as a function of temperature. In the final part of this thesis, a spin absorption technique is used to extract the spin diffusion length of $Co_{70}Fe_{30}$ as a function of temperature, confirming that Elliott-Yafet spin relaxation is the dominant mechanism in this alloy.

Contents

LIST OF FIGURES

List of Tables

Abbreviations

FM	Ferromagnet
NM	Non-magnetic
GMR	Giant Magnetoresistance
NLIV	Non-Local IV
TMR	Tunneling Magnetoresistance
LSV	Lateral Spin Valve
MI	Magnetic Impurity
EBL	Electron Beam Lithography
MMA	Methyl Methacrylate
PMMA	Poly Methyl Methacrylate
SEM	Scanning Electron Microscopy
PVD	Physical Vapour Deposition
SAD	Spin Absorption Device
RF	Radio Frequency
AFM	Atomic Force Microscopy
RFI	Radio Frequency Interference
PCB	Printed Circuit Board
CPP	Current Perpendicular-to-Plane
P	Parallel
AP	Anti-Parallel
EY	Elliott-Yafet
SOC	Spin-Orbit Coupling
BG	Bloch-Grüneisen
VBS	Virtual Bound State
UHV	Ultra High Vacuum
HV	High Vacuum
IPA	Isopropyl Alcohol
LOR	Lift Off Resist
VTI	Variable Temperature Insert
NMP	Micro Deposit Remover 1165
DC	Direct Current
AC	Alternating Current
DUT	Device Under Test
EI	Electromagnetic Interference
XRR	X-Ray Reflectivity

CHAPTER 1

Introduction

While the electronic charge has been widely exploited over the last century to revolutionise our everyday lives, it was not until much more recently that the other fundamental property of the electron, its spin, was realised to be much more useful than just a quantum mechanical 'quirk' of matter. Even prior to the 1897 discovery of the electron itself, spin-dependent transport had already been observed in ferromagnets (FM); most notably, the 1857 discovery of anisotropic magnetoresistance (AMR) by Lord Kelvin [17] and the anomalous Hall effect by E. H. Hall in 1881 [18]. However, it was not until the 1980s with the advent of thin film growth techniques, that discoveries of larger spin-dependent effects emerged and interest in spin related phenomena began to gain traction. Perhaps the most important milestone, widely acknowledged to be the genesis of contemporary spin related research, was the 1988 discovery of giant magnetoresistance (GMR) by Albert Fert and Peter Grünberg [19, 20]. In metallic thin film multilayers with alternating FM and non-magnetic (NM) layers a large magnetoresistance ($\approx 10\%$) was observed upon reversing the magnetisation of the FM layers between the parallel (P) and anti-parallel (AP) states. In the P state, only minority spin electrons were scattered and the total resistance was low, whereas in the AP state scattering of both majority and minority spins led to a high resistance. These multilayer structures, otherwise known as GMR spin valves, quickly found commercial applications as magnetic sensors in the car industry and as read heads in hard disk drives [21, 22].

Inspired by this early commercial success, an explosion in experimental and theoretical work ensued and birthed the field of spin electronics, dubbed 'spintronics', which aims to harness the power of the electron's spin to create powerful devices with novel functionalities and improved power consumption. All spintronic devices that have found commercial success so far utilise the spin polarised charge current. Although successful, these devices still suffer from the detrimental effects of Joule heating that lies at the root of the recent slowing in Moore's law. Looking forward, the next generation of spintronic devices are conceived to harness the pure diffusive spin current; a diffusion of spin without charge, theoretically free from Joule heating [23–25]. The cornerstone of pure spin current study is the lateral spin valve (LSV), which generally consists of two spatially separated FM electrodes bridged by a relatively long ($\approx$ µm) NM transport channel. The lateral geometry provides a unique opportunity to study spin injection and the evolution of pure spin currents over long length scales without spurious signals from charge currents.

In an initial proof of concept in 1985, Johnson and Silsbee [26] successfully demonstrated non-local spin injection from an FM into a 50 µm thick Al bar; although, owing to the relatively large dimensions of the device, the output spin signals were small ($\approx$ 10pV). By 2001, advancements in lithographic techniques allowed for the fabrication of nanoscale LSVs, which showed a dramatic signal enhancement to a few µV at room temperature [27] and led to a cascade of LSV research in the following decades. Since then, spin injection into different metals [12, 28–31], semiconductors [32, 33] and superconductors [34–36] has been achieved. Novel methods of spin injection such as thermal spin injection [37–39] and spin pumping [40] have also been demonstrated. Fabrication methods have also improved; most notably, the development of the shadow deposition technique enables deposition of the entire LSV in a single vacuum cycle - presenting clear advantages over multi-step techniques. The broad aims of LSV research are twofold: the optimization of spin injection and transport.

This thesis focuses on spin and thermal transport metallic LSVs. All devices were fabricated through a shadow deposition method to achieve high-quality transparent FM/NM interfaces. Cu was used throughout as the NM transport channel due to its low resistivity, low spin-orbit coupling and consequently long spin diffusion length. CoFe was an ideal candidate for the FM given its soft magnetic properties, high Curie temperature and high intrinsic spin polarisation (α_{FM}). For metallic LSVs with transparent interfaces, the spin injection efficiency for a particular FM is determined by its spin and charge transport parameters, namely, the spin diffusion length (λ_{FM}), resistivity (ρ_{FM}) and α_{FM} [41, 42]. Compared to the most widely used FM, Py, all three transport parameters tend to be higher in CoFe, indicating superior spin injection properties. This was demonstrated experimentally in $\mathrm{Co_{60}Fe_{40}}$/Cu LSVs, where the spin signals were increased four-fold compared to equivalent Py devices [43]. Although CoFe alloys are perfect candidates for future device applications, very few LSV studies have employed CoFe thus far. The three completed CoFe studies [42–44] only presented results at either room or low temperatures, so limited information is available on the temperature dependence of spin transport. This information, however, is vital to understand the sources of spin relaxation. In this work, we employ a slightly different alloy composition to previous studies, specifically $\mathrm{Co_{70}Fe_{30}}$, based on the observation that in magnetic tunnel junctions (MTJs) slightly more Co-rich electrodes were found to exhibit higher magnetoresistances [45].

In Chapter 4, spin transport in two sets of $Co_{70}Fe_{30}$/Cu LSVs with different $Co_{70}Fe_{30}$ thicknesses are compared, with a view to maximising spin diffusion and spin injection. Shadow evaporated $Co_{70}Fe_{30}$/Cu LSVs have not been investigated thus far, and no measurements of the temperature dependence of spin transport in these devices exist. Furthermore, in other CoFe/Cu LSVs (with similar CoFe compositions) fabricated via a two-step technique reported spin polarisations were low (0.2-0.5)[43, 44]; this may be improved through the use of a shadow evaporation technique. However, previous research [46] has suggested that shadow evaporated devices suffer from shorter spin diffusion lengths in the NM (λ_{NM}) due to magnetic impurity contamination during deposition. Any improvement in the spin signal due to a higher spin polarisation may therefore be counterbalanced by a decrease in λ_{NM}. In this chapter, the competing factors of spin injection and contamination effects on spin diffusion are investigated.

Whilst the original concept behind the LSV envisaged a device largely free of spurious signals, in reality, several thermal background voltages arise as a consequence of the injecting charge current. An offshoot of spintronics called ‘spin caloritronics’ focuses upon the interaction of spin and thermal currents [47, 48]. Even whilst thermal phenomena are not exploited to create spin-dependent effects, large and often complex thermal signals arise which can be entangled with the spin voltages. In Chapter 5, we examine and attempt to explain the temperature and length dependent behaviour of the thermal voltages arising in $Co_{70}Fe_{30}$/Cu LSVs for the first time.

Finally, in Chapter 6, the temperature dependence of the spin diffusion length of $Co_{70}Fe_{30}$ is determined through a spin absorption technique. Gap dependent LSV measurements are frequently employed to extract α_{FM} and λ_{NM}. However, this requires an estimation of λ_{FM} upon which the magnitude and temperature dependence of α_{FM} extracted is directly dependent. Unfortunately, measurements of λ_{FM} are lacking in the literature even though they play a fundamental role in spintronic devices. Our work sought to begin to address this lack of data.

Prior to the experimental chapters discussed above, Chapter 2 details the relevant theory underlying spin currents, spin injection and the spintronic devices used. Additionally, we discuss the theories of spin relaxation in metals and the relevant thermal effects. In Chapter 3, a detailed outline of the device design, fabrication and measurement techniques are presented.

CHAPTER 2

Theory

2.1 Introduction

A pure spin current is the net flow of spin without charge; in metals, it can simply be visualised as an equal number of spin-up and spin-down electrons diffusing in opposite directions. The absence of net charge flow is the key difference between the pure spin current and its counterparts and theoretically negates the possibility of Joule heating; a major contributor to the recent slowing in Moore's Law [49]. This, and the possibility of more sophisticated technologies, are the driving forces behind the study and future implementation of pure spin currents. To achieve this goal there are three central technological challenges to be addressed: the ability to inject information as a pure diffusive spin current into an otherwise unpolarised transport medium; transmission of this information over a sufficient distance without detrimental loss; and, to read the output in a predictable manner. Generally, the task of injection and detection of pure spin currents has fallen to the ferromagnets (FM) due to a naturally occurring spin asymmetry [30, 50–52]. For the transport medium, materials with a weak interaction between electron spin and the lattice are required, specifically non-magnetic (NM) materials with low spin-orbit coupling (SOC) [49, 53, 54]. For metallic spintronics, the light elements Cu, Ag and Al are the most commonly used with pure spin currents persisting over many hundreds of nanometres [14, 55, 56]. The first five sections in this chapter provide a brief overview of the basic concepts relevant to spin injection, transport and detection in metallic structures. Since the pure diffusive spin currents in this work (and most other) are generated by charge currents, several thermoelectric phenomena arise. Thermal effects lead to a number of secondary, but important, voltages which in certain instances interfere with spin transport [38, 39, 50, 57, 58]. The relevant thermal phenomena are discussed in the final section of this chapter.

2.2 Spin and Ferromagnetism

2.2.1 Spin

Spin is an intrinsic internal angular momentum with no true classical analogue. Particles can be classified by their spin (s); those with half–integer spin, such as electrons (s=$\frac{1}{2}$), are fermions which order themselves according to the Fermi–Dirac distribution and are subject to the Pauli exclusion principle. For an electron, the spin angular momentum (**S**) can be expressed as an operator using the Pauli spin matrices:

$$\mathbf{S} = \frac{1}{2}\hbar\boldsymbol{\sigma} \tag{2.1}$$

$$\text{where, } \sigma_x, \sigma_y, \sigma_z = \left(\begin{smallmatrix} 0 & 1 \\ 1 & 0 \end{smallmatrix}\right), \left(\begin{smallmatrix} 0 & -i \\ i & 0 \end{smallmatrix}\right), \left(\begin{smallmatrix} 1 & 0 \\ 0 & -1 \end{smallmatrix}\right)$$

where, $\mathrm{S_x}$, $\mathrm{S_y}$ and $\mathrm{S_z}$ are the components of spin in the x, y and z axes respectively. The observed values of spin are restricted to $+\frac{\hbar}{2}$ or -$\frac{\hbar}{2}$ along any quantisation axis; better known as 'spin-up' or 'spin-down'. For an electron in an atom, there is a magnetic moment associated with the orbital angular momentum (**L**) given by $\boldsymbol{\mu}_\mathbf{o} = -\frac{\mu_\mathrm{B}}{\hbar}\mathbf{L}$, where μ_B= $\frac{e\hbar}{2m_e}$ is the Bohr magneton, $\mathrm{m_e}$ is the electron mass and e is the electron charge. Analogously, there is a magnetic moment arising from the spin angular momentum given by $\boldsymbol{\mu}_\mathbf{s}= -\frac{g\mu_B}{\hbar}\mathbf{S}$, where g is the spin g-factor which close to 2. Due to the much greater mass of the nucleus, the magnetic moment produced by nuclear spin is negligible compared to that of the electron. It is, therefore, the electrons that are responsible for the magnetic properties of many solids [59, 60]. In some cases, such as bulk 3d transition metals, the orbital contributions are quenched by the crystal field and the unpaired electron spins are the dominant contributors to magnetism [61].

2.2.2 Ferromagnetism

FMs perform a crucial role in spintronics as the most commonly used sources and detectors of spin polarised carriers. Within an FM, there exists long-range magnetic order that tends to align the unpaired electron spins parallel to one another. The origin of this magnetic order depends on the electronic structure of the material. Relevant to this work are the itinerant 3d FMs, whose magnetism arises as a result of the competition between exchange and kinetic energy within the 3d bands; this concept is explained below [60].

Exchange

The total wavefunction of an electron can be expressed as the product of the spatial (ψ) and spin (χ) parts as $\Psi = \psi\chi$. As electrons are fermions, the total wavefunction must be anti-symmetric. Consider two electrons (1,2) in different orbitals (p,q) of the same atom with spatial wavefunctions $\psi_p(1)$ and $\psi_q(2)$. From the constraints outlined above, and that electrons are indistinguishable, the allowed two-particle total wavefunctions are:

$$\Psi_\mathrm{S} = \frac{1}{\sqrt{2}}[\psi_p(1)\psi_q(2) + \psi_p(2)\psi_q(1)]\chi_S \tag{2.2}$$

$$\Psi_\mathrm{T} = \frac{1}{\sqrt{2}}[\psi_p(1)\psi_q(2) - \psi_p(2)\psi_q(1)]\chi_T \tag{2.3}$$

Ψ_S is the spin singlet state, consisting of a symmetric combination of the spatial wave functions and, to maintain an overall anti-symmetric Ψ_S, an anti-symmetric spin state χ_S. In this instance, the electrons may occupy the same orbital but must have their spins aligned anti-parallel (S = 0). Conversely, Ψ_T is the spin triplet state which contains an anti-symmetric combination of spatial states and a symmetric spin state χ_T. Here, there are three possible spin orientations (S = 1, S = −1 or S = 0) and the electrons cannot occupy the same orbital. Therefore, the spatial separation of the electrons and thus the Coulomb repulsion experienced depends on the alignment of their spins. As a result, there is a difference in electrostatic energy for the triplet ($\mathrm{E_T}$) and singlet ($\mathrm{E_S}$) states from which the exchange constant (J) can be defined as $\mathrm{J} = \frac{\mathrm{E_S}-\mathrm{E_T}}{2}$ [59]. This is the exchange interaction. It is a consequence of the symmetry constraints imposed on the electron wavefunctions by the Pauli principle and the subsequent modification of the electrostatic energy depending on spin. When J is negative ($\mathrm{E_S} < \mathrm{E_T}$), the singlet state is of lower energy leading to an anti-parallel alignment of spins. If J is positive, the triplet state is energetically favourable leading to a parallel alignment of spins.

Stoner Ferromagnetism

In the 3d bands of the itinerant metals, it can be energetically favourable for the bands to spontaneously spin split if the reduction in Coulomb energy (gain in exchange energy $\mathrm{E_{ex}}$) is greater than the price in kinetic energy required to promote electrons to higher energies. As shown in Figure 2.1(a), this exchange splitting leads to an imbalance in the spin-up and spin-down electron populations and consequently net magnetism. The criterion for this phenomenon to occur was neatly summed up by Stoner: spontaneous ferromagnetism will arise if $N(\epsilon_F)J > 1$, where $N(\epsilon_F)$ is the density of states at the Fermi energy and J is the exchange constant [61]. The Stoner criterion demonstrates why exchange splitting of this type is not observed in the s bands (which are broad with a low $N(\epsilon_F)$), nor in the d bands of many materials as shown in Figure 2.1(b).

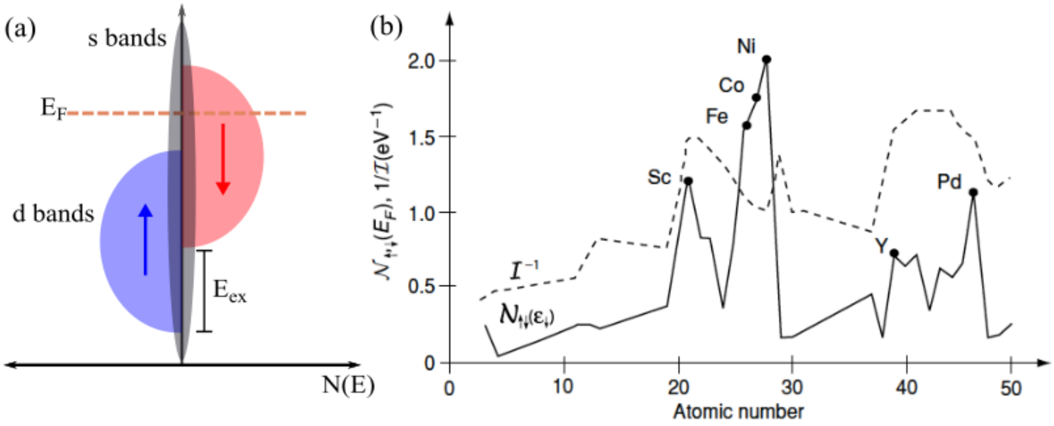

Figure 2.1: (a) Simplified band diagram illustrating the exchange splitting of the d bands in an itinerant FM. A proportion of one spin species (in this case spin-down) are promoted to higher energies, resulting in a net spin-up polarisation. (b) The condition set by the Stoner criterion for spontaneous magnetism $N(\epsilon_F) > I^{-1}$ (I is equivalent to J) across the 3d transition metal series. There are only three elements (Fe, Co and Ni) in this series where $N(\epsilon_F)$ (solid line) exceeds I^{-1} (dotted line) and ferromagnetism occurs. Alloying these materials together retains and can improve the ferromagnetism, taken from [1].

Transport and Polarisation

The exchange splitting of the d bands has important consequences in charge transport. The most obvious effect is that as $N(\epsilon_F)_\uparrow \neq N(\epsilon_F)_\downarrow$ in the d bands, the d electrons have different conductivities depending on their spin. The high mobility s electrons also contribute to the charge current in itinerant FMs. Although the s states experience no exchange splitting, they acquire a small degree of spin polarisation through s–d hybridisation [62]. Additionally, s–d scattering events provide additional spin polarisation to the net conductivity. Scattering by phonons, electrons and defects can take an electron from an s state to a d state whilst conserving spin. The density of available d states to scatter into at some temperature T is given by $\mathrm{N}(\epsilon_{\mathrm{F}} \pm \mathrm{k_B T})$, where $\mathrm{k_B}$ is the Boltzmann constant. Due to the exchange splitting, $\mathrm{N}(\epsilon_{\mathrm{F}} \pm \mathrm{k_B T})$ is higher for one spin species so, according to Fermi's golden rule, the s–d scattering rate will be greater for s electrons with spins parallel to the high $\mathrm{N}(\epsilon)$ d band [59, 61]. Consequently, the conductivity of both s and d electrons are spin-dependent and the charge current in an FM is naturally spin polarised; providing a convenient source of spin polarised electrons for spintronics.

In a spintronic device, it is generally favourable to maximise spin dependent effects to improve the signal to noise ratio. In part, this can be achieved by choosing an FM with a high degree of spin asymmetry. The degree of spin polarisation (α) is a useful indicator; it takes a value between 0 and 1, where 1 indicates 100% spin asymmetry. As identified by I.I. Mazin [63], α can be defined in several different ways depending on the measurement setup. Given that the spin asymmetry in an itinerant FM arises from the exchange splitting of the d bands, quite simply the spin polarisation can be defined as the difference in the density of states for each spin type, $\alpha = \frac{\mathrm{N}(\epsilon_{\mathrm{F}})_\uparrow - \mathrm{N}(\epsilon_{\mathrm{F}})_\downarrow}{\mathrm{N}(\epsilon_{\mathrm{F}})_\uparrow + \mathrm{N}(\epsilon_{\mathrm{F}})_\downarrow}$. In practice though, this definition is of little use. As outlined in the previous paragraph, the difference in the density of states is not the only factor determining the spin polarisation of the charge current (α_{FM}). Given that α_{FM} arises from a multitude of interconnected factors, a detailed formulation is challenging; but, through the use of the Mott two-channel model, a rough definition can be obtained [64]. Mott postulated that if the occurrence of a spin-flip was far rarer than a normal scattering event, the transport phenomena for each spin type could be lumped into two families with different conductivities ($\sigma_{\uparrow,\downarrow}$). Thereby, the spin polarisation of the charge current can be defined as: $\alpha_{\mathrm{FM}} = \frac{\sigma_\uparrow - \sigma_\downarrow}{\sigma_\uparrow + \sigma_\downarrow}$, where $\sigma_\uparrow$ and $\sigma_\downarrow$ are the conductivities of the spin-up and spin-down electron populations respectively.

2.3 Length Scales of Interest

Having discussed the source of our spin polarised electrons, the next step is to inject the spin polarised current into the NM medium and derive the equations that describe the subsequent spin diffusion. Prior to this, we define the characteristic spin and charge transport length scales which simplify the descriptions and allow for different transport regimes to be distinguished. Firstly, neglecting spin and considering the electron population as a whole we can define three relevant length scales:

- Elastic Mean Free Path

  The elastic mean free path ($\mathrm{l_e}$) is defined as the average distance an electron travels between elastic scattering events. These scattering events stem from the imperfections present within the crystal (or surfaces) which distort the otherwise periodic potential of the lattice and can produce large changes in momentum without a change in energy. Therefore, the structure and the presence of impurities are the largest contributors to this length scale.

- Inelastic Mean Free Path

  Alternatively, an electron may scatter and change its energy in an inelastic event. One example is electron-phonon scattering, where an electron may lose (or gain) energy if a phonon is emitted (or absorbed) during the scattering event. Additionally, electron-electron scattering events may also produce inelastic scattering. The characteristic length scale for these events is termed the inelastic mean free path ($\mathrm{l_{ie}}$), which is defined as the average distance an electron travels between inelastic scattering events.

- Electronic Mean Free Path

  The electronic mean free path (λ_e) is defined as the average distance an electron travels between scattering events which impart large changes in momentum. This is the length scale relevant to measured resistivity (ρ) and is a combination of $\mathrm{l_e}$ and $\mathrm{l_{ie}}$. At very low temperatures, where impurity and residual defect scattering dominates, it is comparable to $\mathrm{l_e}$. At high temperatures, where electron-phonon scattering dominates, it is comparable to $\mathrm{l_{ie}}$. λ_e can be calculated from the momentum relaxation time (τ_e), which is the average time between momentum scattering events. Assuming nearly free conduction electrons, the Drude model can be used to calculate τ_e from the measured resistivity as $\frac{1}{\rho} = \frac{\mathrm{ne}^2\tau_\mathrm{e}}{\mathrm{m}}$, where m is the free electron mass and n is the conduction electron density. The electronic mean free path can then be calculated from $\lambda_\mathrm{e} = \tau_\mathrm{e}\mathrm{v_F}$, where $\mathrm{v_F}$ is the Fermi velocity.

Comparing λ_e with a suitable transport length scale, for example the wire length (L), two transport regimes can be defined: the diffusive regime ($\lambda_\mathrm{e} < \mathrm{L}$), where electrons experience many scattering events as they traverse a sample; and, a ballistic regime ($\lambda_\mathrm{e} > \mathrm{L}$), where electrons move ballistically through the sample only scattering from the boundaries. In this work, we focus upon diffusive transport only. For spin transport another two length scales can be defined:

- Spin-Flip Length

  The spin-flip length ($\mathrm{l_{sf}}$) is defined as the mean distance between sequential spin-flipping events.

- Spin Diffusion Length

  The spin diffusion length (λ_s) is the mean distance an electron will diffuse between spin-flipping events and is the geometric mean of $\mathrm{l_{sf}}$ and λ_e, given by $\lambda_\mathrm{s} = \sqrt{\frac{1}{3}\lambda_\mathrm{e}\mathrm{l_{sf}}}$. This is perhaps the most important length scale for spintronic devices, as it dictates the length scale over which non-equilibrium spin polarisations will persist.

Considering the above we can effectively design and understand device transport properties. The importance of these length scales will become clear as they feature frequently in the equations in the following sections.

2.4 Spin Currents and Spin Injection

2.4.1 Spin Currents

Diffusive transport of the electron population can be understood by considering the electrochemical potential (μ), which is the sum of the Fermi level (ϵ_{F}) and the electrical potential (ϕ) as $\mu = \epsilon_{\mathrm{F}} - \mathrm{e}\phi$. A local gradient in μ acts as a driving force for electron transport and can arise due to a spatial variation in ϵ_F, which is related to local electron density (n), or an electric field. Following the assumptions of the Mott two-channel model, the behaviour of the spin-up and spin-down electrons can be described separately using a spin-dependent electrochemical potential $\mu_\sigma = \epsilon_{\mathrm{F}}^{\sigma} - \mathrm{e}\phi$, where σ denotes the electron spin. The current density ($\mathbf{j}$) in a conductor is the combination of the electric field ($\mathbf{E}$) induced drift current ($\sigma\mathbf{E}$) and diffusion current ($\mathrm{eD}\nabla\mathrm{n}$).

$$\mathbf{j} = \sigma\mathbf{E} + \mathrm{eD}\nabla\mathrm{n} \tag{2.4}$$

Considering the form of the Fermi-Dirac distribution for a free electron gas where $\mathrm{T} \ll \mathrm{T_F}$, $\nabla\epsilon_{\mathrm{F}}^{\sigma}$ may be expressed as $\mathrm{N}(\epsilon_{\mathrm{F}})_\sigma\nabla\epsilon_{\mathrm{F}}^{\sigma} = \nabla\mathrm{n}_\sigma$ [59]. Combining this, equation 2.4, and the Einstein equation for conductivity $\sigma_\sigma = \mathrm{e}^2\mathrm{N}(\epsilon_{\mathrm{F}})_\sigma\mathrm{D}_\sigma$, the current density in each spin channel can be written as:

$$\mathbf{j}_\uparrow = -\sigma_\uparrow\nabla\mu_\uparrow \tag{2.5}$$

$$\mathbf{j}_\downarrow = -\sigma_\downarrow\nabla\mu_\downarrow \tag{2.6}$$

Defining the spin and charge currents as $\mathbf{j_s} = \mathbf{j}_\uparrow - \mathbf{j}_\downarrow$ and $\mathbf{j_c} = \mathbf{j}_\uparrow + \mathbf{j}_\downarrow$ respectively, we obtain:

$$\mathbf{j_s} = \frac{1}{\mathrm{e}}\nabla(\sigma_\uparrow\mu_\uparrow - \sigma_\downarrow\mu_\downarrow) \tag{2.7}$$

$$\mathbf{j_c} = \frac{1}{\mathrm{e}}\nabla(\sigma_\uparrow\mu_\uparrow + \sigma_\downarrow\mu_\downarrow) \tag{2.8}$$

Through conservation laws the steady state continuity equations for the charge and spin currents are given by:

$$\nabla \cdot \mathbf{j_c} = 0 \tag{2.9}$$

$$\nabla \cdot \mathbf{j_s} = -\mathrm{e}\frac{\delta \mathrm{n}_\uparrow}{\tau_{\uparrow\downarrow}} + \mathrm{e}\frac{\delta \mathrm{n}_\downarrow}{\tau_{\downarrow\uparrow}} \tag{2.10}$$

where, $\delta\mathrm{n}_\sigma = \mathrm{n}_\sigma - \mathrm{n}_\sigma^0$ is the deviation from equilibrium carrier density (n_σ^0) for each spin and $\tau_{\uparrow\downarrow}$ ($\tau_{\downarrow\uparrow}$) is the characteristic spin scattering time between ↑ to ↓ (↓ to ↑). At equilibrium, there should be no net spin relaxation which requires that $\frac{\mathrm{N}(\epsilon_\mathrm{F})_\uparrow}{\tau_{\uparrow\downarrow}} = \frac{\mathrm{N}(\epsilon_\mathrm{F})_\downarrow}{\tau_{\downarrow\uparrow}}$. From the above, we obtain the key equations for charge (2.11) and spin current (2.12) evolution in the steady state:

$$\nabla^2(\sigma_\uparrow\mu_\uparrow + \sigma_\downarrow\mu_\downarrow) = 0 \tag{2.11}$$

$$\nabla^2(\mu_\uparrow - \mu_\downarrow) = \frac{1}{\lambda_\mathrm{s}^2}(\mu_\uparrow - \mu_\downarrow) \tag{2.12}$$

The difference in the spin-dependent electrochemical potentials ($\mu_\uparrow - \mu_\downarrow$) represents a non-equillibrium spin population and is called the spin accumulation. Equation 2.12, the spin diffusion equation, demonstrates that the key ingredients to generate a diffusive spin current are a net spin accumulation and a spatial gradient in that spin accumulation. Furthermore, it demonstrates that the non-equillibrium spin population will persist over a length scale determined by the spin diffusion length in the material (λ_s). The above equations can be solved for a specific device geometry to obtain the spatial dependence of the spin-dependent electrochemical potentials.

2.4.2 Spin Injection

One method to generate a spin accumulation is to drive a charge current across a metallic FM/NM interface, in what is commonly known as electrical spin injection. As stated previously, in an FM the conductivity of spin-up and spin-down electrons are not equal ($\sigma_\uparrow \neq \sigma_\downarrow$). Therefore, when a current flows from the FM into an NM, where $\sigma_\uparrow = \sigma_\downarrow$, there must be a redistribution of the current carrying electrons across the two spin channels. For example, if $\sigma_\uparrow > \sigma_\downarrow$ in the FM, there will be an excess of spin-up electrons injected into the NM and, to maintain charge neutrality, there must be a corresponding loss of spin-down carriers. The net result is an increase in the population of spin-up and depletion of spin-down electrons at the interface, which yields the local spin accumulation required to drive a diffusive spin current.

This problem was initially outlined by van Son et al. [65], who considered a simplified 1D interface with the FM at x<0, NM at x>0 and a transparent interface (no spin-flipping) at x=0. Equation 2.12 was solved to obtain the spatial variation of the spin-dependent electrochemical potentials with the following boundary conditions:

- $\mu_\uparrow$ and $\mu_\downarrow$ are continuous across the interface
- $\mathbf{j}_\uparrow$ and $\mathbf{j}_\downarrow$ are conserved at the interface
- $\mathbf{j_c}$ is spatially homogenous
- as $\mathrm{x} \to \infty$ there is no spin accumulation and $\mu_\uparrow = \mu_\downarrow$

Firstly, the current conversion process between the NM and FM led to a spin accumulation at the interface. This is shown schematically in Figure 2.2, where $\mu_\uparrow > \mu_\downarrow$ in the regions with an excess of spin-up electrons and net spin accumulation. The local spin accumulation drove a diffusive spin current into the NM, which decayed over the spin diffusion length of the NM (λ_{NM}). Moreover, there was a backflow of the diffusive spin current into the FM over the spin diffusion length of the FM (λ_{FM}). As a result, the spin polarisation of the injected current at the interface (α_{i}) was reduced from the bulk spin current polarisation of the FM (α_{FM}), and was found to be:

$$\alpha_{\mathrm{i}} = \alpha_{\mathrm{FM}} \frac{1}{1 + (1 - \alpha_{\mathrm{FM}}^2)\frac{\sigma_{\mathrm{FM}}\lambda_{\mathrm{NM}}}{\sigma_{\mathrm{NM}}\lambda_{\mathrm{FM}}}} \tag{2.13}$$

where, σ_{FM} and σ_{NM} are the total conductivities of the FM and NM respectively. Secondly, even though the spin-dependent electrochemical potentials were continuous across the interface, the average electrochemical potential ($\mu = \frac{\mu_\uparrow + \mu_\downarrow}{2}$) was not. The magnitude of the discontinuity at the interface is $\Delta\mu$, and for metallic transparent interfaces is related to the spin accumulation through $\Delta\mu = \frac{\alpha_{\mathrm{FM}}(\mu_\uparrow + \mu_\downarrow)}{2}$ [66]. This led to a potential difference ($\Delta \mathrm{V} = \frac{\Delta\mu}{\mathrm{e}}$) between the FM and NM, which can be expressed as a spin-dependent interface resistance ($\mathrm{R_s}$):

$$\mathrm{R_s} = \frac{\Delta \mathrm{V}}{\mathrm{I_c}} = \alpha_{\mathrm{FM}}^2 \frac{\lambda_{\mathrm{NM}}\sigma_{\mathrm{NM}}^{-1}}{1 + (1 - \alpha_{\mathrm{FM}}^2)\frac{\sigma_{\mathrm{FM}}\lambda_{\mathrm{NM}}}{\sigma_{\mathrm{NM}}\lambda_{\mathrm{FM}}}} \tag{2.14}$$

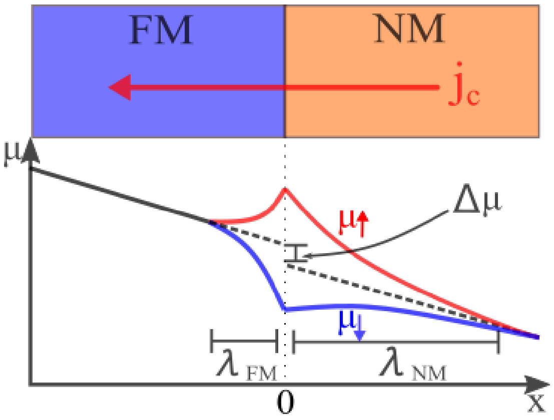

Figure 2.2: Schematic of an FM/NM interface with j_c through it. The plot depicts the spatial variation of $\mu_\uparrow$ (red), $\mu_\downarrow$ (blue) and the average electrochemical potential μ (black dashes). In the regions close to the interface, where $\mu_\uparrow > \mu_\downarrow$, there is a net spin-up accumulation. This spin accumulation is largest at the interface and decays either side over λ_s in each material to the equilibrium value; zero in the NM and to a value in the FM determined by α_{FM}. There is a discontinuity in the average electrochemical potential at the interface ($\Delta\mu$), which gives rise to a potential difference between the NM and FM.

Of note, the term $(\frac{\sigma_{\mathrm{FM}}\lambda_{\mathrm{NM}}}{\sigma_{\mathrm{NM}}\lambda_{\mathrm{FM}}})^{-1}$ is a limiting factor for the magnitude of α_{i} and $\mathrm{R_s}$. This is a consequence of the difference in the spin resistances of the NM and FM. The spin resistance is defined as $\mathrm{R_S} = \frac{\lambda_{\mathrm{S}}}{\sigma \mathrm{A}}$, where A is the element area perpendicular to the direction of spin current flow. Materials with low spin resistances act as spin sinks, where the spin current is preferentially relaxed [67]. In this simplified model, both the FM and NM are of unit area so the limiting factor is equivalent to the ratio of the spin resistances $\frac{\mathrm{R_{FM}}}{\mathrm{R_{NM}}}$. When $\mathrm{R_{FM}}$ is small compared to $\mathrm{R_{NM}}$, there is a large backflow of spins into the FM, which reduces both α_{i} and $\mathrm{R_s}$. In all metallic devices, the much shorter spin diffusion length in the FM ($\lambda_{\mathrm{FM}} \ll \lambda_{\mathrm{NM}}$) is the primary contributor to the spin backflow [10, 11, 42, 68].

2.5 Spintronic Devices

2.5.1 Lateral Spin Valves

In order to probe spin transport in the NM without the accompanying charge current, a lateral spin valve (LSV) may be used. Figure 2.3 depicts a typical two terminal LSV composed of an FM injector ($\mathrm{FM_1}$), NM transport channel and detecting FM ($\mathrm{FM_2}$). Passing a charge current through the $\mathrm{FM_1}$/NM interface and draining the current out the left side of the device generates a spin accumulation at this interface. The local spin accumulation drives a diffusive spin current in both directions of the NM channel; the spin current diffusing to the right of the injecting interface is free from the charge current and is, therefore, a pure diffusive spin current. The spin current will decay over λ_{NM} due to spin scattering as it diffuses along the NM channel. Any remaining spin accumulation at the detecting $\mathrm{FM_2}$/NM interface produces a discontinuity in the average electrochemical potential, as outlined in the previous section, that is proportional to the spin accumulation at that point [26]. This discontinuity produces a voltage between the NM channel and $\mathrm{FM_2}$ detector, as indicated in Figure 2.3. The sign of this voltage depends on the relative alignment of the $\mathrm{FM_1}$ and $\mathrm{FM_2}$ magnetisations and the direction of the current.

For a positive current ($\mathrm{FM_1}$ to NM) one spin type, in this case spin-up, will be accumulated in the NM channel. As illustrated in Figure 2.4, when the FM magnetisations are aligned parallel (P) the chemical potential in the detector will align with $\mu_{\uparrow}$ in the NM, leading to a positive $\Delta\mu$. Whereas, in the anti-parallel (AP) alignment, the spin-

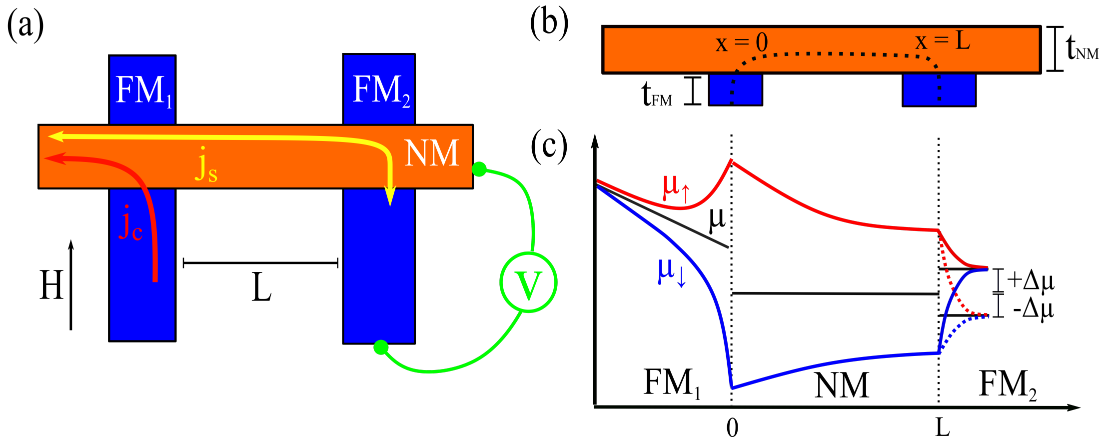

Figure 2.3: (a) Schematic of a typical LSV with an NM transport channel bridging the injecting electrode FM_1 and detecting electrode FM_2. A spin current is generated by passing a charge current through the FM_1/NM interface and detected as a non-local voltage across the FM_2/NM interface. (b) Side view of LSV. (c) 1D representation of the evolution of spin-dependent electrochemical potentials across the device. A net spin-up accumulation is injected into the NM at the FM_1/NM interface (point a), decays exponentially due to spin scattering in the NM channel and the remaining spin accumulation at the FM_2/NM interface (point b) produces a discontinuity in the average electrochemical potential ($\Delta\mu$) that is equal and opposite in sign in the P (solid lines) and AP (dashed lines) states .

down chemical potentials align and $\Delta\mu$ is negative; $\Delta\mu$ is equal and opposite in sign in the P and AP magnetisation states. If the direction of the current is reversed (NM to FM_1), spin-down electrons accumulate in the NM channel and $\Delta\mu$ is negative in the P state and positive in the AP state. The spin injection mechanism upon reversing the current is unchanged, therefore $\Delta\mu$ is equal and opposite in sign for opposite polarity currents [50]. Generally, the voltage induced by the spin accumulation is normalised by the injection current to obtain the non-local spin resistance; which is positive in the P state ($\mathrm{R_P}$) and negative in the AP state ($\mathrm{R_{AP}}$). The device magnetoresistance, or the 'spin signal', is the difference between the non-local spin resistance in the P and AP states and given by $\Delta\mathrm{R_S} = \mathrm{R_P} - \mathrm{R_{AP}} = \frac{2\Delta\mu}{\mathrm{eI_c}}$. Analogous to the approach taken by van Son et al. [65], the 1D spin diffusion model for transparent interfaces can be used to describe the spin diffusion properties of an LSV. With appropriate boundary

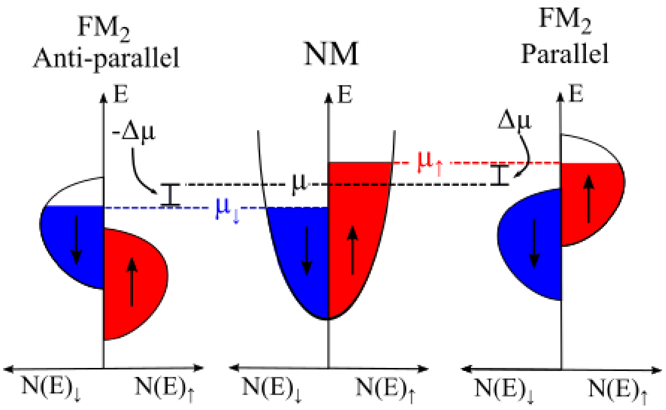

Figure 2.4: Simplified band diagram of the NM (with a net spin-up accumulation) at the detecting interface and the detecting electrode (FM$_2$) in the P and AP states; adapted from [26].

conditions, an expression for ΔR_S can be obtained as:

$$\Delta R_s = \frac{2\Delta V}{I_c} = \frac{4\alpha_{FM}^2 R_{FM}^2}{(1-\alpha_{FM}^2)^2 R_{NM}} \frac{e^{-L/\lambda_{NM}}}{(1+\frac{2R_{FM}}{(1-\alpha_{FM}^2)R_{NM}})^2 - e^{-2L/\lambda_{NM}}} \tag{2.15}$$

where, α_{FM} is the bulk FM current polarisation we defined earlier, L is the separation between the FM electrodes, and R_{FM} and R_{NM} are the spin resistances of the FM and NM respectively. The spin resistances here are defined as: $R_{NM} = \frac{\rho_{NM}\lambda_{NM}}{A_{NM}}$ and $R_{FM} = \frac{\rho_{FM}\lambda_{FM}}{A_{FM}}$, where $A_{NM} = w_{NM}t_{NM}$ and $A_{FM} = w_{NM}w_{FM}$ are the element areas perpendicular to the direction of spin current flow. Varying L and measuring ΔR_S in otherwise geometrically identical LSVs allows for the key spintronic material parameters α_{FM} and λ_{NM} to be extracted from equation 2.15.

2.5.2 Spin Absorption Devices

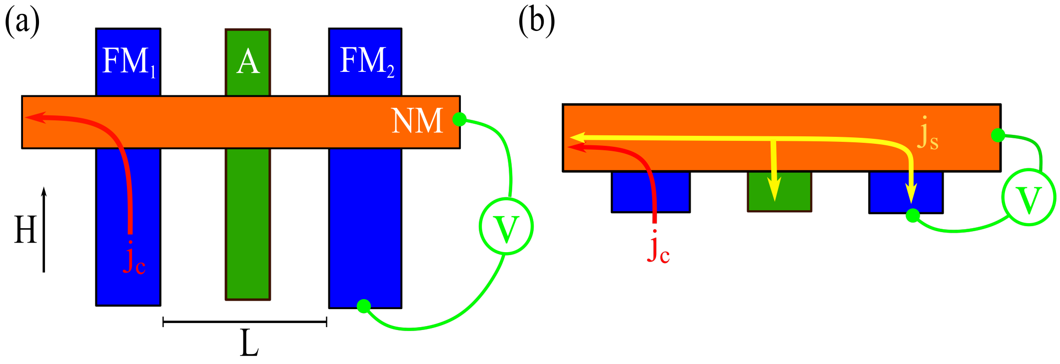

Figure 2.5: (a) Schematic of a typical spin absorption device from above with current and voltage probes in the non-local configuration; FM_1 is used as the injector, FM_2 is the detector and the central wire (A) is composed of the material in which the spin diffusion length is to be determined. (b) Side view of the spin absorption device. The charge current (red) driven through the FM_1/NM interface drives a diffusive spin current (yellow) in the NM channel. As the central wire has a low spin resistance, some of the spin current is absorbed by A and reduces the spin accumulation that reaches the detecting FM_2/NM interface.

LSV measurements are an effective tool to study spin transport in materials with relatively long spin diffusion lengths about which L can be varied. For those shorter than a few hundred nanometres, such as FM materials or heavy metals like Pt, LSV measurements are unviable due to the limits on minimum feature size and current spreading effects. An alternative is the spin absorption method, which has been demonstrated to effectively determine short λ_s for both heavy metals and FMs [10, 11, 69–71]. In a spin absorption device (SAD), a central floating wire (A) of which λ_s is to be determined is introduced between the electrodes of an LSV; a schematic is depicted in Figure 2.5. As in a regular LSV measurement, a charge current through the FM_1/NM interface generates a local spin accumulation and drives a pure diffusive spin current in the NM channel. Depending on the relative spin resistances of the NM and A, some of the spin current will be absorbed by A. Spin absorption by the central wire reduces the spin accumulation that reaches the FM_2/NM interface and thus the measured ΔR_S. Provided that the assumption of a point contact is valid (i.e. the width of the absorber is less than the spin diffusion length in the channel, $\mathrm{w_A} < \lambda_{\mathrm{NM}}$) [70] we can compare $\Delta\mathrm{R_S}$ for the SAD device ($\Delta\mathrm{R_S^{abs}}$) with that of a reference LSV ($\Delta\mathrm{R_S^{ref}}$), which is a geometrically identical LSV without an absorbing wire. Using the 1D model from the previous sections the ratio of the spin signals $\eta = \frac{\Delta\mathrm{R_S^{abs}}}{\Delta\mathrm{R_S^{ref}}}$ can be written as [10]:

$$\eta = \frac{2\frac{\mathrm{R_A}}{\mathrm{R_{NM}}}(\sinh\left(\frac{\mathrm{L}}{\lambda_{\mathrm{NM}}}\right) + 2\frac{\mathrm{R_{FM}}}{\mathrm{R_{NM}}}\mathrm{e}^{\frac{\mathrm{L}}{\lambda_{\mathrm{NM}}}} + 2\frac{\mathrm{R_{FM}^2}}{\mathrm{R_{NM}}}\mathrm{e}^{\frac{\mathrm{L}}{\lambda_{\mathrm{NM}}}})}{(\cosh\left(\frac{\mathrm{L}}{\lambda_{\mathrm{NM}}}\right) - 1) + 2\frac{\mathrm{R_A}}{\mathrm{R_{NM}}}\sinh\left(\frac{\mathrm{L}}{\lambda_{\mathrm{NM}}}\right) + 2\frac{\mathrm{R_{FM}}}{\mathrm{R_{NM}}}(\mathrm{e}^{\frac{\mathrm{L}}{\lambda_{\mathrm{NM}}}}(1 + \frac{\mathrm{R_{FM}}}{\mathrm{R_{NM}}})(1 + 2\frac{\mathrm{R_A}}{\mathrm{R_{NM}}}) - 1)} \tag{2.16}$$

When $\mathrm{FM_1}$, $\mathrm{FM_2}$ and A are composed of the same material $\mathrm{R_A} = \mathrm{R_{FM}}$. In this instance, λ_{FM} can be extracted from equation 2.16 by substituting in known values and an estimate of α_{FM} from complimentary LSV measurements. This value can be refined by refitting equations 2.16 and 2.15 until the parameters converge.

2.6 Spin Scattering

The average distance over which the non-equilibrium spin population persists is determined by spin relaxation and dephasing processes within the material. The precession, diffusion and decay of a spin ensemble in an applied field is determined by two relaxation times, $\mathrm{T_1}$ and $\mathrm{T_2}$, which feature in the Bloch-Torrey equations [54, 72, 73]. The spin relaxation time (or longitudinal relaxation time) $\mathrm{T_1}$ is the characteristic time for spins aligned collinear to the field to equilibrate through the exchange of energy from the spin system to the lattice. $\mathrm{T_2}$, the spin dephasing time (or transverse/ coherence time), is the time scale over which transverse spins that initially precess in phase about the longitudinal field lose coherence through fluctuations in the precession frequencies. For a NM isotropic cubic material (in an applied field up to several tesla) these two relaxation times are equal, allowing for a single spin relaxation time τ_{sf} to be defined as $\mathrm{T_1}=\mathrm{T_2}=\tau_{\mathrm{sf}}$. This situation should apply to Cu which is employed as the NM transport medium throughout this thesis. In a FM metal the situation is slightly more complex due to the internal magnetic field. Recent reports have indicated that in some cases $\mathrm{T_1} >> \mathrm{T_2}$, as the relaxation mechanisms for longitudinal and transverse spins are different [74, 75]. In this thesis we probe only collinear spin relaxation characterised by

T_1, which we denote as τ_{sf} henceforth.

In diffusive spin transport, τ_{sf} is related to the spin diffusion length $\lambda_{\mathrm{s}} = \sqrt{\mathrm{D}\tau_{\mathrm{sf}}}$, where D is the spin averaged diffusion coefficient given by $\mathrm{D} = \frac{\mathrm{D}_{\uparrow}\mathrm{D}_{\downarrow}(\mathrm{N}_{\uparrow}+\mathrm{N}_{\downarrow})}{\mathrm{D}_{\uparrow}\mathrm{N}_{\uparrow}+\mathrm{D}_{\downarrow}\mathrm{N}_{\downarrow}}$ with $\mathrm{D}_{\uparrow}$ and $\mathrm{D}_{\downarrow}$ as the spin-dependent diffusion coefficients. For spintronics to be viable, we must have $\tau_{\mathrm{sf}} > \tau_{\mathrm{e}}$ in the transport medium due to weak coupling between the electron spin and the environment. This coupling is a relativistic effect called SOC; in the rest frame of a moving electron it perceives an electrical potential (such as a lattice ion) as a magnetic field that can interact with its spin. In addition to the intrinsic crystal potential there are surfaces, interfaces, impurities, grain boundaries and vacancies all of which may contribute to the SOC of a material creating an incredibly complex situation which is highly sensitive to dimensionality, doping and alloying. In metals, there are two prevailing theories of spin relaxation: Elliott-Yafet (EY) and Dyakonov-Perel mechanisms. The former is the dominant process of spin relaxation in the low resistance metals with inversion symmetry studied in this work.

2.6.1 Elliott-Yafet

The EY mechanism contains two contributions which are usually combined into a single EY theory. The Elliott component arises from the inclusion of the SOC interaction from the periodic lattice potential in the Hamiltonian of the conduction electrons as [76]:

$$\mathrm{V}_{\mathrm{SOC}} = \frac{\hbar}{4\mathrm{m}^2\mathrm{c}^2}\nabla\mathrm{V}_{\mathrm{sc}} \times \hat{\mathrm{p}} \cdot \hat{\sigma} \tag{2.17}$$

where, V_{sc} is the spin independent periodic lattice potential, $\hat{\mathrm{p}} = -\mathrm{i}\hbar\nabla$ is the linear momentum operator, m is the free electron mass, c is the speed of light and $\hat{\sigma}$ are the Pauli spin matrices. As a consequence of this interaction, the electron Bloch states are no longer pure spin eigenstates and are instead a linear combination of the Pauli spin-up $|\uparrow\rangle$ and spin-down $|\downarrow\rangle$ states. For the specific case of metals with inversion symmetry the new degenerate Bloch states become:

$$\psi^{\uparrow}_{\mathbf{k},n}(\mathbf{r}) = [a_{\mathbf{k},n}(\mathbf{r})\,|\uparrow\rangle + b_{\mathbf{k},n}(\mathbf{r})\,|\downarrow\rangle]e^{i\mathbf{k}\cdot\mathbf{r}} \tag{2.18}$$

$$\psi^{\downarrow}_{\mathbf{k},n}(\mathbf{r}) = [a^{*}_{-\mathbf{k},n}(\mathbf{r})\,|\downarrow\rangle - b^{*}_{-\mathbf{k},n}(\mathbf{r})\,|\uparrow\rangle]e^{i\mathbf{k}\cdot\mathbf{r}} \tag{2.19}$$

where, n is the band index, $\mathbf{k}$ is the wave vector, $\mathbf{r}$ is the radius vector and a, b are the coupling coefficients. Generally, SOC is a weak effect compared to the other terms in the Hamiltonian so it can be treated as a perturbation. In this instance, a is close to unity and $b << 1$, so $\psi^{\uparrow}_{\mathbf{k},n}$ is a predominantly spin-up state and $\psi^{\downarrow}_{\mathbf{k},n}$ is spin-down. For states with a non-vanishing b, ordinarily spin conserving momentum scattering events (such as those with phonons) can induce a transition between $\psi^{\downarrow}_{\mathbf{k},n}$ and $\psi^{\uparrow}_{\mathbf{k},n}$ and result in a spin-flip.

Later, Yafet suggested that an additional contribution arose from the modulation of the spin-orbit interaction between electrons and the lattice by phonons [77]. He demonstrated that the temperature dependence of the spin relaxation rate should mirror that of the momentum relaxation rate as $\frac{1}{\tau_{\mathrm{sf}}} = \frac{\alpha}{\tau_{\mathrm{e}}}$, where α is a temperature independent constant. Here, α is the spin-flip probability which dictates the probability per momentum scattering event that it will result in a spin-flip. The spin-flip probability depends on the particular scattering mechanism due to the combined effects of the spin-orbit interaction from the scattering potential and that of the host [78–81]. For example, spin-orbit effects in the vicinity of an impurity are strongly affected by the difference in valence (ΔZ) between the impurity and the host. For large ΔZ, strong spin-orbit effects will lead to a higher α than for small ΔZ [82, 83]. Fortunately for spintronics, most scattering mechanisms have low spin-flip probabilities ($\alpha << 1$) and the spin relaxation time is much longer than the momentum relaxation time. In the presence of multiple scattering sources, the general approach is to assume that they are independent and apply Matthiessen's rule to yield the generalised EY relationship [84]:

$$\frac{1}{\tau_{\mathrm{sf}}} = \sum_{\mathrm{i}} \frac{1}{\tau_{\mathrm{sf,i}}} = \sum_{\mathrm{i}} \frac{\alpha_{\mathrm{i}}}{\tau_{\mathrm{e,i}}} \tag{2.20}$$

where, $\tau_{\mathrm{e,i}}$, $\tau_{\mathrm{sf,i}}$ and α_i are the momentum relaxation time, spin relaxation time and probability of a spin-flip for the i-th scattering mechanism[85]. From measurements of τ_{sf} and τ_{e}, equation 2.20 can be applied to separate τ_{sf} into its constituent spin scattering contributions and extract α_i for each. This is incredibly useful as it allows for comparison between the efficiency of spin relaxation for different scattering mechanisms.

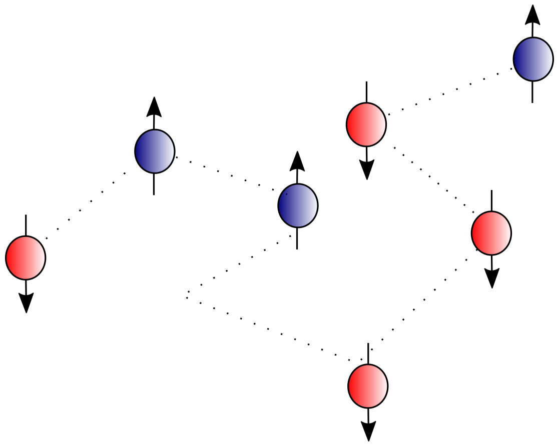

Figure 2.6: Simplified illustration of the EY mechanism. The electron changes direction during momentum scattering events, some of which result in a spin-flip. The average number of momentum scattering events required for a spin-flip to occur is determined by the spin-flip probability for that particular scattering mechanism.

2.6.2 Kondo Scattering

When some transition metal impurities are diluted in certain host metals they retain their magnetism. The condition for this to occur is most easily understood from the perspective of the Anderson or virtual bound state (VBS) model [86]. A localised d impurity level lying below the Fermi energy (ϵ_{F}) in the s bands of a host will hybridise with the itinerant s states. Hybridisation broadens and shifts the impurity level to a VBS with a width of $2\Gamma \approx 2\pi \mathrm{N}(\epsilon_{\mathrm{F}})|\mathrm{V}_{\mathrm{sd}}|^2$ and an energy of $\epsilon_{\mathrm{d}} \approx \frac{2\mathrm{N}(\epsilon_{\mathrm{F}})|\mathrm{V}_{\mathrm{sd}}|^2}{\mathrm{D}}$, where V_{sd} is the strength of the s-d hybridisation, D is the s bandwidth and $\mathrm{N}(\epsilon_{\mathrm{F}})$ is the density of states of the host at ϵ_{F}. The intra-atomic Coulomb repulsion between opposite spin electrons in the d impurity splits the VBS into spin-up and spin-down states by U_{dd}. For the impurity to retain a net magnetic moment, the occupancy of the spin-up and spin-down VBS must not be equal. The first factor to consider is whether the impurity states remain split; if the broadening and shifting of the VBS are stronger than the Coulomb repulsion, then the VBS will overlap in energy and the magnetic state collapses. If the VBS remain split, the position of the spin-split VBS relative to ϵ_{F} dictates whether or not the impurity retains a net moment. For example, if both the spin-down and spin-up VBS lie entirely below (or above) ϵ_{F}, the impurity will have no net moment. If not, the impurity will have a net moment, the magnitude of which

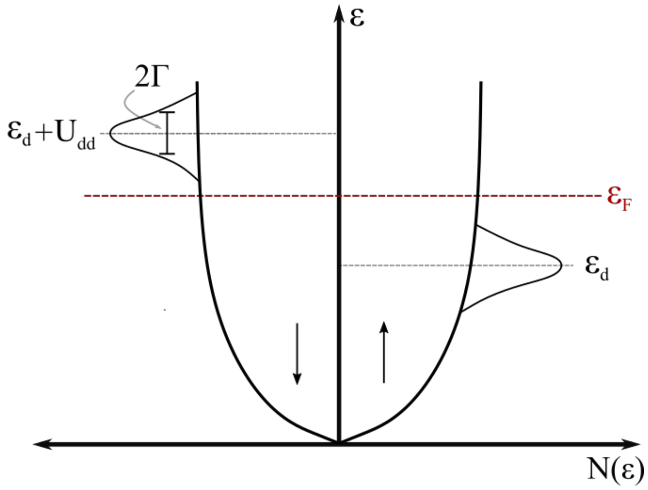

Figure 2.7: Simplified spin-dependent density of states for a free electron host metal. The impurity state has shifted and broadened due to s-d hybridisation, and then split due to the Coulomb interaction. This schematic shows the case for a well-defined impurity spin where one VBS (at ϵ_{d}) lies well below ϵ_{F}, thus is fully occupied, whereas the other VBS (at $\epsilon_{\mathrm{d}} + \mathrm{U}_{\mathrm{dd}}$) lies above ϵ_{F} and is unoccupied.

depends on the position of each VBS relative to ϵ_{F}. This condition is satisfied for Fe or Mn impurities in a Cu host [87, 88], whereas not for Fe in Al as both impurity states lie below ϵ_{F} [89, 90]. A schematic of a well-defined local moment is depicted in Figure 2.7, where the spin-up VBS is fully occupied and the spin-down VBS is unoccupied.

The interaction between this local impurity moment and the conduction electrons of the host leads to a number of peculiar phenomena, notably a logarithmic increase in the resistivity at low temperatures. The first successful theoretical treatment of this feature was by Kondo in 1964 [87] , from whom the 'Kondo effect' took its name. Kondo realised that unlike scattering from a NM impurity, which is a first-order process with four possible routes to take an electron from a state k to $\mathrm{k}^{'}$, the internal degrees of freedom of the magnetic VBS introduces an intermediate state q in the scattering process. Therefore, for each of the four first-order routes there are a further four scattering routes (two exchange and two direct) which differ in their intermediate states, but achieve the same end result. Due to the exclusion principle each path has a different probability and thus a different scattering amplitude [61]; the sum of which leads to a net contribution to the resistivity of:

$$\rho_{\mathrm{m}} = \rho_{\mathrm{k}} \ln(\mathrm{T}) \tag{2.21}$$

$$\rho_{\mathrm{k}} = \mathrm{c}[1 + \frac{3\mathrm{zJ}}{\epsilon_{\mathrm{F}}}] \frac{3\pi \mathrm{mJ}^2 \mathrm{S}(\mathrm{S}+1)(\mathrm{V}/\mathrm{N_T})}{2\mathrm{e}^2 \hbar \epsilon_{\mathrm{F}}} \tag{2.22}$$

where, c is the concentration of magnetic impurities, z is the number of conduction electrons per atom, V is the total volume of the crystal, $\mathrm{N_T}$ is the number of atoms in the crystal and S is the impurity spin. J is the direct exchange constant between the conduction electrons and impurity spin, which can be either positive (ferromagnetic coupling) or negative (antiferromagnetic coupling). Importantly, a negative J leads a logarithmic resistivity increase that has been experimentally observed at low temperatures. This logarithmic approximation breaks down as the temperature approaches the Kondo temperature:

$$\mathrm{T_K} \approx \frac{\epsilon_{\mathrm{F}}}{\mathrm{k_B}} \mathrm{e}^{-\frac{1}{|\mathrm{J}|\mathrm{N}}} \tag{2.23}$$

where, $\mathrm{k_B}$ is the Boltzmann constant and N is the conduction electron density of states at the impurity [90]. The exponential dependence on J means that $\mathrm{T_K}$ can vary from a few mK up to thousands of degrees [91]. Whilst T>>$\mathrm{T_K}$, conduction electrons are weakly scattered by the impurity spin. As T approaches $\mathrm{T_K}$, $\rho_{\mathrm{m}} \propto \ln(\mathrm{T})$ as in Kondo's original work. Once T<$\mathrm{T_K}$, conduction electrons start to screen the impurity spin and $\rho_{\mathrm{m}} \propto \mathrm{T}^2$, before finally reaching a plateau for T<<$\mathrm{T_K}$ where the impurity spin is screened entirely by the conduction electrons.

Manifestations of the Kondo effect are not exclusive to the resistivity. In the specific heat [92, 93] and thermopower [94–96] Kondo peaks appear at $\frac{1}{3}\mathrm{T_K}$ and $\mathrm{T_K}$ respectively. Furthermore, about two thirds of the Kondo resistivity involves spin-flipping events so it is a highly effective source of spin relaxation [89]. Manifestations of this ‘spin Kondo effect’ have been widely observed in measurements of $\Delta \mathrm{R_s}$ in LSVs [30, 78, 97, 98].

2.7 Thermal Effects

The use of a charge current to generate a pure diffusive spin current inevitably leads to a number of thermoelectric effects. Perhaps the most obvious is the Joule heat, where collisions between the electrons constituting the current and the ionic lattice result in a degree of energy loss according to $\mathrm{P} = \mathrm{I}^2\mathrm{R}$. The Joule heat is conducted into the substrate and throughout the device creating temperature gradients between the device, substrate and at the FM/NM interfaces. In this section we outline the relevant thermoelectric concepts.

2.7.1 Thermal Conductivity

The thermal conductivity of a material (k) defines the amount of heat flow (Q) generated by a temperature gradient (dt) across its length (dx) in the absence of current flow. Fourier's law of conduction states:

$$\mathrm{Q} = -k\frac{dt}{dx} \tag{2.24}$$

In a metal, the total thermal conductivity is the sum of the electron (k_e) and phonon contributions (k_p). Each contribution is roughly determined by the number of carriers, average velocity and mean free paths. In good metallic conductors, the thermal conductivity is dominated by the electronic contribution due to the high density of conduction electrons [99]. In these instances, $k \approx k_\mathrm{e}$ and the thermal conductivity can be estimated from the electrical conductivity (σ) using the Wiedemann-Franz Law:

$$k = \sigma \mathrm{LT} \tag{2.25}$$

where, L is the Lorenz number and T is the absolute temperature. The Sommerfield theory for a highly degenerate electron gas, which experiences only elastic scattering, proposes that L has a universal value for metals of $\mathrm{L}_0 = \frac{\pi^2}{3}(\frac{\mathrm{k_B}}{\mathrm{e}^2})^2 = 2.44\mathrm{x}10^{-8}\mathrm{V}^2/\mathrm{K}^2$. Measurements of L have shown that it is in fact both material, purity and temperature dependent; with values measured well above and below L_0. At very high ($\mathrm{T} > \Theta_\mathrm{D}$) and low temperatures, where the scattering is primarily elastic, this law is well obeyed with $\mathrm{L} \approx \mathrm{L}_0$. At intermediate temperatures, however, deviations from L_0 arise as a consequence of inelastic scattering or additional phonon contributions. The widely used equation for a temperature dependent L(T) which includes impurity and phonon scattering is given in equation 2.26 [94]. Although closer to reality than the Sommerfield model, it is based on a number of simplifying assumptions which dictate its validity for any particular material namely: an equilibrium phonon distribution; only normal electron-phonon scattering (no Umklapp); and, a spherical Fermi surface [94, 100].

$$\frac{\mathrm{L(T)}}{\mathrm{L_0}} = \frac{\frac{\rho_0}{\mathrm{K_{el-ph}}} + (\frac{\mathrm{T}}{\Theta_\mathrm{D}})^5 \mathrm{J}_5 \frac{\Theta_\mathrm{D}}{\mathrm{T}}}{\frac{\rho_0}{\mathrm{K_{el-ph}}}(\frac{\mathrm{T}}{\Theta_\mathrm{D}})^5 \mathrm{J}_5(\frac{\Theta_\mathrm{D}}{\mathrm{T}})[1 + \frac{3}{\pi^2}(\frac{\mathrm{k_F}}{\mathrm{q_D}})^2(\frac{\Theta_\mathrm{D}}{\mathrm{T}})^2 - \frac{1}{2\pi^2}\frac{\mathrm{J}_7(\frac{\Theta_\mathrm{D}}{\mathrm{T}})}{\mathrm{J}_5(\frac{\Theta_\mathrm{D}}{\mathrm{T}})}]} \tag{2.26}$$

Here, Θ_D is the Debye temperature; ρ_0 is the residual resistivity; $\mathrm{K_{el-ph}}$ is the electron-phonon contribution to the resistivity; $\mathrm{k_F}$ is the Fermi wave-vector, given by $k_F = (3\pi^2 n_e)^{\frac{1}{3}}$ (n_e is the number density of free electrons); and, $\mathrm{q_D}$ is the Debye wave-vector calculated from $q_D = \frac{\Theta_D k_B}{\hbar v_s}$ ($\mathrm{v_s}$ is the weighted average of the transverse and longitudinal sound velocities in the material). The integrals $\mathrm{J_n}$ are given by:

$$\mathrm{J_n}(\frac{\Theta}{\mathrm{T}}) = \int_0^{\frac{\Theta}{\mathrm{T}}} \frac{\mathrm{x^n e^x}}{(\mathrm{e^x} - 1)^2} dx \tag{2.27}$$

2.7.2 Seebeck and Peltier Effects

As inferred by the Wiedemann-Franz Law, there is an intrinsic link between electrical and thermal conduction, so temperature gradients (∇T) can be generated by potential differences (∇V) and vice versa. The relationship between charge and thermal transport within a metal can be represented by the coupled matrix:

$$\begin{pmatrix} \mathbf{J} \\ \mathbf{Q} \end{pmatrix} = \sigma \begin{pmatrix} 1 & S \\ \Pi & \frac{k}{\sigma} \end{pmatrix} \begin{pmatrix} \nabla V \\ -\nabla T \end{pmatrix} \tag{2.28}$$

where, **Q** is the heat current density, **J** is the electrical current density, σ is the electrical conductivity, S is the Seebeck coefficient (or thermopower) and Π is the Peltier coefficient. Considering first a ∇T across a metal, electrons at the hot end will have more energy resulting in a net migration of charge towards the cold end. As a result, an electric field builds until a dynamic equilibrium is reached which ensures the transfer of heat continues without a net movement of charge. With $\mathbf{J} = 0$ in equation 2.28 the potential difference formed is given by $\nabla \mathrm{V} = \mathrm{S} \nabla \mathrm{T}$. This is the Seebeck effect - the magnitude and sign of the Seebeck voltage depends upon S which is an intrinsic property of the material. To measure the Seebeck voltage a junction of two dissimilar metals (A and B) is required with different Seebeck coefficients $\mathrm{S_A}$ and $\mathrm{S_B}$ to prevent the thermal voltages from cancelling. A temperature gradient across the junction will produce a Seebeck voltage proportional to the effective Seebeck coefficient of the pair given by $\mathrm{S_{eff}} = \mathrm{S_A} - \mathrm{S_B}$.

The reverse effect - the generation of $\nabla \mathrm{T}$ in response to $\nabla \mathrm{V}$ - is called the Peltier effect. The Peltier effect produces a local heating/cooling at the interface between two dissimilar metals when an electrical current passes through it. This arises due to the difference in the heat currents associated with the electrical current within each metal, such that heat is either absorbed or emitted at the interface. It is linear to the current and completely reversible – which distinguishes it from Joule heating. Using $\nabla \mathrm{T} = 0$ in equation 2.28 the Peltier coefficient can be defined as $\Pi = \frac{\Delta \mathrm{Q}}{\mathrm{I}}$, so it is the heat absorbed (or emitted) per unit current. Due to Onsager reciprocity the Peltier and Seebeck effects are related to one another through the Kelvin relation: $\Pi = \mathrm{ST}$, where T is the absolute temperature [7].

CHAPTER 3

Methods

3.1 Introduction

This chapter outlines the techniques required to create and measure a functioning device. Device creation begins with lithography; the process of transferring a pattern onto a polymer coated substrate to form a device template. Following this, metallic elements are deposited into the template to form the device. The chosen deposition method depends on the required characteristics of the metallic elements, such as purity, roughness, step coverage and thickness. The first sections of this chapter detail the device design, lithographic techniques and deposition methods used in this work. In the latter sections the techniques used for device characterisation are presented, with particular attention placed upon the magnetotransport measurements that form the bulk of the results presented later in this thesis.

3.2 Fabrication

Fabrication is a challenging aspect of research focussed upon spin dependent effects, which are most easily observed as the dimensions of the device elements reach the nanoscale. Fabricating a device with such feature sizes requires a multi-step fabrication process. There are two aspects to the fabrication procedure: forming a working device; and, making electrical contact to that device. For the latter, contact is made to the device with well aligned microscopic wires that broaden to a macroscopic bonding pad allowing for a wire bond connection to be made to the measurement equipment. When patterning large areas, as for the bonding pads, optical lithography is favourable due to its high patterning speed and relatively low cost. However, optical methods are limited by the wavelength of the light and ergo incapable of the high resolution and alignment accuracy required to form the device (inner) contacts. Electron Beam Lithography (EBL) has a much higher resolution and is therefore ideal for the inner contacts; however, the cost and slow speed prevent the use of EBL for the entire contact area. Therefore, bridging this size gap requires breaking the contact into two separate lithography steps. First, a thin inner contact patterned with EBL and deposited by thermal evaporation, followed by a thicker outer contact patterned with optical lithography and deposited by sputtering. For the active device, if a transparent metallic interface between two different materials (as in lateral spin valves (LSV) and spin absorption devices (SAD)) was required an electron beam shadow lithography technique was used. Other devices, such as nanowires, where the active region consists of a single material were fabricated using conventional EBL. A schematic of a typical device chip with inner contacts, outer contacts and the device (in this instance an LSV) is shown in Figure 3.1. A general outline of the multi–step fabrication procedure for all the devices in this work is outlined below:

1. Patterning and deposition of inner contacts.
2. Bonding pads and outer contacts.
3. Active device patterning and deposition.

3.2.1 Device Design

To create a successful device there are two key considerations:

- How can the amount of spin current injected and detected by the ferromagnets (FM) be maximised?
- How may the reduction of the spin signal ($\Delta \mathrm{R_S}$) due to scattering within the non-magnetic (NM) transport channel be reduced?

These issues can partially be addressed through clever device design. For the latter, the inverse scalability of $\Delta \mathrm{R_S}$ with the volume of transport channel in LSVs has been demonstrated in a number of earlier experiments [101, 102]. However, this is only true to a certain limit. Once the channel dimensions approach the electronic mean free path (λ_e), electrons begin to ‘see’ the wire surface and experience additional scattering which is detrimental to the magnitude of $\Delta \mathrm{R_S}$. Both theoretical and experimental work on thermally evaporated Cu have shown that this limit lies around 100 nm [51, 101]. Therefore, the patterned width ($\mathrm{w_{NM}}$) and thickness ($\mathrm{t_{NM}}$) of all the NM channels were 100 nm. The efficiency of spin injection and detection in metallic devices with transparent interfaces can be manipulated by varying the relative spin resistances ($\mathrm{R_S}$) of the device elements. A device element with a low $\mathrm{R_S}$ acts as an efficient spin sink, and is a preferred path for spin relaxation. At the injecting interface, the low spin resistance of the FM ($\mathrm{R_{FM}}$) compared to the NM channel ($\mathrm{R_{NM}}$) reduces the efficiency of spin injection as spins backflow into the FM. Through geometrical means this can be partially alleviated. As $\mathrm{R_{FM}} \propto \frac{1}{\mathrm{w_N w_{FM_1}}}$, reducing $\mathrm{w_{FM}}$ can increase $\mathrm{R_{FM}}$, without

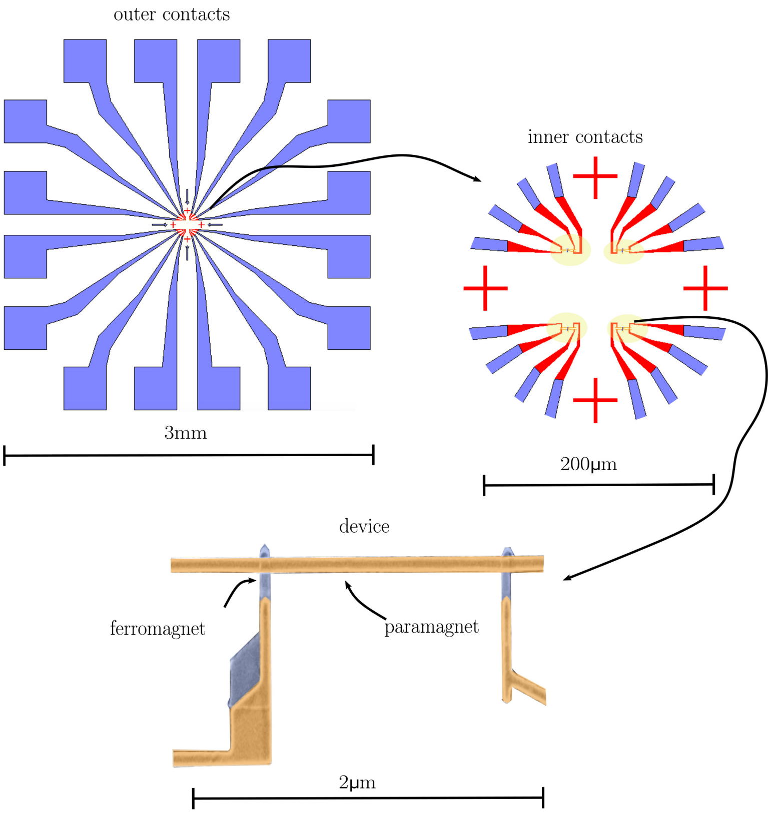

Figure 3.1: Schematic of a typical LSV chip. The outer contacts (blue) overlap with inner contacts (red), decreasing in size as they move toward the centre of the chip where they contact one of the four devices at the centre. This chip is one of a grid of nine on the same substrate, all of which are fabricated and deposited together, and then diced into separate smaller chips at the end of the process.

affecting R_{NM}, and reduce the severity of the spin backflow [51, 69]. This technique has proved successful, exponentially increasing the injected spin polarisation in Py/Cu LSVs [103]. Conversely, to improve the detection efficiency, spin absorption into the detecting FM must be maximised so a larger interface is preferred. Based on the above, the injecting and detecting FM widths were chosen to be 80 and 100 nm respectively. Additionally, to measure ΔR_S, the electrodes were designed to have different switching fields such that the magnetisations could be aligned both parallel (P) and anti-parallel (AP) to one another. To achieve this, a nucleation pad was added to the wider detecting electrode (FM_2) to induce a clean, fast magnetisation reversal through the injection of a single domain wall. The addition of this pad also further lowered the coercivity of

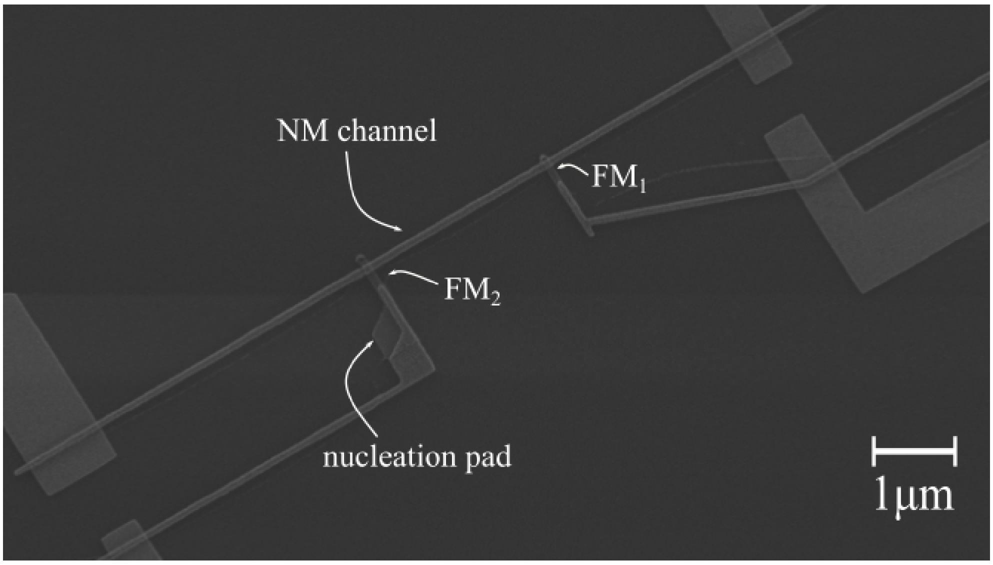

Figure 3.2: Scanning Electron Microscopy (SEM) image of a typical LSV; the active device is in the central region of the image. The positions of the injector (FM$_1$), detector (FM$_2$), the NM transport channel and the nucleation pad on FM$_2$ are labelled.

FM$_2$ and increased the field window of the AP state. A typical example of a fabricated LSV is shown in Figure 3.2. K-Layout software was used to design the patterns for all the devices and contacts.

3.2.2 Lithography

A general lithographic procedure is as follows: a resist is spin coated onto a substrate, exposure to a stimulus (light/electrons) alters the chemistry of the exposed region, the exposed/unexposed areas for positive/negative resists are then removed using a developer solution leaving behind the desired pattern ready for material deposition. After deposition in a 'lift off' step, the resist is removed by submerging the sample in resist remover; hopefully leaving behind the desired structure. In this section, the preparation of resists and the patterning techniques used in this thesis are outlined.

Resists

The first step in any lithography process is to spin coat a resist onto the substrate. A resist is a viscous solution comprised of a polymer, that is sensitive to either light or electrons, and a solvent to adjust the viscosity. Spin coating is the process of spreading an even layer of the resist upon the substrate; the chosen rotation speed and time determines the resist thickness. Following this, the resist is baked to evaporate some of the solvent and harden the resist. For a positive resist, the regions exposed to the patterning stimulus become soluble in a development solution and are removed. The result is a stencil, ready for deposition. The use of a bilayer resist is generally preferred as it allows a resist profile undercut to be formed. This reduces the chance of material depositing up the resist walls and forming sharp edges called 'ears', which adhere to the substrate and interfere with subsequent lithography steps. A comparison between a single resist (composed of Methyl Methacrylate (MMA)) and bilayer resist (MMA lower layer and Poly Methyl Methacrylate (PMMA) upper layer) is depicted in Figure 3.3.

Electron Beam Lithography Resists

For all EBL processes a bilayer resist consisting of a electron sensitive under layer, MMA, and a high-resolution upper resist layer, PMMA, was used. Upon exposure to electrons MMA requires less exposure than PMMA to become soluble in the developer solution, so naturally an undercut will form. The EBL resist preparation process was as follows:

1. An Si/SiO$_2$ substrate was baked at 180 °C for 5 minutes to dehydrate.
2. After cooling, MMA (MAA(8.5)EL11) was spin coated at 4000 rpm for 40 s to achieve a thickness of approximately 500 nm.
3. The resulting MMA (MAA(8.5)EL11) layer was baked at 180 °C for 5 minutes and then cooled for 30 s.
4. PMMA (950k) was spun on top with the same spin coater settings to achieve a thickness of 200 nm.
5. A final bake at 180 °C for 5 minutes produced the desired bilayer resist.

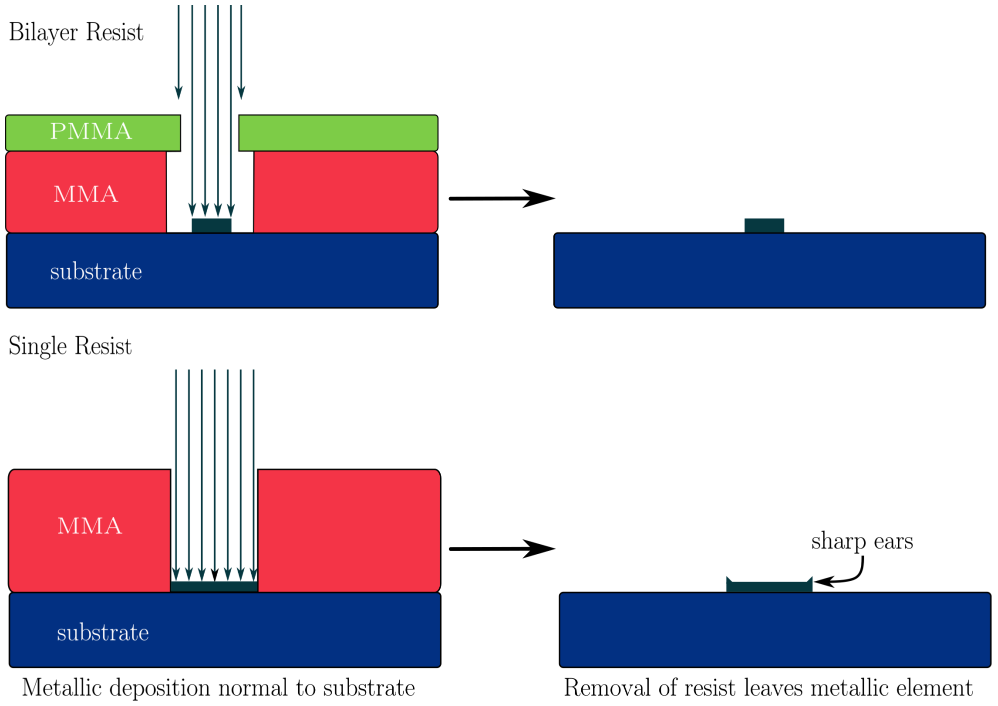

Figure 3.3: A comparison between the resulting structures that form using a bilayer resist and a single resist. The formation of the undercut in the bilayer case prevents material from depositing on the base of the resist walls. This means a clean lift off profile for both directional and non-directional (e.g. evaporation and sputtering) deposition techniques. Conversely, single resists can suffer from sharp edges and left over hardened resist around the structure which can interfere with subsequent lithographic steps.

Optical Resists

A bilayer system was also employed for the optical lithography in this work. In this case, the base layer (LOR 3A) is not photosensitive and the undercut forms as a result of the development process. The upper layer (S1813) is photosensitive and defines the patterned features. During development, the exposed regions of upper S1813 layer are dissolved allowing the developer to degrade the LOR 3A in the open regions. Baking temperature and times control the rate of degradation of the LOR 3A and were optimised to produce a sufficient undercut for a good lift off result. The procedure was as follows:

1. An Si/SiO$_2$ substrate (with deposited inner contacts) was dehydrated for 5 minutes at 180 °C.
2. LOR 3A was spin coated at 4000 rpm for 40 s.
3. LOR 3A was baked at 200 °C for 5 minutes.
4. S1813 was spin coated at 4000 rpm for 40 s.
5. A final bake at 110 °C for 3 minutes produced the desired bilayer resist.

Lithographic Techniques

Electron Beam Lithography

EBL is a high-resolution patterning method which uses a focused electron beam to create patterns in an electron sensitive surface. The system used in this research was a 100 kV JEOL JBX-6300FS, which has a Schottky type emitter electron gun. In this type of gun, a sharp ZrO coated W tip is heated at a lower temperature than the temperature required to produce thermionic emission. A strong electric field is applied to lower the potential barrier for electrons to escape the tip. This electron beam then passes through a number of alignment coils and acceleration electrodes before arriving at the optics. Here, a number of electromagnetic lenses focus the electron beam and provide stigmation correction. A blanking aperture allows the beam to be blocked when necessary. A final set of optics control the x, y position of the beam relative to the substrate and moves the beam in a raster fashion to pattern the desired areas.

Both the inner contacts and single metallic devices (nanowires) were patterned using conventional EBL. The resist was prepared as outlined in the previous sections, and the patterning and development process was as follows:

1. Exposure on the JEOL JBX 6300FS system. In order to produce the desired pattern simulations were performed using BEAMER software to obtain proximity error corrections and tailor the local dosage to the feature density and size. Beam currents and dosages varied, but were generally 10 nA and 440 μC/cm^2. All data collection, simulations and patterning during this step were performed by Dr M. Rosamond. For device patterning, as no regions of the structure were visible with an optical microscope, a visible test structure was patterned away from the active device to assist in determining development times.

2. To develop the pattern the substrate was submerged in Isopropanol (IPA) / deionised H_2O (7/3) solution and rinsed in IPA. Development was performed in regular intervals (5 to 40 s) and the structure (or test structure, depending on the feature size) was examined under an optical microscope. For the inner contacts, development was complete when no traces of resist remained in the largest exposed regions. For a device, development was performed until the test structure was fully developed.

3. To remove any residual resist in the patterned channels the substrate underwent an O_2 plasma ash at 50 W for 20 s. Following this, a Radio-Frequency (RF) Ar etch at 4 mTorr, 50 W was perfomed in a high vacuum (HV) sputter system to further remove the resist residues (the etching process is discussed further in section 3.2.3).

4. Material deposition was then performed. Active devices (nanowires) were deposited in a ultra high vacuum (UHV) chamber using electron beam evaporation. For the inner contacts an Edwards thermal evaporator with a base pressure of 1x10^{-6} mBar was used to deposit Cr/Au (5/30) nm. More details regarding the deposition methods used are provided in section 3.2.3.

5. Finally, the resist was removed in a lift off step by submerging the sample in pre-heated acetone at 60 °C for approximately 10 minutes.

Optical Lithography

Optical lithography transfers a pattern onto a photoresist coated substrate using actinic optical radiation. Either a physical mask consisting of optically opaque regions is used to define the exposure pattern, or a laser raster across the photoresist to replicate a computer generated pattern. In this work, a physical mask of Cr etched on quartz with an alignment and exposure system was used. The equipment used, a Karl Suss MJB 3 Mask Aligner, was equipped with a 350 W Hg arc lamp producing a wavelength of 405 nm and a typical intensity of 20 mW/cm^2. Depending on the combination of resist, mask to substrate distance and development process the aligner was capable of achieving features down to 1 µm. Optical lithography was used to define the outer contacts which had feature sizes between 1 and 100 µm. This formed the second step in the fabrication process, so had to be aligned to the first step (inner contacts). To achieve this, a series of alignment markers were patterned with EBL along with the inner contacts which corresponded to markers etched on the physical mask. Viewing the mask and substrate from above through an optical microscope (with 50x, 100x lenses), the mask was moved in the x and y axes until patterned markers coincided with the corresponding transparent regions in the mask. The optical lithography procedure was as follows:

1. The substrate was prepared as described in the optical resists section.
2. Patterned markers on the substrate were aligned with the corresponding transparent regions on the mask. The mask and substrate were brought into hard contact to reduce pattern distortion from diffraction. Once in hard contact, the mask and substrate were exposed to light with the exposure time tailored to achieve a dose of 400 mJ/cm^2.
3. The pattern was developed in MF319 until the large bonding pads were clear of resist (1-2 minutes) and rinsed in de-ionised H_2O.
4. Deposition of Cr/Au (5/100) nm in a Physical Vapour Deposition (PVD) sputtering system (described in more detail in section 3.2.3.).
5. Finally, lift off was performed in micro deposit remover 1165 (NMP) at 75 °C, followed by a rinse in de-ionised H_2O and dried with compressed N_2.

Shadow Lithography

To produce both the LSV and SAD devices in this work an unconventional method called shadow lithography was used. As the name suggests, the technique relies on the fabrication of suspended regions of resist that shadow parts of the substrate. Depositing materials at different angles with a shadowed resist allows for junctions between the two to be formed in a single step. This eliminates the need for two separate lithography stages with an intermediate interface cleaning inert gas etch, which is somewhat effective but susceptible to interface damage and inconsistencies. Shadow lithography is therefore an attractive alternative to produce high quality transparent interfaces; a key requirement for efficient spin current injection/detection at FM/NM interfaces. The same MMA/PMMA bilayer resist is used as described in the previous sections. In conventional EBL, a constant electron dose naturally leads to an undercut in the vicinity of the exposed regions due to the difference in electron sensitivity of the two layers. Here, we exploit this difference further by varying the electron dose to either: degrade both PMMA and MMA layers using a high electron dose; or only degrade the MMA using a low electron dose (see Figure 3.4).

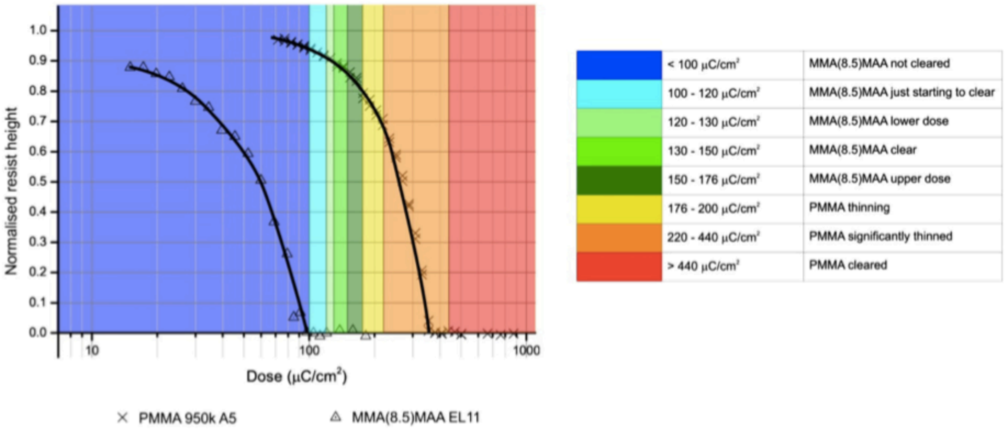

🟦	< 100 μC/cm²	MMA(8.5)MAA not cleared
🟦	100 - 120 μC/cm²	MMA(8.5)MAA just starting to clear
🟩	120 - 130 μC/cm²	MMA(8.5)MAA lower dose
🟩	130 - 150 μC/cm²	MMA(8.5)MAA clear
🟩	150 - 176 μC/cm²	MMA(8.5)MAA upper dose
🟨	176 - 200 μC/cm²	PMMA thinning
🟧	220 - 440 μC/cm²	PMMA significantly thinned
🟥	> 440 μC/cm²	PMMA cleared

(a) (b)

Figure 3.4: The effect of electron dose on MMA and PMMA resists. The resist height is normalised to the initial value prior to exposure. A dose >440 μC/cm^2 is required to clear the PMMA and was chosen as the high dose. A lower dose of (120-130) μC/cm^2 can effectively clear the MMA with minimal thinning to the PMMA, taken from [2].

A low dose therefore creates suspended regions of resist, which will only be depos-

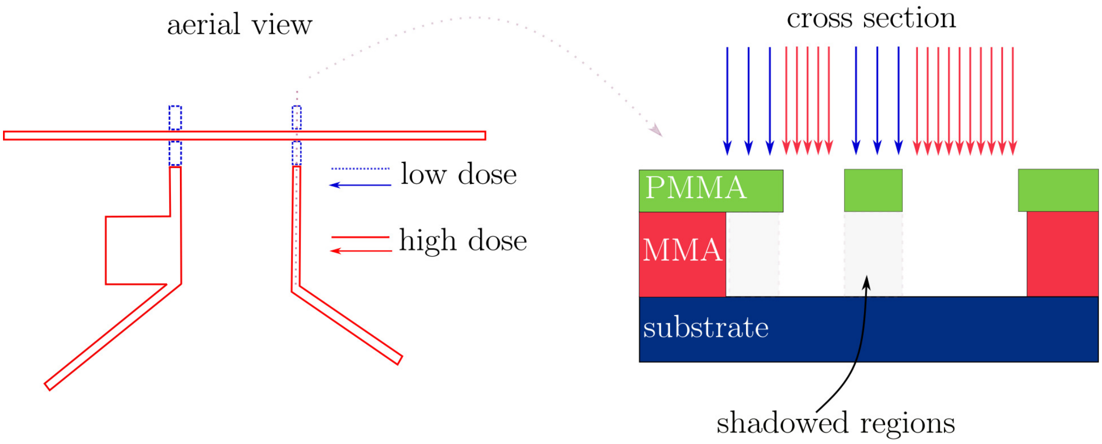

Figure 3.5: Aerial view of K-Layout design of an LSV indicating regions of high and low electron doses. Cross section along the dotted line at the interface shows the formation of the shadowed regions.

ited underneath if material is evaporated at an angle. As shown in Figure 3.5, these suspended regions are used to define the FM electrodes which are deposited at an angle. The high dose defines the regions where the NM material is deposited, normal to the substrate. Corrections to the dosage were required to account for the additional scattering effects produced within the resist (which can overexpose low dose areas if they lie close to high dose areas) and were performed by Dr M. Rosamond using a 3D Proximity Correction with BEAMER software, in addition to the patterning itself [2].

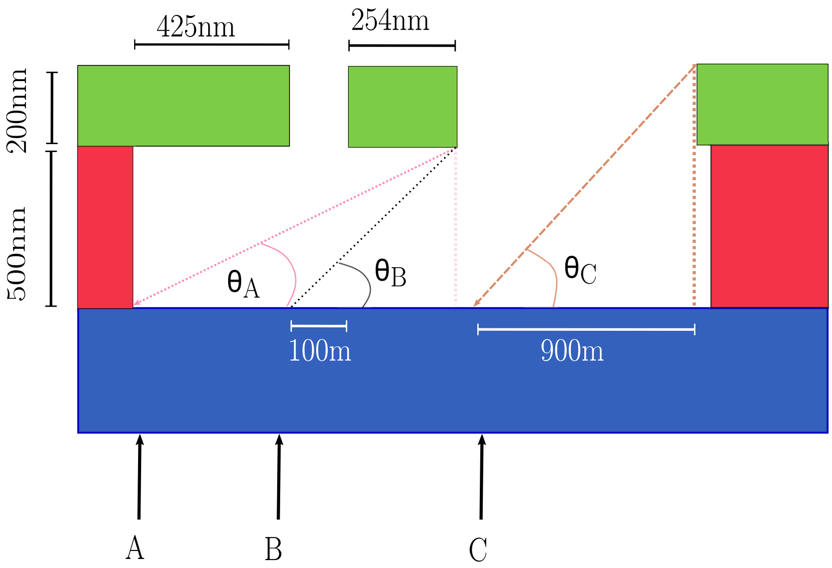

Figure 3.6: Cross section of developed shadow mask along the FM electrode and NM channel intersection. Horizontal lengths are taken from device design and resist thicknesses are approximate.

Deposition Angle

The developed resist properties such as the thickness of MMA and PMMA layers, protrusion of the overhang and feature sizes are required to determine the shadow deposition angles. Figure 3.6 is a schematic of the cross section along one of the FM electrodes (see Figure 3.5) and illustrates the conditions that have to be met for the chosen FM deposition angle:

- FM material cannot extend past point A, as any material deposited up the resist wall will introduce problems when attempting to lift off.
- FM material must extend across the NM channel to produce a continuous interface, the minimum position for this is point B.
- Electrical contact must be made with the NM contact, so the FM must begin no further than point C.

Basic trigonometry may be used to determine the angles corresponding to material reaching the points A, B and C. The resulting angles are as follows: θ_{A}=32.7°;

θ_B=54.7°; and, θ_C=37.7°. Based on the conditions described above, the deposition angle (θ_D) must obey $\theta_D>\theta_A$, $\theta_D>\theta_C$ and $\theta_D<\theta_B$. Therefore, 37.7°$<\theta_D<$54.7°. Feature sizes and resist thicknesses inevitably will vary from the estimates shown in Figure 3.6, so θ_D=45.0° was chosen to remain safely within the determined limits.

Shadow Lithography and Deposition Overview

The shadow lithography and deposition process was as follows:

1. Resist prepared as described in the EBL resists section.
2. Exposure on the JEOL JBX 6300FS system as described in the Shadow Lithography section.
3. To develop the pattern, the substrate was submerged in IPA/ de-ionised H_2O (7/3) solution and rinsed in IPA. Development was performed in regular intervals (5 to 40 s) until the test structure (and device) was fully developed.
4. To remove any residual resist in the patterned channels, the substrate underwent an O_2 plasma ash at 50 W for 20 s. Following this, a RF Ar etch at 4 mTorr, 50 W was conducted in a HV sputter system to further remove the resist residues (described in more detail in section 3.2.3).
5. Material deposition was then performed in a bespoke UHV chamber with angular control of the substrate (discussed in more detail in section 3.2.3). The FM was deposited at 45° (15 or 30 nm) using electron beam evaporation, followed by the thermal evaporation of the NM (100 nm).
6. Lift off was then conducted in pre-heated acetone at 60 °C with persistent agitation with a pipette.
7. Finally, devices were protected with 500 nm coating of MMA (MAA 8.5 EL11) which was air-dried.

3.2.3 Deposition Techniques

Magnetron Sputtering

Sputtering is a form of PVD where material atoms are ejected from a target through bombardment with an inert working gas, most commonly Ar. This process is performed within a HV chamber, with material targets housed in guns at the chamber base and the substrate suspended above (see Figure 3.7). A combination of roughing and turbomolecular pumps are used to reach a vacuum of at least 1x10^{-6} mbar, after which Ar is bled into the chamber at a fixed flow rate. To start the sputtering process, a plasma is generated by the application of a large electric field between the target and the gun shield. The plasma consists of light, quick electrons and heavy Ar^{+}. As the target material (cathode) is negatively charged, the heavy Ar^{+} ions are accelerated towards it and bombard the surface. If they have sufficient kinetic energy the atoms of the target material will be expelled in all directions, some of which will settle upon the substrate to form a deposited film. A number of secondary electrons are produced in the bombardment process, which in direct current (DC) planar sputtering are not used to their full potential to maintain the plasma and instead stray into the chamber. In magnetron sputtering, as in this work, a magnetic field is generated by an array of magnets behind the target, which in conjuction with the applied voltage confines these secondary electrons to the target surface and enhances the ionisation of the Ar atoms and thus the rate of sputtering. Compared to regular sputtering, much lower voltages (a few hundred V instead of thousands) are required to maintain a high sputtering rate. Both methods are forms of DC sputtering that are suitable for conducting targets only. The use of DC sputtering with insulating or semiconducting targets results in a positive charge accumulating on the target that halts the sputtering process. RF sputtering must be used for these materials; where an alternating current (AC) alters the polarity of the accelerating potential and prevents this charge build-up. Inevitably, this also bombards the substrate with Ar^{+}. This bombardment essentially etches the substrate and/or deposited material removing any oxidised layers and/or resist residues. This RF etch method was key to produce low resistance interfaces between subsequent contact patterning steps and to remove any residual resists in the patterned channel that could prevent deposited material from adhering to the substrate. Sputtering was chosen as the deposition method for the optical outer bonding pads (device fabrication step 2) as it is fast, provides good step coverage and the PVD system allows for an in situ RF

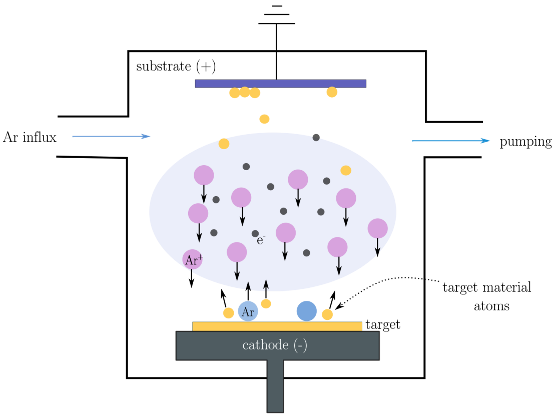

Figure 3.7: Schematic of sputtering system. Influx of Ar atoms (in blue) are ionised by high potential difference across anode and cathode. The plasma generated is indicated in light blue and consists of Ar^+ (purple) and e^- (black).

Ar etch to produce ohmic interfaces between the inner and outer contacts.

Sputtering Process

1. Sample loaded in the HV chamber and pumped to a base pressure of $1x10^{-6}$ mBar.
2. RF etch. Ar was bled in with a flow rate of 10 standard cubic centimetres (sccm) and an AC bias applied at 50 W for 20 s.
3. Deposition. Flow rate reduced to 8.2 sccm. Cr was deposited to achieve a thickness of 5 nm. Following this, Au was deposited to obtain a film thickness >100 nm.

Evaporation Techniques

Electron beam and thermal evaporation were chosen as the deposition methods for the sub-micron features in all devices; the active part of the device and the inner contacts. These techniques are directional (can be seen as a point source) and e-beam methods are capable of depositing high melting point metals. Additionally, evaporation may be achieved in an UHV system without the introduction of a working gas. By removing the residual gases from the growth chamber a higher quality of deposited material can be achieved. This is of key importance for spin transport where impurities and structural defects can have disastrous consequences for spin coherence.

Electron Beam Evaporation

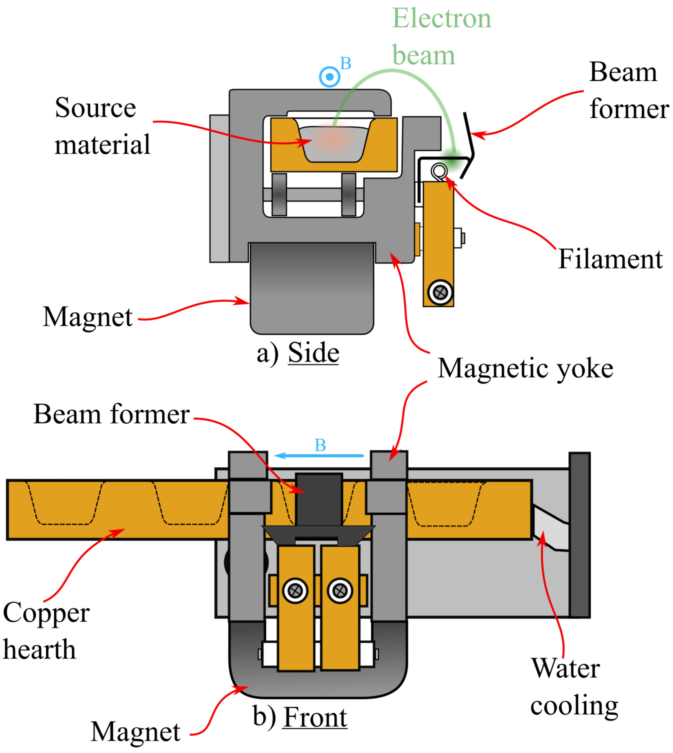

Figure 3.8: Schematic of e-beam gun used in UHV evaporation system. The H_2O cooled Cu hearth houses four material sources and can be moved along bellows until the desired source is centred between the magnetic yokes, taken from [3].

In electron beam evaporation a beam of electrons is used to melt the source material; a schematic of the e-beam gun used is depicted in Figure 3.8. The electrons are generated through thermionic emission by passing a high current (10 A) through a resistive W filament. The emitted electrons are accelerated and deflected towards the Cu hearth by a high voltage (-7 kV) across the filament and beam former. A series of magnets curve the electron beam and direct it to impinge on the source material. Additional beam manipulation, such as centring, is provided by magnets outside the UHV system.

The kinetic energy of the electrons is controlled by varying the accelerating voltage and the emission current controls the energy of the total beam. The general procedure was to increase the emission current (typically 100 mA) with the acceleration voltage fixed until sufficient energy had been supplied to melt the source. Additional external magnets were used to deflect stray electrons and ionised particles emanating from the electron gun in order to prevent damage to the resist from unwanted crosslinking of the polymers. This method was used to evaporate the CoFe used as the FM throughout this study.

Thermal Evaporation

A typical effusion cell (or Knudsen cell) consists of a central ceramic crucible which is filled with source material and surrounded by a meandering resistive filament. When a current is passed through the filament, Joule heating warms the crucible and source material to its melting point. At the top of the crucible a small ceramic disk with a hole at the centre allows evaporated material to escape into the deposition chamber and deposit onto the substrate. This method was used to deposit the Cu which formed the NM transport channel in all devices.

Bespoke Angled Deposition System

The above evaporation methods were both performed in a bespoke UHV deposition chamber (schematic in Figure 3.9, built specifically for the purpose of shadow deposition. The most important aspects of this system are the low base pressure ($1\text{x}10^{-10}$ mbar) and the angled manipulator which will be described in detail in the following section.

To achieve the low base pressure careful maintenance along with a variety of different pumps were required. The main chamber was pumped on by a large oil-based diffusion pump, filled with liquid N_2 to prevent the backflow of oil into the main chamber and backed by a roughing pump. A turbo pumped load lock, separated from the main chamber by a gate valve, allowed substrates to be loaded into the deposition system without exposing the main chamber to atmosphere each time. After exposure of the main chamber to atmosphere for maintenance, the system was baked to release any adsorbed gases in the chamber walls and all sources were thoroughly outgassed.

Prior to a growth, substrates were secured with Kapton tape (UHV compatible) onto

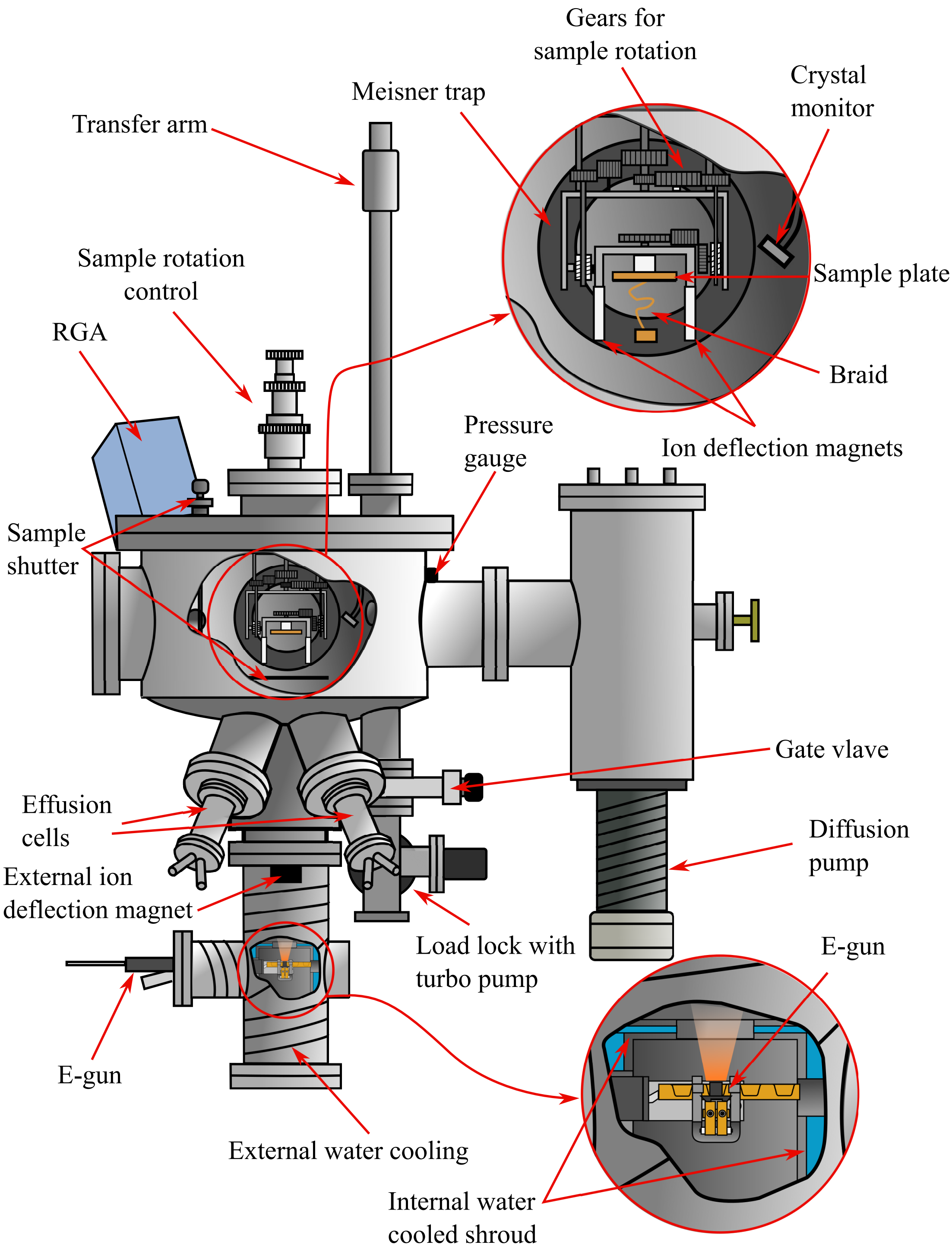

Figure 3.9: Bespoke UHV deposition system which housed two Knudsen cells and an e-gun, taken from [3]

a Cu sample holder that was designed to fit into the jaws of the angled manipulator, and loaded into a carousel in the load lock. Once the load lock has reached a pressure of $\approx$1x10^{-8} mbar, the gate valve was opened, and the carousel was raised into the main chamber using a linear transfer arm. Individual sample plates were transferred using a wobble stick from the carousel into the jaws of the angled manipulator. A meisner trap was filled with liquid N_2 which removed residual gases and water vapour from the chamber, in addition to cooling the sample holder as it was connected to the manipulator by a Cu braid. This additional cooling was incredibly important for lithographic samples, as resists can reflow and deform the pattern if the temperature exceeds 100 °C; a temperature that can easily be reached during deposition. The manipulator was designed to rotate the sample in two orthogonal planes with a precision of 1°, with manual rotation control outside the chamber. Pressures in the main chamber were monitored using an ion gauge (total pressure) and a residual gas analyser (partial pressures). Deposition rates were monitored using a crystal monitor inside the main chamber, and tended to be (0.05-0.2) Å/s for both Cu and CoFe.

3.3 Measurement Techniques

A variety of characterisation techniques were used, the most important of which were magnetotransport measurements. Other techniques, such as atomic force microscopy (AFM) and scanning electron microscopy (SEM) were used to inspect the appearance of the patterned devices, measure geometry and determine material thicknesses to input into data analysis; these techniques will be discussed briefly at the end of this section.

3.3.1 Magnetotransport

Magnetotransport measurements were performed from 4 to 275 K with the spin signals of interest generally lower than 1 μV. Additionally, owing to the small dimensions of the devices, any static shocks generated by moving cables could be detrimental. Therefore, special precautions were taken to improve the signal to noise ratio, prevent spurious effects from temperature changes and protect the devices from static. These included the use of a specialised measurement stick (designed and built by G. Stefanou) and the design and build of a complementary measurement head by the author.

Measurement Stick

A schematic of the measurement stick is depicted in Figure 3.10. The main body of the stick consisted of two long NM steel coaxial tubes, a breakout box mounted at the top and a 24-pin Lemo at the bottom. At the breakout box there were 20 available BNC connections corresponding to 20 signal lines (Cu wires) running down the stick, each connecting to a pin in the Lemo. The wires were in 12 twisted pairs, in a loom, which was non–inductively wound around the exterior of the inner tube and secured with GE varnish. Current (I) and voltage (V) lines were separated from one another by the 2 spare twisted pairs. The breakout box also split the Triax current input into I^+ and I^- and the Lemo voltage output into V^+ and V^-. Using BNC cables, connections were made to the desired signal lines on the breakout box from the I and V input and output. To reduce noise from the thermometry lines, they were isolated from the signal lines as much as possible; bypassing the breakout box and entering the inner tube through a 4-pin Lemo connector. Four thermometry lines were used to take a 4–point resistance measurement of the thermometer, which was calibrated against a standard thermometer. Another two current lines ran down the inner tube for the custom built heater on the sample head, which is described in greater detail in the next section. Heat sinking and InAg solder were used to minimise any electromotive forces (EMFs). Baffles were also soldered between the inner and outer tubes to provide radiation shielding for the signal lines and avoid pressure build-up within the stick.

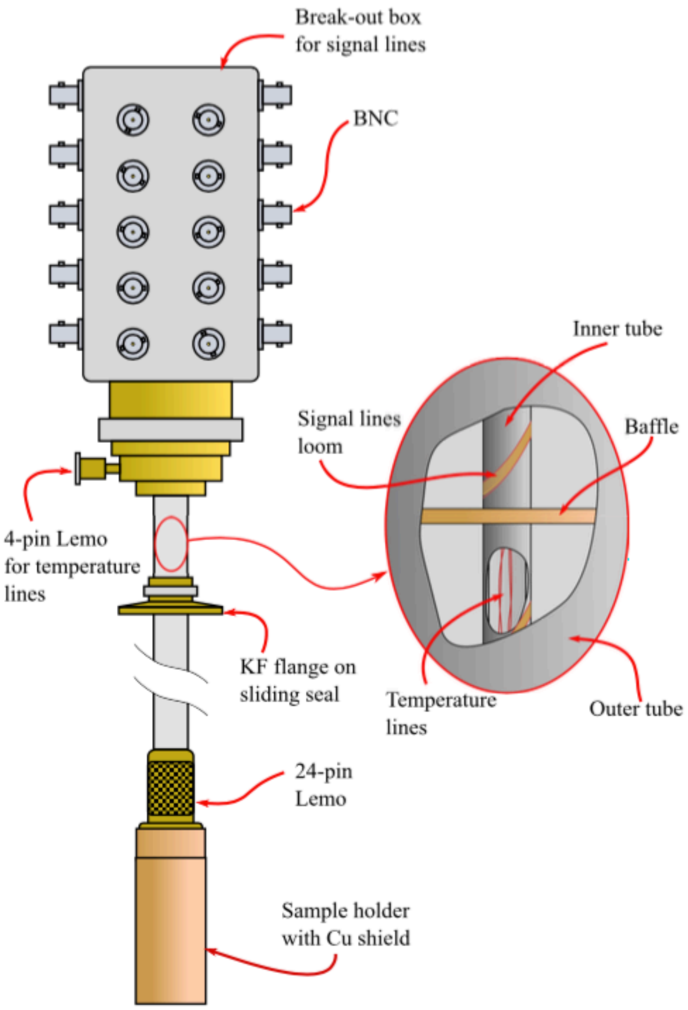

Figure 3.10: A schematic of the measurement stick used for transport measurements. The sample was mounted onto the sample holder at the bottom of the measurement stick and lowered into the variable temperature insert (VTI) of a He flow cryostat, allowing the measurement temperature to be varied between 300 and 1.5 K; taken from [3].

Measurement Head

A schematic of the measurement head is depicted in Figure 3.11. Due to its high thermal conductivity and NM properties, a single piece of O_2 free Cu was used to construct the body of the measurement head. To be compatible with the measurement stick described in the previous section, each of the signal and thermometry lines entered the Lemo as a designated pin. From each Lemo pin, a solder connection was made to a Cu wire (which were in twisted pairs) and these wires separated into groups: 8 signal current lines; 8 signal voltage lines; 4 thermometry (2 I and 2 V) lines; and, 2 heater lines. Each group followed a different path through the body of the head and had separate heat sinks in an attempt to isolate them from one another and reduce noise. The two largest heat sinks at the Lemo were for the signal current and voltage lines. Within the body of the head, thermometry lines were wound around two heat sinking posts (one for each I and V) before making a solder connection to the thermometer. The thermometer was mounted using GE varnish onto the Cu pillar, just below where the sample was mounted. The signal lines emerged separately from each heat sink through a hole within the body of the head. Once in the main body, the lines followed isolated paths (adhered to the body of the head using GE vanish) towards holes in the sides where they exited and were soldered to the correct signal line on the printed circuit board (PCB) above. On the PCB, each solder connection was made to a Cu track which led to one of 16 bonding pads for the sample. Wire bonding connections were then made between the bonding pads on the head and the outer contact bonding pads patterned on the sample. The heater was a custom-made element made from In wire that was non-inductively wound into a meandering filament with a 20 Ω resistance and adhered with varnish to the bottom of the head.

As the spin related signals of interest were generally smaller than a μV, they could easily be masked by spurious thermoelectric signals arising elsewhere in the measurement circuit. Given that the circuit started at the external measurement equipment (at ambient temperature) and led to the device (possibly at cryogenic temperatures), we needed to minimise the possibility of these large temperature gradients creating EMFs. Based on information from [104], a number of steps were taken to avoid this. Firstly, wiring from ambient temperature passed through a number of heat sinks to reduce the temperature gradient from room temperature to the device under test (DUT). Additionally, the sample was thermally anchored to a Cu pillar in the sample holder with conductive silver paint. Other common sources of noise (and offsets) included Radio Frequency Interference (RFI) and Electromagnetic Interference (EI). RFI and EI contributions were minimised through physical shielding around the DUT and the use of twisted wiring pairs.

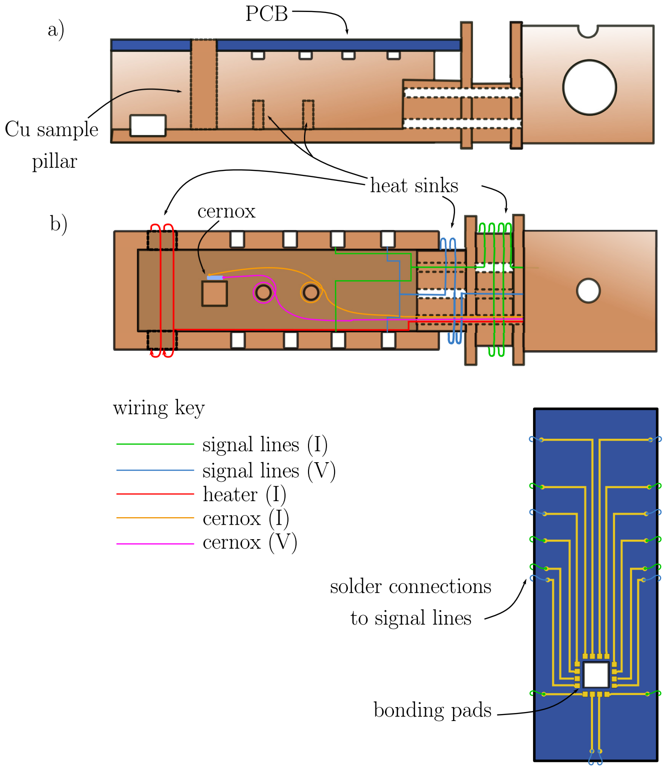

Figure 3.11: (a) A side view of the body of the measurement head. The Cu sample pillar was designed to fit into the square hole in the PCB (shown in lower part of figure), allowing for wire bonding connections to be made from the sample mounted on the pillar to the bonding pads on the PCB. (b) A view of the measurement head from above depicting the path taken by each group of lines through the body of the head. The heating element sits on the base of the head and is not shown in this schematic.

He Flow Cryostat

All transport measurements were performed in an Oxford instruments He flow cryostat depicted in Figure 3.12. Central to the cryostat was the variable temperature insert (VTI) which sat within a He bath. To isolate the He reservoir from ambient temperatures and prevent excessive evaporation, it was surrounded by a vacuum jacket and an external reservoir of liquid N_2. A solenoid magnet lay within the He bath which was capable of supplying magnetic fields up to 8 T. Temperature control within the VTI was achieved through varying the He flow through an adjustable needle valve, pumping speed and heater settings.

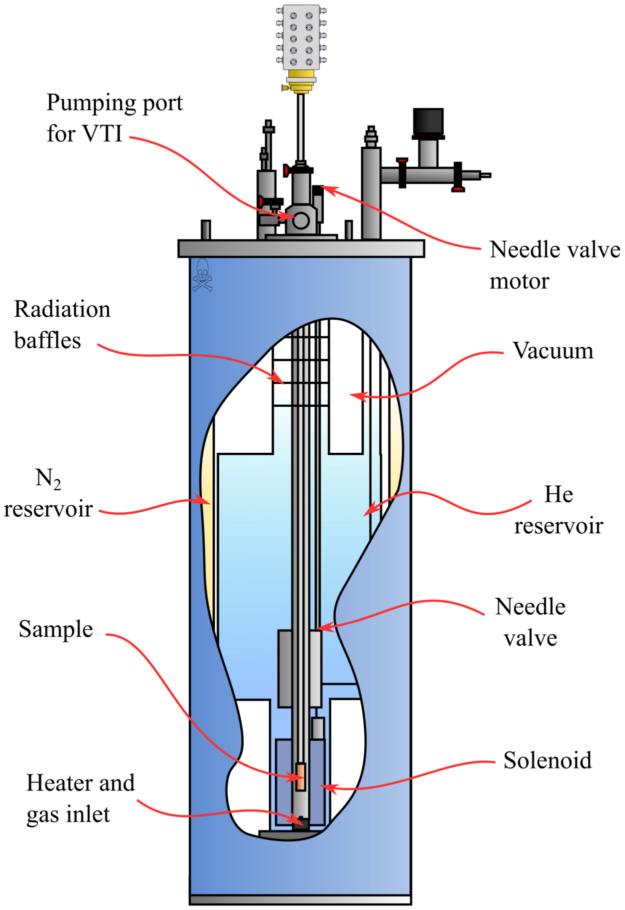

Figure 3.12: Schematic of the cryostat used for transport measurements. The measurement stick, with sample holder attached to the lower end, is lowered into the VTI until the sample sits in the centre of the solenoid, taken from [3].

Magnetotransport Measurement Procedure

Transport measurements were taken by applying a current and measuring a voltage. As the devices measured in this work had low resistances (R_{DUT}) compared to the measurement leads (R_{lead}) a four-point measurement was used throughout to avoid contributions from R_{lead} and contact resistances. Four leads were used to connect a voltmeter in parallel to the DUT and current source as depicted in Figure 3.13.

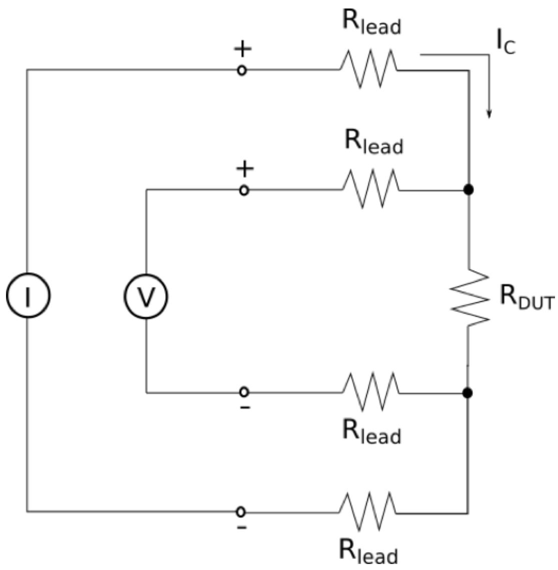

Figure 3.13: Schematic of a four–point measurement configuration. Four leads (with resistances of R_{lead}) are used to connect the current source and voltmeter to the device under test (DUT). The current and voltage leads are the outer and inner pairs respectively. As the voltmeter has a high resistance compared to the DUT (R_{DUT}), the vast majority of the current (I_c) flows through the DUT. Therefore, only R_{DUT} is measured without contributions from R_{lead} or contact resistances.

Non-Local and Local Voltage Measurements

In a current biased measurement of a multi–terminal electrical circuit there are two kinds of voltage measurements that may be taken. A local voltage is the most familiar, where the voltage measurement is taken within the path of the current and can be used to determine local resistance. A non–local voltage is taken outside the current path and can be used to measure effects that arise as a consequence of the current. A schematic of the I and V probe configuration for each measurement is depicted in Figure 3.14. As detailed in Chapter 2, a non-local measurement is used to study pure diffusive spin currents. The spin related voltages are small, so most studies use an AC source with a lock–in amplifier to extract it from the background noise. Although effective,

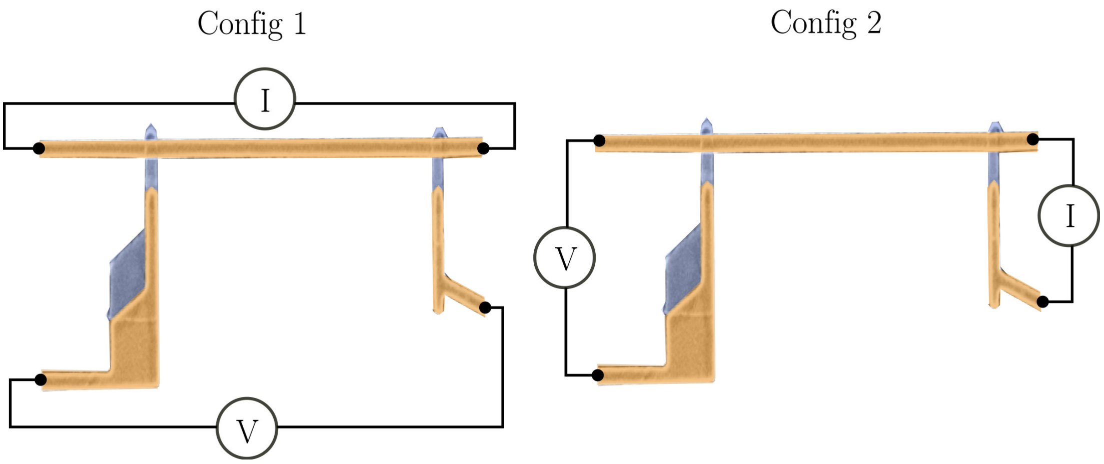

Figure 3.14: Config 1 depicts the probe configuration for a local measurement used to measure the resistance of the transport channel. Config 2 depicts the probe configuration for a non-local measurement used to study spin transport. Here, the right-hand electrode is the injector and the left-hand electrode is the detector.

information from the direction and magnitude of the applied current is inevitably lost. An alternative is to use a DC method which is capable of retaining the effects of current polarity, is faster, and has fewer error sources than the lock-in technique [50, 105]. Throughout this work a DC method was employed for both local and non-local measurements.

Measurement Procedure

After mounting the sample on the measurement head, with the FM electrodes parallel to the direction of the magnetic field produced within the cryostat, the head was connected to the measurement stick and loaded into the VTI. Electrical connections (choice of I, V) were made using the breakout box described in the previous section. To this, a 6221 DC current source and 2182 Keighley Nanovoltmeter were connected. The measurement system was entirely controlled by PC LabView software written by Dr. Gavin Burnell. For each device a local four-point measurement (config 1 in Figure 3.14) was performed whilst cooling from 275 K to measure the local resistance of the Cu. Upon reaching low temperatures, the V and I connections were changed to config 2 (Figure 3.14) to begin non–local measurements. In steps up to 275 K the temperature was stabilised with stablility criteria of $dT/dt < \pm 20$ mK/min and a temperature error of 20 mK. An in-plane field of 300 mT was applied to align the magnetisation of the FM electrodes in the P state. At each field value, the non–local voltage (V_{NL}) was measured whilst sweeping the injection current between ±500 μA to obtain a full non-local IV (NLIV). A NLIV was measured at each field value as it decreased to –300 mT and back to 300 mT in steps of (5–20) mT passing through both the AP and P electrode states.

3.3.2 Other Characterisation Techniques

Scanning Electron Microscopy

A Field Emission Gun (FEG) SEM has a high resolution so was used for device inspection and measurements of the lateral geometry. The imaging electrons are produced under vacuum in the electron gun by field electron emission from a very sharp W tip (approximately 10 nm in diameter). Emitted electrons are then focused through a number of electrostatic and magnetic lenses and accelerated through a variable potential (1 –30 kV) to produce a coherent electron beam that hits the sample. Upon impact with the sample the high energy electrons dissipate their energy through various electron-sample interactions. Depending on the penetration depth the incident electrons may backscatter, produce secondary electrons, X–ray emission, heat, light and diffracted backscattered electrons. Backscattered electrons and secondary electrons are most useful for imaging purposes, where the former gives good contrast between materials and the latter detailed surface topology and morphology. Within the imaging chamber there are specialised detectors for each emission type. For our purposes, measurements of sample geometry were taken using the backscattered electron detector with an acceleration voltage of 5 kV and working distance of approximately 3.5 mm. Example measurements included electrode separation and component widths. A LEO Gemini 1525 FEG–SEM was used in this work.

Atomic Force Microscopy

A key parameter in analysis is the thickness of the resulting nanowires. Two methods were used to verify this, AFM and X-ray reflectivity (XRR). The principle of AFM is based on the interaction between a probe and the surface to be imaged. The probe consists of a long Si cantilever with a sharp tip (10 to 5 nm) at the bottom. To understand the interaction between sample and probe the spring constant, k, of the cantilever can be determined as $k = Ewt^3/4L^3$. Where w = cantilever width; t =

cantilever thickness; L = cantilever length and E = Young's modulus of the cantilever material. This spring constant determines how the cantilever will respond to contact with a surface. Deflections of the cantilever is monitored by a laser spot which reflects off the cantilever and onto a position photosensitive detector (PSPD). There are two working modes for an AFM: tapping mode, where the oscillation amplitude is used to generate a topographical image; or contact mode, where the height is constant and the tip deflection generates an image. In tapping mode, once the tip and sample are brought into contact the tip begins to raster over the selected scan area. The aim is to maintain a constant oscillation amplitude and is controlled by adjusting the z position of the cantilever based on feedback from the PSPD. These changes in z are used to produce a topographical image of the surface. A Digital Instruments Dimension 3100 was used in this work and operated in tapping mode to reduce damage to the devices.

X-Ray Reflectivity

During maintenance and sample growth, thin films were grown alongside patterned devices to corroborate the thicknesses measured using AFM and also to calibrate growth rates. The thickness of these films were measured using XRR. In this process, X-rays are produced within a vacuum tube by passing a current through a resistive filament to emit electrons thermionically. A large potential difference accelerates the electrons toward a target, in this instance Cu, where they either rapidly decelerate and emit a continuous spectrum of radiation, with the wavelength depending on the initial electron kinetic energy (called Bremsstrahlung); others ionise the core electrons of the cathode. Higher energy electrons transition to fill the vacancies and emit an X–ray photon with a well defined energy determined by the transition. These are called characteristic X–rays, which form sharp peaks in the X–ray tube emission spectra. A series of slits and filters are then used to produce a monochromatic X–ray beam with a well defined wavelength. The probing X-ray beam, sample, and detector are first aligned to satisfy the specular condition. This condition is satisfied when the angle between the incident X-ray beam and sample (θ_{i}) is twice the angle between the incident X-ray beam and the detector, called the detector angle ($2\theta_{\mathrm{i}}$). For θ_{i} less than a critical angle (θ_{c}) all X-rays will be reflected from the sample surface in Total External Reflection (TER). For θ_{i} just above θ_{c}, X–rays enter the sample and at each interface, with different refractive indexes (n), are either reflected or transmitted. Measuring the intensity of X-rays as a function of θ_i results in a complex pattern of interference, called Kiessig fringes. For a single layer film the periodicity of the Kiessig fringes is determined by layer thickness, the depth determined by the electron density in the layer, and the decay of the curve gives information on the surface roughness. Fitting with Bede software allows these parameters to be extracted by fitting the resulting curves.

CHAPTER 4

Spin Transport in Lateral Spin Valves

4.1 Introduction

Although the study of spin transport in metals is not a particularly new field, substantial gaps in our knowledge remain. A primary goal of the lateral spin valve (LSV) community is to maximise the spin signal (ΔR_S), which necessitates both enhancing the spin diffusion length of the non-magnetic transport channel (λ_{NM}) and the efficiency of spin current injection from the ferromagnets (FM). In the most commonly studied materials, Cu and Ag, λ_{NM} is known to depend on the intrinsic spin–orbit coupling of the material and other extrinsic factors, such as interfaces, surfaces, grain boundaries and impurities [59, 106, 107]. In nanostructures, these extrinsic factors tend to dominate and are inherently difficult to control. Among the various methods to improve the spin injection efficiency, an attractive approach is to use FMs with high intrinsic spin polarisations (α_{FM}). From the starting point of a high α_{FM}, further adjustments can be made to increase the spin injection efficiency, such as the use of tunnel barriers [108], dual injectors [109, 110] and increasing the spin resistance of the FM injector (R_{FM}) [51]. Perhaps the most widely adopted FM is Py, but the modest spin polarisation ($\sim 40\%$) limits the efficiency of spin injection that can be achieved [41, 71, 78]. CoFe alloys were suggested to be robust alternatives; they possess a high intrinsic spin polarisation, soft magnetic properties, are simple to deposit, and the magnetic and transport properties can be tuned by varying the ratio of Co to Fe [42, 111]. The use of a $Co_{60}Fe_{40}$ alloy in Cu based LSVs was shown to increase ΔR_S four-fold compared to Py at room temperature and attributed to a higher spin polarisation of 0.5 ± 0.2 [43]. Despite this, the optimisation of the use of CoFe alloys in LSVs has not been explored further.

When designing an LSV one of the most important parameters to consider is the thickness of the FMs (t_{FM}). Reducing the thickness can increase the resistivity through surface or grain boundary scattering [112–116], which can increase R_{FM} and improve the injected spin polarisation. On the other hand, these additional sources of momentum relaxation can lead to a reduction of the intrinsic spin polarisation with thickness [117–119]. The situation is complicated further in devices fabricated with a shadow deposition technique; widely regarded to produce high quality transparent interfaces [68], but susceptible to magnetic impurity (MI) contamination [30, 81, 97]. In a 2010 study of shadow deposited Co/Cu LSVs an increase in t_{Co} was shown to decrease the spin diffusion length of the Cu (λ_{Cu}) at 5 and 295 K [46]. In this study, it was suggested that ferromagnetic material built up on the resist walls during the angled evaporation and was subsequently implanted into the transport channel during the non-magnetic metal deposition. Increasing the thickness, increased the build-up of material on the resist and in turn the degree of MI contamination. Since then, MIs have been shown to have quite an extreme effect on spin transport. The study of MI effects was engendered by the observation of a low temperature reduction in ΔR_S in Cu and Ag based devices [78, 120, 121]. This was in contrast to the predictions of the Elliott-Yafet (EY) theory, widely accepted to describe spin relaxation in these light metals, that ΔR_S should saturate at low temperatures. L O' Brien et al. [30] identified a link between the ability for a particular FM impurity to retain its magnetism in the NM metal and the appearance of a peak in ΔR_S. Given the approximate correspondence between the Kondo temperature (T_K) of the pairing and the position of the peak (T_{max}) in ΔR_S, it was proposed that the anomalous behaviour of ΔR_S was a consequence of temperature dependent Kondo spin scattering from dilute MIs, denoted the 'spin Kondo effect'. How the spin Kondo effect manifests itself depends on the location of the impurities. MIs in the bulk of the NM affect λ_{NM} and those interdiffused at the FM/NM interfaces affect α_{FM}; the peak in ΔR_S is a combination of both with the dominant contributor determined by the fabrication method.

Annealing shadow deposited Co/Cu and Py/Cu LSVs was shown to promote interdiffusion from the FM electrodes, enhance the spin Kondo effects in α_{FM}, and at sufficiently high annealing temperatures lead to the emergence of Kondo effects in λ_{Cu} and ρ_{Cu} [97, 121]. The use of a low purity Cu source (dominant impurity being Fe) in Py/Cu LSVs showed similar enhancement of Kondo effects in λ_{Cu} and ρ_{Cu} [78]. The consequences of contamination via the resist initially suggested by H. Zou et al. [46] have not been studied since. In a follow up paper on Py/Cu LSVs (with thin Py), the same group revealed that a monotonic ΔR_S could be recovered once the devices were exposed to atmosphere for 143 days [120]. The study concluded that the MIs introduced via the resist were concentrated at the sides/surfaces of the NM channel, and post oxidation were encompassed within a ∼6 nm layer of CuO rendering them inaccessible to the conduction electrons. If MIs introduced in this way are solely introduced at the sides/surfaces we might expect that the Kondo effect would be suppressed due to the spin-orbit anisotropy of the surface [122–124]. The previous thickness dependent study did not examine the temperature dependence of the spin transport nor charge transport, which have proved indispensable in studying the sources and relative magnitudes of different spin scattering sources [78, 81]. Additionally, it is not clear how widespread this contamination issue is given the variety of resist thicknesses, protrusions and evaporation angles employed. This contamination route is also not well recognised in the literature and some LSV studies have compared the spin transport properties of the NM with different t_{FM} and assumed no impact [78]. In this chapter, the competing factors of spin injection and contamination effects are investigated whilst increasing the FM thickness from 15 to 30 nm in shadow deposited LSVs composed of the technologically relevant pairing $Co_{70}Fe_{30}$/Cu.

4.2 Devices

Two sets of LSVs were fabricated for comparison each with identically designed lateral geometries, Cu thickness and deposition rates of 0.2 Å/s for the Cu and 0.06 Å/s for the $Co_{70}Fe_{30}$ (referred to as CoFe for the remainder of this chapter). The only intentional variation between the two sets was the thickness of the CoFe electrodes (t_{CoFe}) from 15 nm to 30 nm. Each set was deposited with shadow deposition in a growth pressure of approximately $1x10^{-9}$ mbar. To maintain consistency between the CoFe/Cu interfaces of the two sets the delay between Cu and CoFe deposition was set to 15 minutes. The time (t) for a monolayer of gas to form under ultra high vacuum conditions, assuming that every incoming particle that arrives at the interface remains there, can be estimated from $t = \frac{3.2}{p} x10^{-6}$s, where p is the pressure in mbar [125]. Using the growth pressure, which is an upper limit, we obtain $t \approx 53$ minutes. Therefore, 15 minutes was assumed to be a short enough time period to avoid monolayer absorption of residual gases at the interfaces, whilst allowing the chamber to be pumped out prior to the Cu deposition. To prevent oxidation all samples were coated with 500 nm of Methyl Methacrylate (MMA) resist (no baking) and stored under high vacuum ($\approx 1x10^{-6}$ mbar) until measurement.

Slight variations in lateral geometry are inevitable from the fabrication process so scanning electron microscopy (SEM) was used to determine the precise widths of the CoFe injector (W_{CoFe_1}), detector (W_{CoFe_2}) and Cu channel (W_{Cu}) for each LSV. The average values calculated for each set were: W_{Cu}=(120±3) nm, W_{CoFe_2}=(132±2) nm, W_{CoFe_1}=(120±2) nm for the t_{CoFe} = 15 nm set; and, W_{Cu}=(125±3) nm, W_{CoFe_2}=(134±3) nm, W_{CoFe_1}=(122±2) nm for the t_{CoFe} = 30 nm set. Additionally, the edge-edge electrode separation (L) was measured for each LSV, as depicted in Figure 4.1(a).

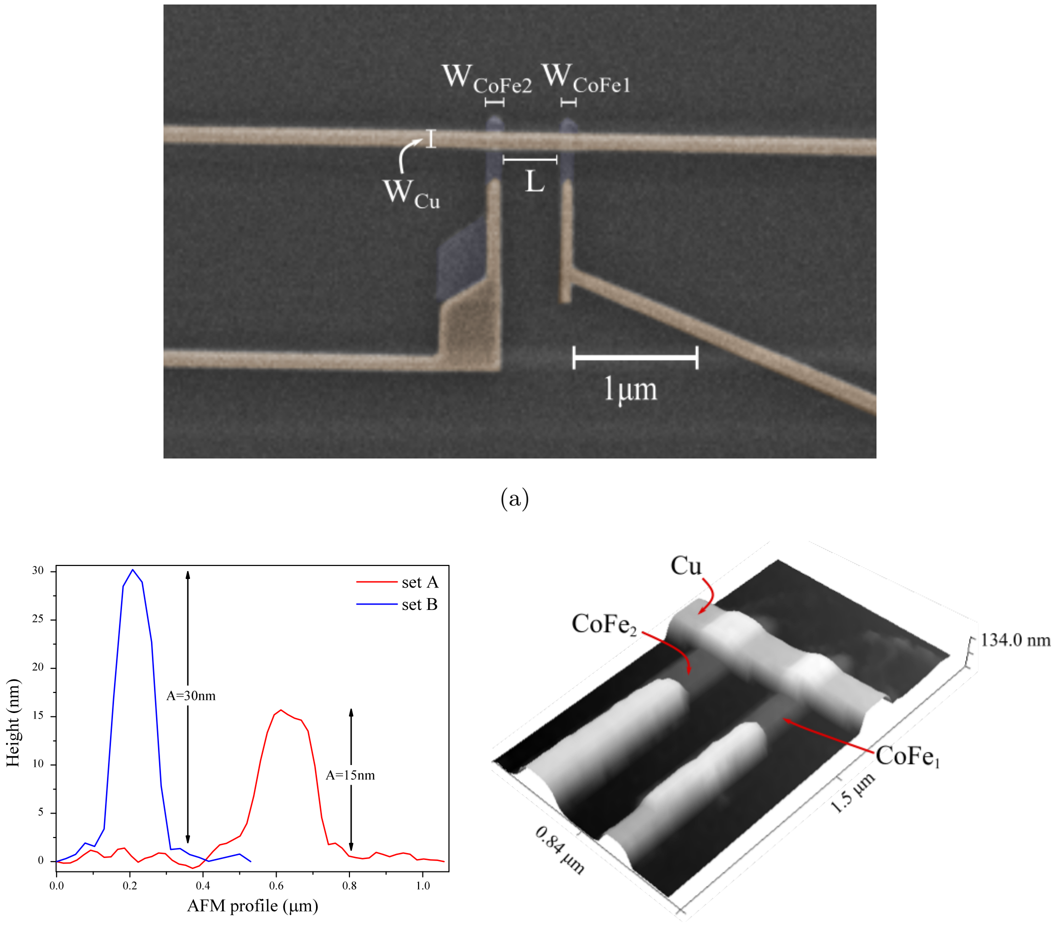

(a)

(b)

(c)

Figure 4.1: (a) SEM image of an LSV from set A with false colours to indicate the different materials Cu (orange) and CoFe (blue). The relevant device geometries measured using SEM in each LSV are also indicated. (b) AFM height profile over the CoFe injector and detector (set B in blue and set A in red). (c) 3D representation of an AFM height map over the CoFe injector (CoFe_1), detector (CoFe_2) and Cu transport channel of an LSV from set B, produced in Gwyddion software.

Element thicknesses were measured using atomic force microscopy (AFM) yielding: t_{Cu}=(112±2) nm, t_{CoFe}=(15±2) nm for the $t_{\text{CoFe}} = 15$ nm set; and, t_{Cu}=(100±1) nm, $t_{\text{CoFe}} = (30\pm3)$ nm for the $t_{\text{CoFe}} = 30$ nm set. Moreover, multiple AFM line profiles along the length of the Cu wires confirmed a roughness of less than ±2 nm for both sets. In the $t_{\text{CoFe}} = 30$ nm set, six LSVs were measured with electrode separations between 400 nm and 1.7 µm. In the t_{CoFe} = 15 nm set, seven LSVs were measured with electrode separations between 490 nm and 2.2 µm. Henceforth we denote the t_{CoFe} = 15 nm set as 'set A' and the t_{CoFe} = 30 nm set as 'set B'.

4.3 Charge Transport

The resistance (R_{Cu}) of each Cu transport channel was measured using a four-point local measurement (see Chapter 3) whilst cooling from 275 to 4 K. Following this, the resistivity (ρ_{Cu}) of each channel was calculated from $\rho_{\mathrm{Cu}} = \frac{A_{\mathrm{Cu}} R_{\mathrm{Cu}}}{L}$, where $A_{\mathrm{Cu}} = W_{\mathrm{Cu}} t_{\mathrm{Cu}}$. Ideally, ρ_{Cu} should be identical for each LSV within a set given the identical processing conditions. Despite this, there was some variation in resistivity from device to device which others have attributed to unavoidable variations in microstructure [106]. In the forthcoming spin transport analysis, an average value of λ_{Cu} for each set will be extracted which requires the assumption that all LSVs (within a set) share a common ρ_{Cu}. Given that the variation in ρ_{Cu} for either set was not too large and each shared the same temperature dependence, an average ρ_{Cu} with standard error for each set was calculated and depicted in Figure 4.2(a).

To facilitate later analysis, where the momentum relaxation times (τ_{e}) are related to the spin relaxation times (τ_{sf}) through the EY theory, the Drude model was used to calculate τ_{e} from $\frac{1}{\rho} = \frac{ne^2\tau_{\mathrm{e}}}{m}$, where m is the free electron mass and n is the conduction electron density ($n_{\mathrm{Cu}} = 8.5\mathrm{x}10^{28}$ e/m^3). Additionally, to compare the characteristic length scales for spin and charge transport, the electronic mean free path (λ_{e}) was calculated from $\lambda_{\mathrm{e}} = \tau_{\mathrm{e}} v_{\mathrm{f}}$, where v_{f} is the Fermi velocity which we take as the free electron value of $v_{\mathrm{f}} = 15.07\mathrm{x}10^5$ m/s [126]. The temperature dependence of τ_{e} and λ_{e} calculated from the average ρ_{Cu} in both sets are depicted in Figure 4.3 (a) and (b) respectively.

In the absence of significant contamination from the CoFe electrodes, ρ_{Cu} for each set should be similar. However, as shown in Figure 4.2(a), the average ρ_{Cu} in set B is roughly 1 µΩcm higher than set A across the entire temperature range. Additionally, there is a small ρ_{Cu} upturn below $T_{\mathrm{min}} \approx 8.5$ K in all six devices of set B which is not present in set A; the classic signature of Kondo scattering from dilute MIs. Similar low temperature resistivity increases can arise from weak localisation, but the resistivity of the Cu is very low compared to the typical samples ($\sim$ 100 µΩcm) where these effects are observed [127, 128]. The position and magnitude of the low temperature resistivity increase is common to all devices in set B (which are identical other than the variation in L), which suggests that the concentration of MIs is roughly constant as a function of lateral distance along the Cu channel [121].

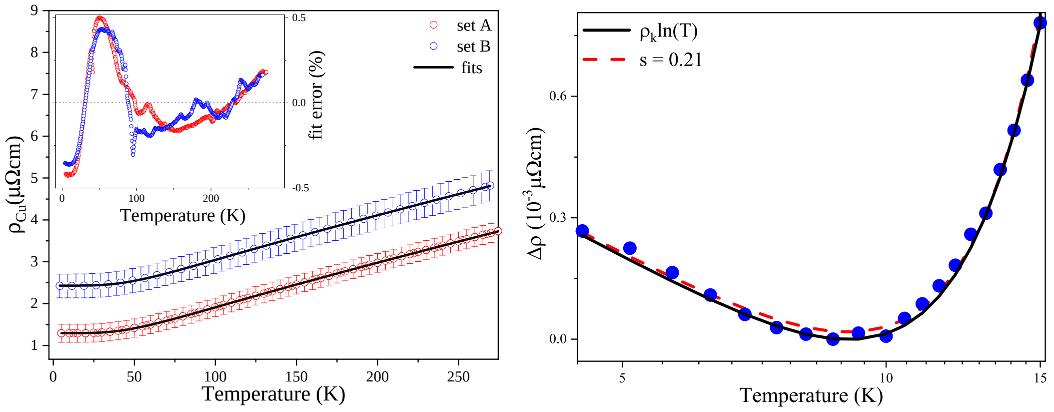

(a)

(b)

Figure 4.2: (a) Average ρ_{Cu} from each set with fits to equation 4.1. Inset graph shows the percentage fitting error calculated as $\frac{\rho_m - \rho_{BG}}{\rho_m}$x100% at each temperature, where ρ_m is the measured data and ρ_{fit} is the fitted value. The fitting error is less than ±0.5% at all temperatures in both sets, so the agreement between the data and fit is very good. (b) The average low temperature resistivity increase ($\Delta\rho = \rho(T) - \rho(T_{min})$) in set B. Two fits are shown: the first (black line) is the low temperature portion of the fit to equation 4.1; and, the second (red dashed line) is a fit to the phenomenological model for the Kondo effect (equation 4.2).

Assuming that Matthiessen's rule is valid the total resistivity can be written as the sum of the phonon resistivity (ρ_p), residual resistivity (ρ_0) and magnetic resistivity (ρ_m). The former can be represented by the Bloch–Grüneisen (BG) function and the magnetic contribution to the resistivity can be approximated as $\rho_m = \rho_k$ ln(T), where ρ_k is the Kondo resistivity. The total resistivity is therefore:

$$\rho(T) = \rho_0 + K_{el-ph}\left(\frac{T}{\Theta_D}\right)^n \int_0^{\frac{\Theta_D}{T}} \frac{x^n}{(e^x - 1)(1 - e^{-x})} dx + \rho_k \ln(T) \tag{4.1}$$

where, K_{el-ph} is a constant related to the electron-phonon coupling, Θ_D is the Debye temperature and n is an exponent, which in this case is equal to 5 [129, 130]. Equa-

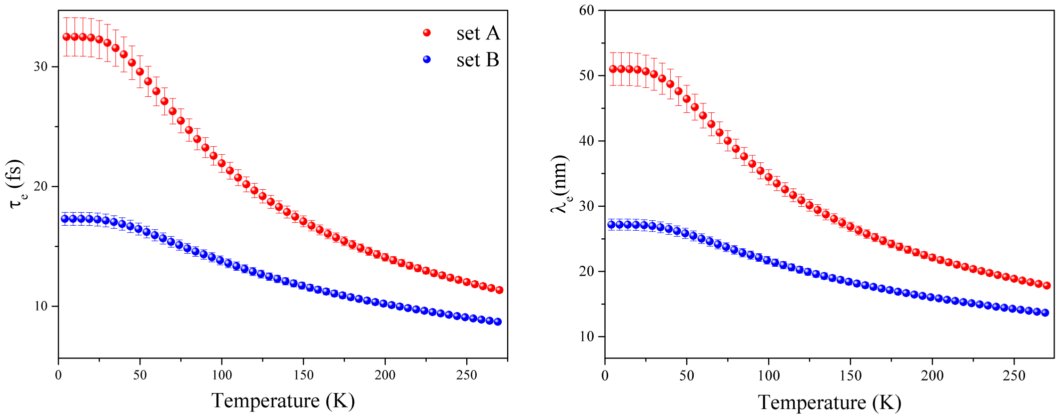

(a)

(b)

Figure 4.3: Calculated charge transport parameters $\tau_{\rm e}$ (a) and $\lambda_{\rm e}$ (b) for each set; both are larger in set A due to the lower Cu resistivity.

tion 4.1 was fitted to the average resistivity of both sets with $\Theta_{\rm D}$, $K_{\rm el-ph}$, ρ_0 and $\rho_{\rm k}$ left as free fitting parameters; the results are depicted in Figure 4.2(a). The extracted values of $\Theta_{\rm D}$ are extremely close to one another: $\Theta_{\rm D}$= (287.1±0.6) K and $\Theta_{\rm D}$=(286.0±0.3) K for sets B and A respectively. Both are roughly 17% lower than bulk Cu indicating the presence of ‘phonon softening’ , which is frequently observed in systems with reduced dimensions [130, 131]. Phonon softening is a reduction of the overall average frequency of the phonon distribution as a result of either an increased surface to volume ratio (as the dangling bonds at the surfaces alter the phonon modes), or scattering from disorder [132, 133]. Softening in this case is likely a result of the increased surface to volume ratio, as $\Theta_{\rm D}$ are close whereas ρ_0 are dissimilar. The electron–phonon coupling constants were found to be $K_{\rm el-ph}$=(10.791±0.002) µΩcm and $K_{\rm el-ph}$=(10.756±0.001) µΩcm for sets B and A respectively. Both values are close, albeit a little larger than values found elsewhere for mesoscopic Cu wires which tend to be between 6 to 9 µΩcm [130] [134]. Larger $K_{\rm el-ph}$ are often accompanied by phonon softening effects and have been attributed to surface roughness and internal disorder [135–137]. The electron-phonon scattering characteristics are comparable in each set so the resistivity difference stems from the temperature independent residual resistivity arising from disorder, which is $\rho_0 = (2.4 \pm 0.2)$ µΩcm in set B and $\rho_0 = (1.3 \pm 0.1)$ µΩcm in set A.

Resistivity Minimum

As depicted in Figure 4.2(b), the low temperature resistivity increase in set B follows the classic logarithmic temperature dependence associated with the Kondo effect; although the measurements are not to a sufficiently low temperature to observe the transition to the $\propto T^2$ dependence with the onset of electron-electron interactions and screening of the impurity spin [138]. The Cu in each set was evaporated from the same 99.9999% purity source, with the same deposition rate and in equivalent growth pressures. Therefore, these additional MIs did not originate in the source nor enter from residual vapours in the deposition chamber. Additionally, neither set was annealed (which would encourage interdiffusion from the electrodes into the channel) apart from 10 minutes in 60^{o}C acetone during post deposition processing. This leaves the contamination route suggested by H. Zou et al. [46, 120], where MIs enter via the resist due to the angled evaporation of the FM. To illustrate this more clearly, Figure 4.4 shows a schematic of the angled deposition procedure. CoFe was deposited first at 45^{o} to the substrate, thereby ensuring deposition into the patterned regions to form the electrodes but also onto the side walls of the resist that surrounded the Cu channel (indicated by the red box). During the subsequent Cu deposition, normal to the substrate, the energetic flux had the potential to dislodge small amounts of CoFe deposit from the resist walls and implant it into the Cu channel. Increasing the amount of CoFe deposited, increased the build–up on the resist walls and in turn the degree of MI contamination of the Cu channel. The appearance of a Kondo upturn in the resistivity of set B is in agreement with the suggestions of [46], that MI contamination is exacerbated by an increase in t_{CoFe}. However, our observations contradict the conclusions of [120] that the MIs are confined to a small ($\sim$ 6 nm) region at the channel surfaces. As shown in Figure 4.3(b), even at 4 K the electronic mean free path is less than the dimensions of the channel; thus, bulk scattering is the dominant source of momentum relaxation. In this instance, therefore, MIs have penetrated further into the Cu channels than suggested previously [120].

Both Fe and Co diluted in bulk Cu retain their magnetism and may Kondo scatter. They do, however, have very different Kondo temperatures ($T_K^{\mathrm{Fe}} \approx 20 - 30$ K [89, 90, 92, 93] and $T_K^{\mathrm{Co}} \approx 500$ K (in bulk) [90, 139, 139, 140]), impurity spins ($S_{\mathrm{Co}} = 1$ [97, 141] and $S_{\mathrm{Fe}} = \frac{1}{2}$ [78, 81, 88, 142]) and equilibrium solubility in Cu (negligible for Co [143] compared to 2600ppm for Fe [144]). Kondo scattering is known to be sup-

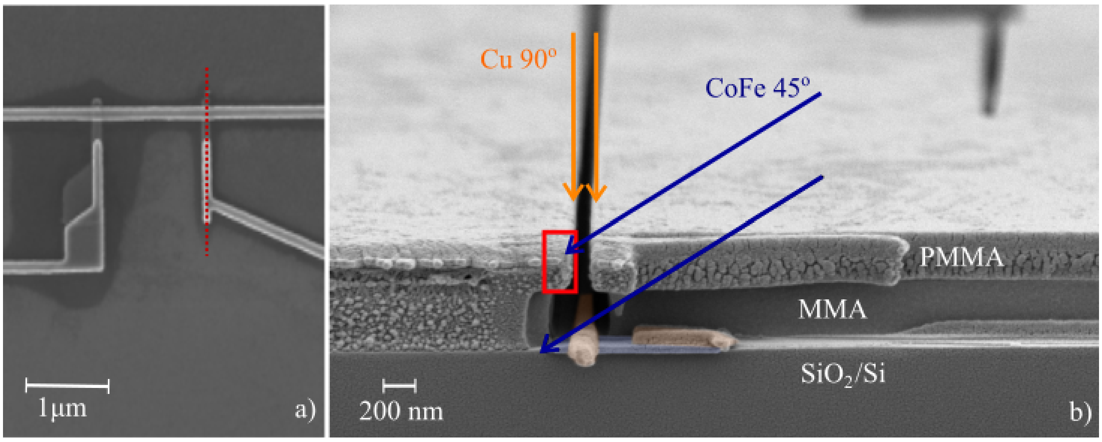

Figure 4.4: (a) SEM image of an LSV with red hatched line indicating the position of the cross section. (b) An angled SEM image of an LSV post shadow deposition and pre lift off. The device was sputtered with Au to prevent charging during imaging then cut using a focused ion beam along the injector. This work was performed by Dr Georgios Stefanou. The deposition angles of Cu and CoFe are shown, along with the red box which indicates the resist region where we believe CoFe deposits build-up during deposition.

pressed in thin films (generally with thicknesses below ∼150 nm) and attributed to spin-orbit anisotropy from the surfaces [145–147]. The suppression decreases roughly with the distance of the impurity from the surface and depends on the impurity spin; Kondo scattering can be quenched entirely for integer spins or partially for half-integer spins [122–124, 148]. The former situation applies to Co and was observed recently in heavily annealed Co/Cu LSVs. No charge Kondo effect was observed once t_{Cu} <200 nm despite Co being distributed throughout the Cu channel [81, 97]. Given the ∼100 nm channel dimensions in this case we suspect that this charge Kondo effect arises from Fe contaminants within the bulk of the Cu channels in set B. A phenomenological model [149, 150] can be fitted to estimate T_K as,

$$\rho(T) = \rho_0 + AT^5 + \rho_k \left(\frac{T_K'^2}{T^2 + T_K'^2} \right)^s \tag{4.2}$$

$$T_K' = \frac{T_K}{\sqrt{2^{\frac{1}{s}} - 1}} \tag{4.3}$$

where, AT^5 approximates the phonon contribution and the scaling parameter s is equal to 0.21 for a $S=\frac{1}{2}$ impurity [138, 149]. The fit is depicted in Figure 4.2(b) and yields $\rho_K = (2.1 \pm 0.1)$ nΩcm and $T_K = (17 \pm 4)$ K, the latter value being at the lower end of reported values for dilute Fe in Cu [89, 145, 151]. From the position of the minimum (T_{min}) a rough estimate of the concentration of Fe impurities ($\mathbf{c}_{Fe}$) can be obtained from Knook's empirical expression $T_{min} = 115\mathbf{c}_{Fe}^{\frac{1}{5.3}}$ [87, 152], which yields $\mathbf{c}_{Fe} \approx$ 1ppm. Assuming that the impurity resistivity contribution varies linearly with concentration ($\Delta\rho \propto \mathbf{c}$), and using the quoted $\Delta\rho_0 \approx$ 14.5 µΩcm per % Fe in Cu [142] leads to $\Delta\rho_0 \approx 1.5\text{x}10^{-3}$ µΩcm. This is far less than the 1 µΩcm higher residual resistivity in set B. This suggests a much higher impurity content in this set than can be inferred from the resistivity minimum alone. In particular, any Co impurities whose spins are hindered by the spin-orbit anisotropy [153] will still contribute to ρ_0. If so, these impurities may be visible in spin transport measurements. A growing body of work centred on the role of MIs in LSVs tend to show that spin transport is much more sensitive than charge transport to ppm levels of MIs [30, 81, 97, 121]. As a consequence, even in the absence of a measurable Kondo effect in the resistivity there can be clear signatures of Kondo scattering in spin transport measurements. Other possible sources of the higher resistivity in set B include an increase in geometrical disorder at the CoFe/Cu interfaces given the higher CoFe thickness in this set, or differences in average grain sizes [112]. Both should manifest as a temperature independent contribution to spin scattering [56] so are easily distinguished from spin scattering by MIs, which have a strong temperature dependence [30, 78, 81, 97].

4.4 Spin Transport

To study spin transport, voltage (V) and current (I) connections were made to each LSV in the non–local configuration depicted in Figure 4.5. The goal here is to obtain the spin signal (ΔR_S), which reflects the amount of the spin accumulation reaching the detecting CoFe electrode. The magnitude of ΔR_S is determined by the initial spin accumulation at the injecting interface and the amount of spin scattering in the Cu channel. In each set of LSVs, measurements of ΔR_S as a function of electrode separation allows the spin diffusion length of the Cu (λ_{Cu}) and the spin polarisation of the CoFe (α_{CoFe}) to be extracted.

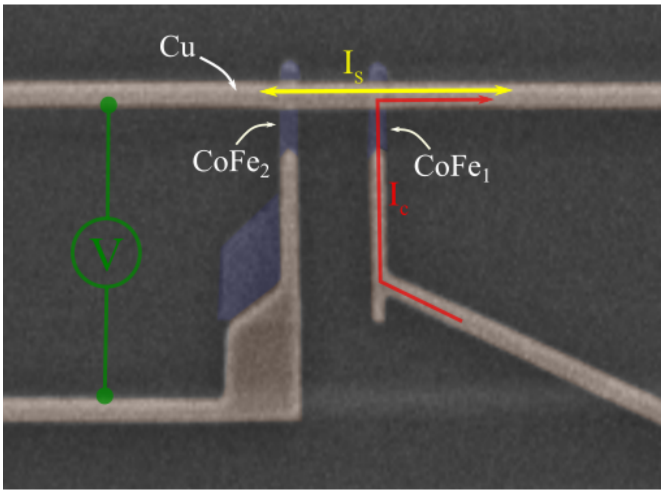

Figure 4.5: LSV with connections in the non–local configuration used to study spin transport. For all devices the narrow CoFe electrode ($CoFe_1$) was used as the injector and $CoFe_2$ as the detector. The passage of I_c through the injecting interface (right hand side), generates a local spin accumulation and drives a diffusive spin current (I_s) in both directions along the Cu channel. The spin current diffusing to the left is free from the charge current and thus a pure diffusive spin current. Any remaining spin accumulation at the detecting interface produces a voltage between the Cu and $CoFe_2$.

Extracting ΔR_s

At each measurement temperature, a small in–plane field of 300 mT was applied to align the magnetisation of the CoFe injector and detector in the parallel (P) state.

Following this, the field was stepped to -300 mT and back to 300 mT measuring the non–local voltage (V_{NL}) at each field value. During this field sweep, the CoFe electrodes pass through both orientations of the P and the anti–parallel states (AP). The term of interest here is the non-local voltage induced by a spin accumulation at the detecting interface ($V_s = \frac{\nabla\mu}{e}$), which is linear to the applied current and reversible [50]. However, due to thermoelectric effects, each V_{NL} contains additional contributions and takes the form of a second order polynomial, $V_{NL} = R_1I + R_2I^2 + c$. A typical example of the current dependence of V_{NL} is shown in Figure 4.6(a).

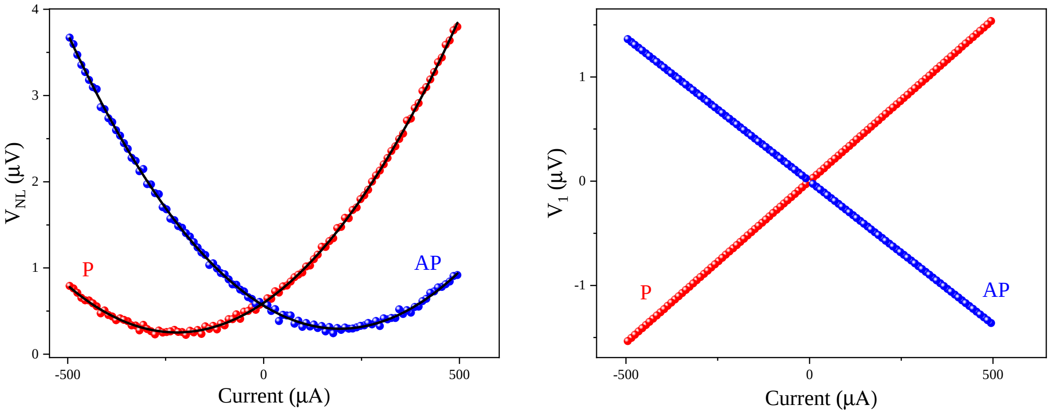

(a)

(b)

Figure 4.6: (a) Raw V_{NL} in P and AP electrode states fitted with a 2nd order polynomial (black lines). (b) The linear voltage response (V_1) extracted from fitting a 2nd order polynomial to V_{NL} in the P and AP electrode states. The gradient of V_1 is the non-local linear resistance (R_1), which is positive and negative in the P and AP states respectively.

The quadratic term (R_2I^2) arises from Joule heating in the path of the injection current (discussed in more detail in Chapter 5) and c is an offset from the measurement equipment. The spin voltage is encompassed within the linear voltage component (V_1=R_1I) of V_{NL}. Figure 4.6(b) depicts V_1 extracted from fitting a 2nd order polynomial to V_{NL} in the P and AP electrode states. V_1 shows a strong dependence on the magnetisation orientation and is bipolar in the direction of applied current. This behaviour is characteristic of the spin accumulation induced voltage, as observed in previous studies [3, 50]. The slope of V_1 yields the non-local linear resistance, R_1. Although difficult to distinguish from Figure 4.6(b), R_1 contains an additional contribution from the reversible Peltier heating/cooling at the injecting interface. This Peltier induced voltage is independent of the magnetisation orientation of the CoFe electrodes, so the two contributions can be separated by plotting the applied field dependence of R_1. Figure 4.7 shows the typical magnetic field dependence of R_1; in this instance measured at 60 K in a L=1300 nm device from set A.

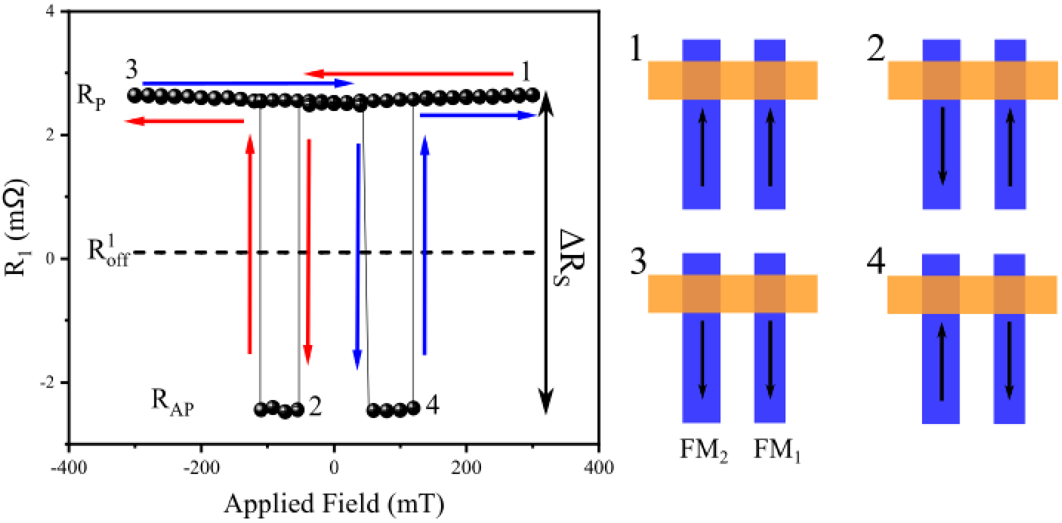

Figure 4.7: Left figure shows the linear non-local resistance (R_1) as a function of applied in–plane magnetic field at 60 K. The non-local spin resistance switches from positive (R_P) to negative (R_{AP}) as the electrodes transition from the P to AP state. In contrast, the Peltier induced non-local resistance has no dependence on the magnetic alignment of the CoFe electrodes and remains constant with applied field (R^1_{off}, dashed line). The arrows show the direction of the field sweep with points 1-4 depicting the different magnetisation alignments of the electrodes, which are illustrated in the schematic to the right.

At high fields, both CoFe electrodes are aligned parallel (1 and 3) and the non-local resistance is positive (R_P). At roughly (±)70 mT, the magnetisation of the detecting electrode reverses, the electrodes are aligned anti-parallel (2 and 4) and the non-local linear resistance is negative (R_{AP}). This switching behaviour is a result of the non-local spin resistance across the Cu/$CoFe_2$ interface only. In contrast, the Peltier contribution has no field dependence and is manifested as a constant offset (R^1_{off}, black dashed line) between the R_P and R_{AP} states. The spin signal can be extracted as the difference between the P and AP resistance states ΔR_S=R_P-R_{AP}, and contains no contribution from the Peltier offset.

The Spin Signal, ΔR_S

Following the procedure outlined above, the temperature dependence of ΔR_S was extracted for multiple LSVs in each set. Figure 4.8(b) shows the spatial decay of ΔR_S at 5 K for both sets. At all electrode separations, ΔR_S is between 2 to 4 times smaller in set B. This indicates either a lower initial spin accumulation at the injecting interface (related to α_{CoFe}) or an increase in spin scattering in the Cu channel (related to λ_{Cu}) in set B.

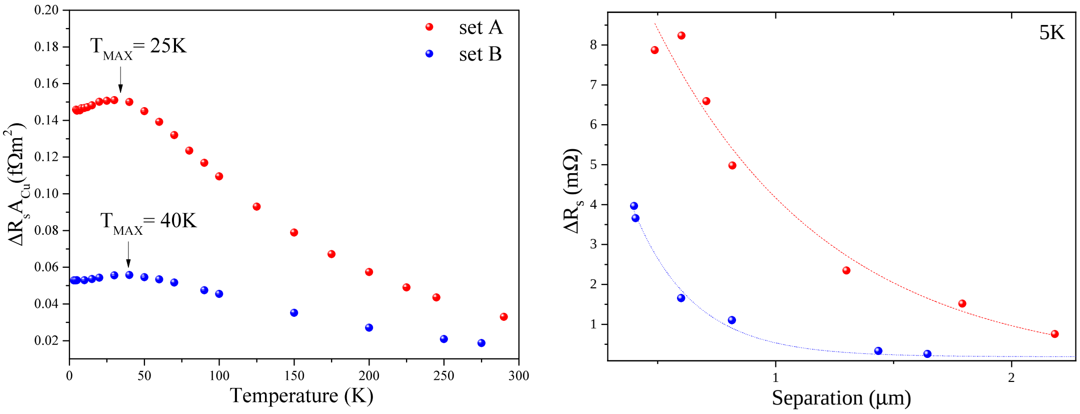

(a)

(b)

Figure 4.8: (a) To account for slight geometrical variations in the Cu channels between each set of devices, the spin signal area product ($\Delta R_S A_{Cu}$) is compared for two L≈600 nm devices from set A and B. (b) The spatial decay of ΔR_S for both sets at 5 K with fits (dashed lines) to equation 2.15.

Additionally, the temperature dependence of ΔR_S (depicted in Figure 4.8(a)) demonstrates that there are notable differences, other than the reduced magnitude, between set A and B. In set B, the overall temperature dependence is weaker and the low temperature reduction (or 'downturn') is larger and shifted to a higher temperature. The position of the maximum is T_{max} = 40 K in set B and T_{max} = 25 K in set A; both of which are common to all LSVs regardless of electrode separation. As noted in the introduction, this downturn is a result of temperature dependent spin scattering and has been linked to Kondo scattering from MIs [3, 30, 78, 97, 98, 121] and surface scattering [120, 155, 156]. MIs in the bulk of the NM channel and surface scattering lead to a downturn in λ_{NM}, whereas MIs at the FM/NM interfaces manifest as a low temperature reduction in α_{FM}.

To unravel the contributions from the interfaces and the bulk, the spatial decay of $\Delta\mathrm{R}_{\mathrm{S}}$ was fitted to a 1D spin diffusion equation to extract λ_{Cu} and α_{CoFe} for each set. ρ_{Cu} was taken as the average value for each set (shown in Figure 4.2(a)), and the geometry and thicknesses of the device components were taken to be the values stated earlier in this chapter. As ρ_{CoFe} could not be measured in situ, two thin films of CoFe with thicknesses of 30 and 15 nm were deposited in equivalent conditions to the LSVs and measured using a van der Pauw technique; the resistivities are depicted in Figure 4.9. Three undetermined parameters remain λ_{Cu}, α_{CoFe} and λ_{CoFe}; one of which must be constrained to achieve a meaningful fit. The conventional approach is to estimate λ_{FM} from the measured resistivity using the empirical relationship $\lambda_{\mathrm{FM}}(\mathrm{T}) = \frac{\lambda_{\mathrm{FM}}(4.2\mathrm{K})\rho_{\mathrm{FM}}(4.2\mathrm{K})}{\rho_{\mathrm{FM}}(\mathrm{T})}$, where $\lambda_{\mathrm{FM}}(4.2\mathrm{K})\rho_{\mathrm{FM}}(4.2\mathrm{K})$ is taken from the literature [55]. For our particular alloy composition one measurement of $\lambda_{\mathrm{CoFe}}(4.2\mathrm{K})$ exists, which found $\lambda_{\mathrm{CoFe}}= (10.9\pm0.5)$ nm for a 200 nm thick thin film with $\rho_{\mathrm{CoFe}}=(6.1\pm0.4)$ µΩcm [154]. From this we obtain $\lambda_{\mathrm{CoFe}}(4.2\mathrm{K})\rho_{\mathrm{CoFe}}(4.2\mathrm{K})=(0.67\pm0.05)$ fΩm^2, which when divided by ρ_{CoFe} yields the estimate of λ_{CoFe} used in the fitting procedure. At each measurement temperature, $\Delta\mathrm{R}_{\mathrm{S}}(\mathrm{L})$ was fitted to equation 2.15 extracting a value for λ_{Cu} and α_{CoFe} each time.

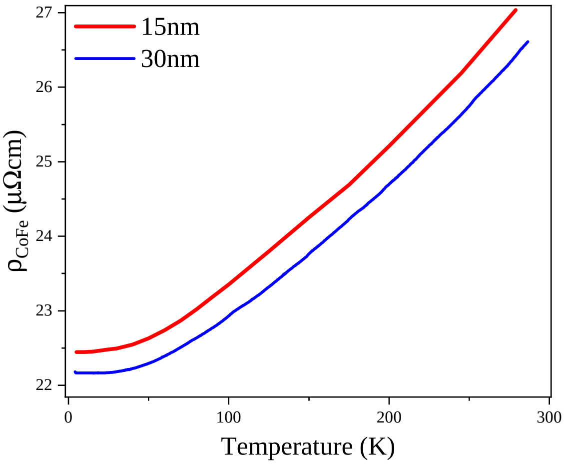

Figure 4.9: Resistivity of 15 and 30 nm thick CoFe thin films measured using a van der Pauw technique. These measurements are used to calculate an estimate of λ_{CoFe} for each set.

4.4.1 Spin Diffusion

Figure 4.10(a) shows λ_{Cu} extracted from the fits to $\Delta R_S(L)$ for both sets. In set A, λ_{Cu} is comparable to Py/Cu devices fabricated from the same Cu source [78] reaching a maximum of λ_{Cu}=(869±3) nm at 25 K; which is toward the higher end of published values. In set B, λ_{Cu} is significantly lower reaching a maximum of only (283±2) nm at T_{max}=50 K; still well within the literature range [68], but low given the high purity Cu source used.

The EY mechanism is recognised to be the prevailing theory to describe spin scattering in light metals like Cu [14, 56, 76] and predicts that the spin diffusion length should follow the temperature dependence of the electronic mean free path ($\lambda_s \propto \lambda_e$). The most obvious deviation is the low temperature peak in each set, which is widely observed throughout the literature and has been linked to Kondo scattering from bulk MIs and spin-orbit scattering from the channel surface. Earlier, charge transport measurements revealed the presence of dilute Fe contaminants in the bulk of the Cu channels in set B. Thus far, without exception, in devices where a charge Kondo effect from Fe impurities is detectable a peak in λ_{Cu} at some temperature T_{max} that roughly correlates to $T_K = 30$ K is observed [12, 28, 30, 56, 78, 98, 120, 155, 156]. We can surmise

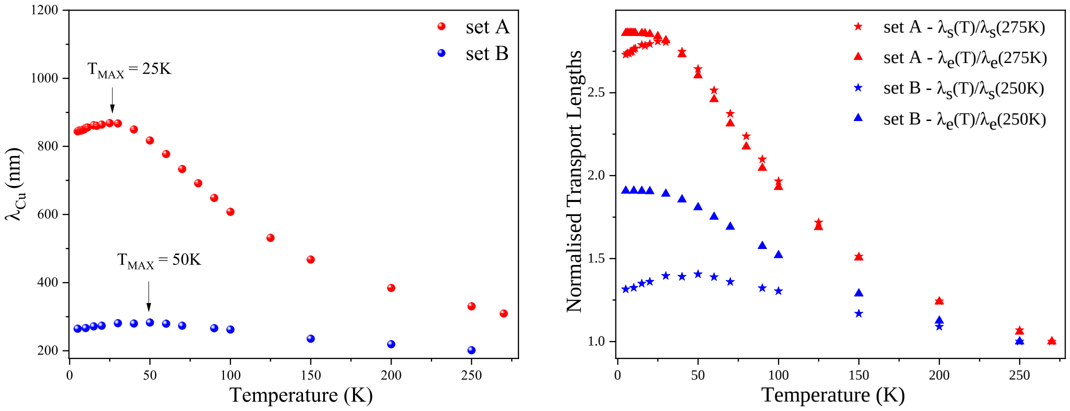

(a) (b)

Figure 4.10: (a) The spin diffusion length of Cu extracted from fitting $\Delta R_S(L)$ for LSVs in set B (blue) and set A (red). (b) The spin diffusion length (λ_s - stars) and electronic mean free path (λ_e - triangles) normalised by their value at the highest measurement temperature (275 K in set A and 250 K in set B) to illustrate the deviations from the expected EY behaviour of $\lambda_s \propto \lambda_e$. In set A (red), the two lengths scale perfectly with one another down to the 25 K maximum in the spin diffusion length. Whereas, in set B, the spin diffusion length increases much less than the electronic mean free path below 200 K.

that the anomaly in set B is, at least in part, the result of Kondo spin scattering from these bulk Fe impurities. Spin scattering from these contaminant Fe impurities will also lower λ_{Cu} overall, as we have observed. Additionally, although no charge Kondo effect was detected in set A (down to 4 K), the variation in peak position and size between the two sets can be explained in the framework of the Kondo effect arising from dilute MIs. Generally, in the absence of other effects (such as impurity type and location) increasing the MI concentration shifts T_{max} toward higher temperatures, enhances the peak and eventually at sufficiently high concentrations the conventional charge Kondo effect arises. In terms of surface scattering, neither λ_e exceeds the 100 nm Cu thickness and if the peaks were solely the result of surface scattering, set A (with a longer λ_e) would experience the onset of surface scattering at a higher temperature than set B; which is contrary to our observations.

For closer examination of the applicability of the conventional EY mechanism at all temperatures, the spin and charge transport length scales were normalised to their high temperature values as shown in Figure 4.10(b). The normalised length scales should follow the same temperature dependence if the dominant momentum scattering mechanisms are also responsible for spin scattering. In set A, both increase at the same rate upon cooling from 275 K demonstrating that electron-phonon scattering which limits λ_e at high temperatures also determines λ_s; in perfect agreement with the conventional EY theory. The only deviation occurs with the onset of the low temperature peak at 25 K, as highlighted in the previous paragraph. Conversely, in set B, the length scales follow entirely different temperature dependences for $T < 200$ K with λ_s increasing much more slowly than λ_e. This suggests the presence of a temperature dependent spin scattering mechanism, that only weakly affects the electronic mean free path and dominates over the phonon spin scattering contribution at high temperatures.

Spin Lifetime in Cu

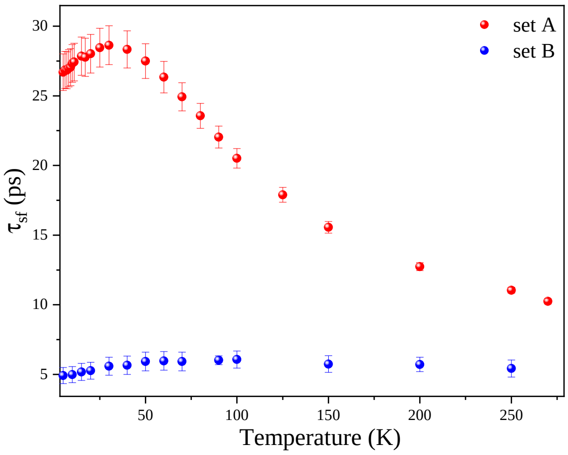

Figure 4.11: The spin relaxation time calculated from the spin diffusion length of the Cu in each set. With thin CoFe electrodes (set A), the spin relaxation time is long and the temperature dependence strongly resembles the momentum relaxation time, as expected from the EY mechanism. With thick CoFe electrodes (set B), the spin relaxation time is a factor of five smaller and has a notably weak temperature dependence. This indicates that the dominant spin relaxation mechanisms are very different in each set.

To attempt to discern the sources of spin relaxation in each set and quantify their contributions, the spin relaxation time (τ_{sf}) was calculated from $\tau_{sf} = \frac{\lambda_{Cu}^2}{D}$, where

$D = \frac{1}{3}\tau_e v_f^2$ is the diffusion coefficient. As shown in Figure 4.11, the spin relaxation time in set A is comparable to other clean Cu in the literature [78], whereas in set B it is a factor of five smaller. Moreover, the disparate τ_{sf} temperature dependences indicate that the dominant spin relaxation mechanisms are very different in each set. As detailed in Chapter 2, the EY mechanism links the momentum and spin relaxation times as $\frac{1}{\tau_{sf}} = \frac{\alpha}{\tau_e}$, where α is the probability of a spin-flip per momentum scattering event. For multiple independent scattering sources, Matthiessen's rule can be applied to obtain an expression for the total spin relaxation rate in terms of the individual spin scattering contributions each with a different spin-flip probability. The total spin scattering rate for phonons, defects and Kondo scattering can be written as:

$$\frac{1}{\tau_{sf}} = \frac{\alpha_{def}}{\tau_{e,def}} + \frac{\alpha_{ph}}{\tau_{e,ph}} + \frac{\alpha_k}{\tau_{e,k}} \tag{4.4}$$

where, $\tau_{e,def}$, $\tau_{e,ph}$ and $\tau_{e,k}$ are the momentum relaxation times for defects, phonons and Kondo respectively. Similarly, α_{def}, α_{ph} and α_k are the spin-flip probabilities for defects, phonons and Kondo respectively. The conventional approach is to extract each momentum relaxation time directly from the measured τ_e, input into equation 4.4 and obtain the spin-flip probability for each scattering mechanism. Recently, J.D.Watts et al. [81] suggested that the Kondo scattering contribution from MIs actually extends up to much higher temperatures than are visible in τ_e; up to 10 times T_K [138]. These high temperature contributions are much more pronounced in spin relaxation as although Kondo scattering events are less frequent than those with phonons, for example, the probability of a Kondo spin-flip ($\alpha_k = \frac{2}{3}$ [98]) is typically 100 times that of phonons ($\alpha_{ph} \approx 10^{-3}$ [77, 80, 85]). Consequently, for large MI concentrations or high T_K impurities, the Kondo spin scattering contribution can dominate over phonons even at room temperature. As noted in the previous section, this is exactly what we observe in set B. To account for this, $\tau_{e,k}$ can be calculated from the Goldhaber–Gordon phenomenological expression [157] (equations 4.5, 4.6), which can approximate the transition from the logarithmic dependence ($T > T_K$), to T^2 ($T \sim T_K$) to saturation ($T << T_K$).

$$\tau_{e,k}^{-1} = \tau_{k,0}^{-1}\left(\frac{T_K'^2}{T^2 + T_K'^2}\right)^s \tag{4.5}$$

$$\mathrm{T}_{\mathrm{K}}^{'} = \frac{\mathrm{T}_{\mathrm{K}}}{\sqrt{2^{\frac{1}{\mathrm{s}}} - 1}} \tag{4.6}$$

where, $\tau_{\mathrm{k},0}^{-1}$ is the saturation Kondo momentum scattering rate at $\mathrm{T} = 0$ K, which is related to the MI concentration. T_{K} is the Kondo temperature and in this context is defined as the temperature at which $\tau_{\mathrm{k},0}^{-1}$ is at half the maximum value. The scaling parameter (s) determines the slope of the scattering rate and is related to the impurity spin (S). The momentum scattering time from impurities and phonons can be obtained as the temperature independent and dependent parts respectively of τ_{e}. Based on previous work, the Kondo spin-flip probability can be fixed to $\alpha_{\mathrm{k}} = \frac{2}{3}$ [78, 81, 98, 162], which leaves α_{ph}, α_{def}, $\tau_{\mathrm{k},0}^{-1}$, T_{K} and s as unknowns.

Fitting equation 4.4 requires some knowledge of the relevant Kondo parameters (T_{K} and s) and the presence of two potential Kondo impurities in our devices, Co and Fe, complicates matters. The Kondo effect was negligible (above 4 K) in the Cu resistivity of set A but this does not, however, rule out the presence of MIs in the channel. Very low MI concentrations that are below the detection limits of charge transport are frequently observed in spin transport [41, 81]. The comparison of the spin and charge length scales in set A, depicted Figure 4.10(b), demonstrated that the additional temperature dependent spin scattering was limited to low temperatures. Studies of Kondo spin scattering from Co impurities in Cu are quite limited, but tend to show a spin scattering contribution that extends well up to room temperature due to the high $\mathrm{T}_{\mathrm{K}} \approx 500$ K [81, 97]. Additionally, the overall magnitude of τ_{sf} is severely reduced in Cu containing Co compared to Fe [81]; a consequence of the larger spin-flip cross section of Co compared to Fe or Ni in Cu [80, 82, 158] and the larger Kondo spin-flip scattering rate due to an increased s-d exchange constant $\mathrm{J} \approx 1.3$ eV (0.9 eV for Fe) [159, 160]. Therefore, to fit the total spin-flip scattering rate (τ_{sf}^{-1}) in set A, the Kondo parameters were fixed to typical values for Fe ($\mathrm{T}_{\mathrm{K}} = 30$ K, $\mathrm{s} = 0.21$) and α_{ph}, α_{def} and $\tau_{\mathrm{k},0}^{-1}$ were left as free fitting parameters.

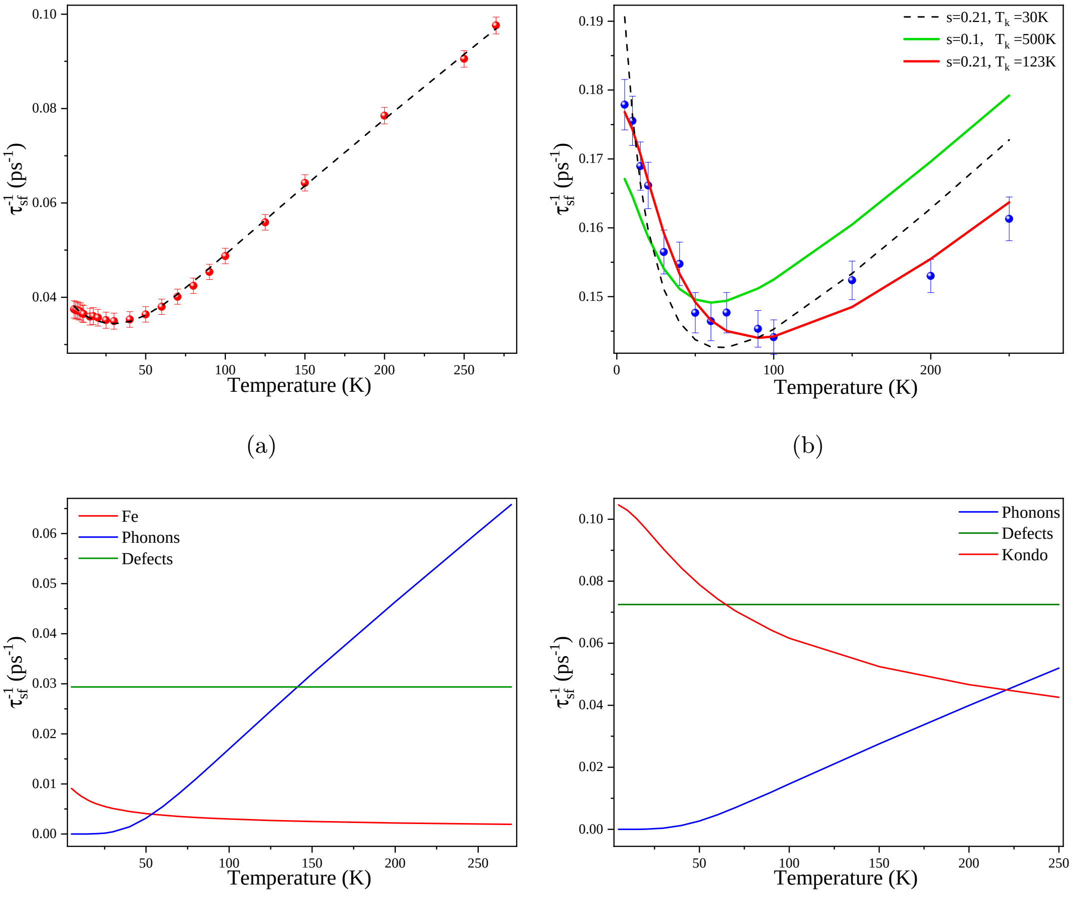

(a) (b)

(c) (d)

Figure 4.12: (a) The spin-flip scattering rate in set A with a fit to equation 4.4 (black dashed lines) assuming spin scattering contributions from phonons, defects and bulk Fe impurities. The temperature dependence of each spin scattering contribution extracted from the fit are depicted in (c) with phonons in blue, defects in green and Fe in red. (b) Spin-flip scattering rate in set B with three fits to equation 4.4, each using different values of the Kondo parameters (T_K and s): bulk Fe, with $T_K = 30K$ and $s = 0.21$ fixed, is depicted as the black dashed line; bulk Co, with $T_K = 500K$ and $s = 0.1$ fixed, is depicted as the green solid line; and, a mixed fit for scattering from both bulk Co and Fe impurities, with $s = 0.21$ fixed and $T_K = 123$ K as a free fitting parameter, is depicted as the red solid line. Only the latter fits the experimental data; the individual spin scattering contributions extracted from the fit are depicted in (d) with phonons in blue, defects in green and a mixed Kondo contribution in red.

The agreement between the data and fit is excellent; both are depicted in Figure 4.12(a) and the temperature dependence of each spin scattering contribution is plotted in Figure 4.12(c). The fit values were: $\alpha_{\mathrm{ph}} = (1.16 \pm 0.03)\mathrm{x}10^{-3}$, in agreement with values found in conduction electron spin resonance measurements (CESR) [80, 85]; $\alpha_{\mathrm{def}} = (9.45 \pm 0.05)\mathrm{x}10^{-4}$ which comparable to values extracted in Py/Cu LSVs from the same Cu source [78]; and, $\tau_{\mathrm{k,0}}^{-1} = (0.016 \pm 0.001)\mathrm{ps}^{-1}$. The low Fe concentration in this set is reflected in the small value of $\tau_{\mathrm{k,0}}^{-1}$. As shown in Figure 4.12(c), the contribution to the total spin-flip scattering rate from Kondo scattering by Fe ($\tau_{\mathrm{s,k}}^{-1}$) is negligible above 50 K thus phonons are the dominant source of spin-relaxation at high temperatures. Using the extracted value of $\tau_{\mathrm{k,0}}^{-1}$, the temperature at which Kondo scattering in τ_{e} would be visible was estimated to be $\mathrm{T} \approx 3$ K. It is therefore reasonable to assume that the additional low temperature spin scattering in set A is a result of dilute Fe impurities; which would be visible in the Cu resistivity if measurements were extended to a slightly lower temperature. It is interesting to note that the use of a thinner CoFe electrode seems to avoid contamination from Co entirely, even though the electrode material is composed of 70% Co.

The situation is quite different in set B. There is a detectable level of Fe impurities in the Cu resistivity, the spin relaxation time is suppressed, has a large low temperature suppression and a weak temperature dependence; all of which are indicative of high MI concentrations in the Cu bulk. In the initial fit, we test whether Fe impurities alone (which were detectable in the Cu resistivity) can account for the observed behaviour by fixing s and $\mathrm{T_K}$ to the values stated earlier and fix α_{ph} to the value returned from fitting set A. The fit is depicted as the black dashed line (labelled $\mathrm{s} = 0.21, \mathrm{T_K} = 30$ K) in Figure 4.12(b); due to the relatively low Kondo temperature of Fe, the fit cannot account for the very weak high temperature dependence and, in an attempt to do so, overestimates the spin scattering rate at low temperatures. This demonstrates that there are additional spin scattering mechanisms, other than Kondo scattering from Fe, present in the Cu of set B. The first possibility is Kondo scattering from dilute Co impurities in the Cu bulk. Based on previous reports, this is somewhat unexpected given the low miscibility of Co in Cu which tends to prevent the observation of bulk Co Kondo scattering without significant annealing (typically $\mathrm{T} > 300^{\circ}\mathrm{C}$) [81, 143, 161]. This previous study of shadow deposited Co/Cu LSVs used thin Co electrodes (15 nm), half the thickness of the CoFe electrodes in this set. The use of a thicker CoFe electrode here, and subsequent increase in CoFe deposits on the resist walls, may have led to the inclusion of Co deposits further into the channel along with Fe. To test Co impurities alone, τ_{sf}^{-1} was fitted with s= 0.11 with a fixed $\mathrm{T_K} = 500$ K, values found previously for Co in Cu [81]. Unfortunately, it did not reproduce any of the observed features (green line in Figure 4.12(b)). We note that the data can be fitted with two independent bulk Fe and Co Kondo scattering contributions, assuming no interactions between impurities, but the additive effects lead to a defect spin-flip probability of $\alpha_{\mathrm{def}} < 1\mathrm{x}10^{-3}$; which is much smaller than values found in clean LSVs [56, 78, 81]. Another possibility is that due to the random nature of the introduction of Co and Fe contaminants, and that these devices have not been annealed, there is a distribution of Co, Fe and clusters of each throughout the Cu channel which have different local $\mathrm{T_K}$ and S. As pointed out by other authors, a disordered system is better described by an average $\mathrm{T_K}$ and S of the entire distribution [163]. In equations 4.6 and 4.5, $\mathrm{T_K}$ and s are directly dependent upon one another; as $\mathrm{T_K}$ increases s decreases. Therefore, we are unable to obtain a precise estimate of either but only an indication of the range of possible values that fit the data. Consequently, τ_{sf} was fitted with s fixed at values between 0.05 and 0.5 and a free $\mathrm{T_K}$. Values between $0.17 < \mathrm{s} < 0.26$, which corresponds to an average impurity spin slightly greater than a half to just below a half, successfully fitted the data yielding: $\mathrm{T_K}=(123 \pm 5)$ K to $\mathrm{T_K}=(100 \pm 10)$ K, which are between the accepted values for dilute bulk Co and Fe; and $\alpha_{\mathrm{def}} = (1.42 \pm 0.03)\mathrm{x}10^{-3}$ to $\alpha_{\mathrm{def}} = (1.25 \pm 0.02)\mathrm{x}10^{-3}$, which is comparable other reported values for Cu [78]. The fit for s=0.21 and $\mathrm{T_K} = (123 \pm 5)$ K is depicted in Figure 4.12(b).

Alternatively, if the majority of the Co and Fe contaminants are concentrated at the surfaces/sides of the Cu channel as previously suggested [120], the spin-orbit anisotropy of the surface may suppress or quench the Kondo effect entirely [122, 123]. As a result, a significant proportion of the MIs close to the surface, particularly Co due to the integer S, will not Kondo scatter and would only spin-orbit scatter [140]. Whilst spin-orbit scattering alone is temperature independent, if these impurities are at the surfaces and $\lambda_{\mathrm{e}} < \mathrm{t_{Cu}}$, the probability of conduction electrons scattering from this contaminated region would increase with decreasing temperature as λ_e increases. This would appear as a high surface spin-flip probability and has been observed in shadow deposited Cu LSVs recently [106, 164]. To examine the possibility of a high surface spin-flip rate from contaminated surfaces in set B we follow the approach outlined by Y.Cai et al. [106], where a temperature dependent spin-flip probability (α_{sf}) was calculated directly from the EY relationship between ρ_{Cu} and λ_{Cu} as $\alpha_{\mathrm{Cu}} = \frac{1}{3}(\frac{\mathrm{mv_F}}{\mathrm{ne}^2\lambda_{\mathrm{Cu}}\rho_{\mathrm{Cu}}})^2$.

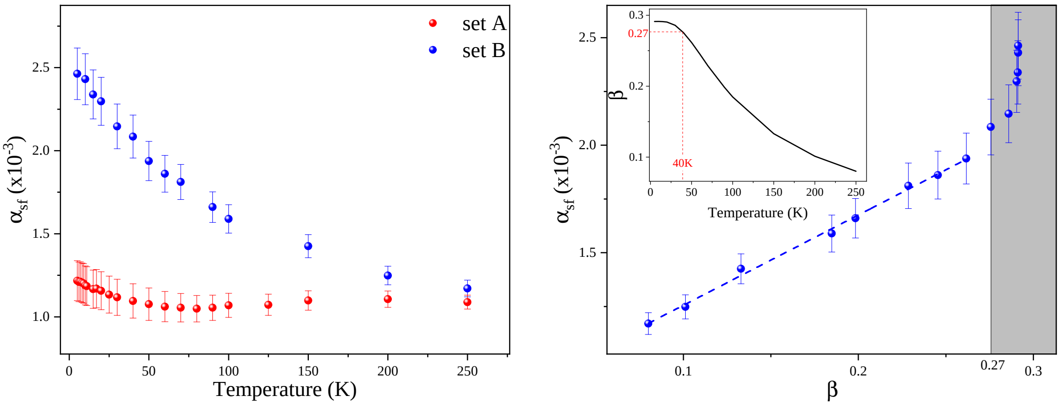

(a) (b)

Figure 4.13: (a) The temperature dependent spin-flip probability calculated from the EY relationship between the average resistivity and spin diffusion length of the Cu in LSVs from set A (red) and set B (blue). There is very little change in α_{sf} with temperature for set A, where in set B α_{sf} doubles upon cooling to 5 K. (b) The main figure depicts the increase in α_{sf} with the probability of surface scattering in set B. The inset shows the temperature dependence of the probability of surface scattering. α_{sf} increases linearly up to $\beta = 0.27$, which corresponds to the 40 K onset of Kondo scattering from Fe, and above which there is rapid increase. The blue dashed lines are a fit to $\alpha_{\mathrm{sf}} = \alpha_{\mathrm{bulk}} + (\alpha_{\mathrm{surfaces}} - \alpha_{\mathrm{bulk}})\beta$ in the linear region, where α_{bulk} and $\alpha_{\mathrm{surfaces}}$ are the probability of a spin-flip from the Cu bulk and surfaces respectively.

The calculated values of α_{sf} for both sets are shown in Figure 4.13(a). In set A, α_{sf} is roughly constant at $\alpha_{\mathrm{sf}} \approx 1\mathrm{x}10^{-3}$, which is close to the value of the phonon spin-flip probability extracted earlier, until the onset of Kondo scattering from Fe when $\mathrm{T} < 30$ K. This demonstrates that above 30 K phonons are the dominant source of spin-relaxation in these devices, in agreement with the previous analysis. The spin-flip probability in set B increases continuously upon cooling from $\alpha_{\mathrm{sf}} \approx 1\mathrm{x}10^{-3}$ at 250 K, close to expected value for phonons, to $\alpha_{\mathrm{sf}} \approx 2.5\mathrm{x}10^{-3}$ at 5 K. This demonstrates that another spin scattering mechanism with a higher spin-flip probability than phonons is increasingly dominant as the temperature reduces; either Kondo scattering from Co and Fe, as argued in the previous section, or scattering from the contaminated surfaces. To correlate the increase in α_{sf} with the probability of surface scattering, the probability of surface scattering per momentum scattering event was calculated as $\beta = \frac{\tau_{\mathrm{e}}}{\tau_{\mathrm{e-surf}}}$ [106], where $\tau_{\mathrm{e-surf}}$ is the average time for an electron to scatter from a surface. For an electron at the centre of the Cu channel in a 3D diffusive random walk, the average surface scattering time can be written as $\frac{1}{\tau_{\mathrm{e-surf}}} = 8\mathrm{D}(\frac{1}{\mathrm{w}^2} + \frac{1}{\mathrm{t}^2})$ [106], where D is the diffusion coefficient, w is the width of the Cu channel and t is the thickness. Figure 4.13(b) shows α_{sf} versus β, with an inset graph of β as a function of temperature. Of note, the spin-flip probability increases linearly with β up to $\beta = 0.27$, which as shown in the inset corresponds to the 40 K peak in the spin diffusion length, above which it increases rapidly. As stated earlier, the upturn in the Cu resistivity is direct evidence for the presence of Fe impurities in the Cu of this set thus the rapid increase in α_{sf} below 40 K is most likely the onset of Kondo scattering from these impurities. The linear dependence at higher temperatures ($0.1 < \beta < 0.3$) could be interpreted as the consequence of an increasing surface scattering contribution. When $\beta \to 0$, the scattering is predominately in the bulk and therefore the y-axis intercept will be approximately the bulk spin-flip probability (α_{bulk}). Likewise, the gradient of α_{sf} versus β will be the difference between α_{bulk} and $\alpha_{\mathrm{surfaces}}$. Fitting the relationship $\alpha_{\mathrm{sf}} = \alpha_{\mathrm{bulk}} + (\alpha_{\mathrm{surfaces}} - \alpha_{\mathrm{bulk}})\beta$ derived in [106] to the linear regime yields $\alpha_{\mathrm{surfaces}} = (5.06 \pm 0.08)\mathrm{x}10^{-3}$ and $\alpha_{\mathrm{bulk}} = (8.36 \pm 0.02)\mathrm{x}10^{-4}$. In this context, $\alpha_{\mathrm{surfaces}}$ is 6 times larger than α_{bulk} which would suggest a region of high spin-flip impurities at the surfaces. Additionally, no increase in α_{sf} with β is observed in set A suggesting that spin scattering from the surfaces is negligible for LSVs with thin CoFe electrodes.

Clearly, the spin scattering contributions from high $\mathrm{T_K}$ Kondo scattering and MI contaminated surfaces have very similar temperature dependences, so it is not possible to distinguish between these two explanations without further work. Regardless, these results demonstrate that the additional MIs introduced via the resist in the thick CoFe devices have dramatically reduced the spin diffusion length and spin relaxation time in the Cu channel.

4.4.2 Spin Polarisation

Fitting the spatial decay of $\Delta\mathrm{R_S}$ also yields the spin polarisation of CoFe (α_{CoFe}), which is related to the magnitude of the initial spin accumulation at the Cu/CoFe$_1$ interface. In the 1D diffusion equation, the spin polarisation is equivalent to the intrinsic spin current polarisation of the CoFe $\alpha_c = \frac{(\sigma_\uparrow - \sigma_\downarrow)}{(\sigma_\uparrow + \sigma_\downarrow)}$. In practice, however, the extracted value is an effective polarisation arising from the combined effects of α_c and the properties of the CoFe/Cu interfaces.

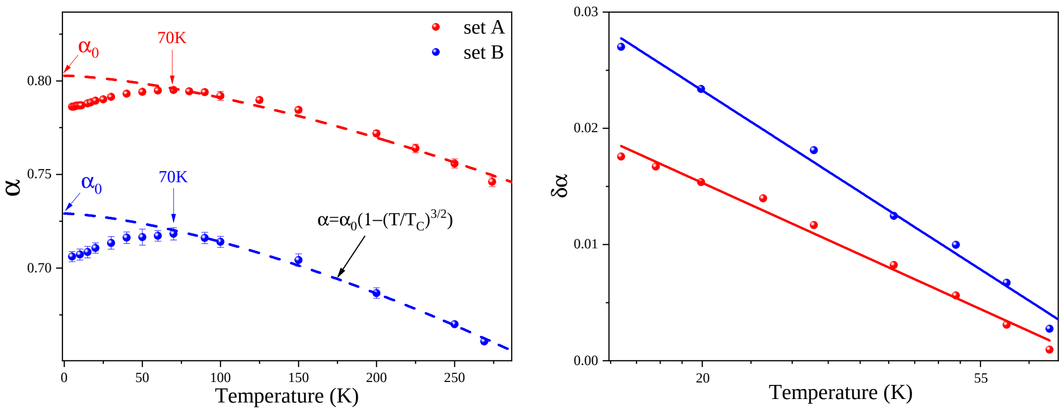

(a)

(b)

Figure 4.14: (a) The spin polarisation of each thickness of CoFe (15 nm in red and 30 nm in blue) extracted from fitting the spatial decay of ΔR_S in each set of LSVs. The dashed lines are fits to a Bloch law used to extract the intrinsic polarisation (α_0) and Curie temperaure, as detailed in the text. The maximum is a consequence of Kondo scattering from MIs at the CoFe/Cu interfaces and occurs at 70 K in both sets of LSVs. (b) To quantify the concentration of MIs at the interfaces, the deviation of the extracted polarisations from the Bloch fit $\delta\alpha = \frac{(\alpha_{\mathrm{CoFe}} - \alpha_{\mathrm{Bloch}})}{\alpha_0}$ is plotted on a logarithmic scale below the 70 K maximum. The straight lines are fits to a phenomological Kondo type expression $\delta\alpha = \delta\alpha_0(1 - \delta\alpha_{\mathrm{k}}\ln(\mathrm{T}))$, where $\delta\alpha_{\mathrm{k}}$ represents the concentration of MIs at the interfaces driving the deviation.

The temperature dependence of α_{CoFe} extracted from set A and B are depicted in Figure 4.14(a). To our knowledge this is the first report of the temperature dependence of α_{CoFe} in LSVs. Above 70 K, α_{CoFe} is dominated by the reduction of the intrinsic spin polarisation with temperature due to the increase in magnon population which causes spin mixing within the CoFe. This region can be well described by a Bloch type law $\alpha = \alpha_0(1 - (\frac{\mathrm{T}}{\mathrm{T_C}})^{\frac{3}{2}})$, where α_0 is the intrinsic polarisation at $\mathrm{T} = 0$ K and $\mathrm{T_C}$ is the Curie temperature. The Bloch fits are depicted as dashed lines in Figure 4.14(a) and yield values of: α_0=(0.73±0.02), α_0=(0.80±0.03) and $\mathrm{T_C}$=(1330±30) K, $\mathrm{T_C}$=(1520±30) K for sets B and A respectively. $\mathrm{T_C}$ of CoFe alloys varies between

1043 and 1600 K depending upon composition [165], in agreement our results. At low temperatures, where the Bloch law predicts that the intrinsic spin polarisation should saturate at α_0, both α_{CoFe} reduce below 70 K. This behaviour is widely observed in shadow deposited LSVs and is thought to be another manifestation of the Kondo effect [30, 41]. Due to the consecutive deposition of the FM and NM, interdiffusion during deposition creates a region of dilute MIs at the FM/NM interfaces. As a result, the spin accumulation at the injecting interface is depolarised through Kondo scattering prior to diffusing down the NM channel. The combination of the use of a 1D model, and the fact that the region is small in comparison with the channel length, results in this temperature dependent Kondo scattering manifesting itself as a logarithmic suppression of the extracted α_{FM}. This region, dubbed the 'Kondo region', has been proposed to have a much higher local density of MIs ($\approx$ 100ppm) than those occurring throughout the bulk of the transport channel leading to the higher temperature onset of Kondo scattering in α_{FM} than λ_{NM} [30, 98, 121]. To roughly estimate the concentration of MIs at the interfaces in each set, the deviation from the ideal Bloch case was calculated as $\delta\alpha = \frac{(\alpha_{\mathrm{CoFe}} - \alpha_{\mathrm{Bloch}})}{\alpha_0}$. Assuming that Kondo scattering is driving the deviation, a Kondo type expression can be used $\delta\alpha = \delta\alpha_0(1 - \delta\alpha_{\mathrm{k}}\ln(\mathrm{T}))$, where $\delta\alpha_{\mathrm{k}}$ is a parameter reflecting the concentration of impurities located at the interface [30]. As shown in Figure 4.14(b), both sets fit very well to a logarithmic dependence and yield values of $\delta\alpha_{\mathrm{k}}$=0.226±0.003 for set A and $\delta\alpha_{\mathrm{k}}$=0.222±0.002 for set B. These values are equivalent, indicating that the concentration of interdiffused MIs at the interfaces is not affected by differences in the CoFe thickness.

The maximum values at 70 K of $\alpha_{\mathrm{CoFe}} = 0.795 \pm 0.002$ and $\alpha_{\mathrm{CoFe}} = 0.718 \pm 0.004$ in set A and B respectively are amongst the highest extracted for similar composition CoFe alloys [43, 71]. However, this value is directly dependent upon our λ_{CoFe} estimation as the two parameters are coupled in equation 2.15. Interestingly, α_{CoFe} in set B is lower than set A at all temperatures. This is unlikely to be a result of changes to the intrinsic spin polarisation of the CoFe, which for other transition metal alloys has been shown to decrease with thickness [117, 118]. Again, directly comparing the magnitude of each α_{CoFe} can be misleading given that λ_{CoFe} for either CoFe thickness is unknown. Instead, the spin injection efficiency can be compared by calculating $\gamma = (\mathrm{R}_{\mathrm{CoFe}}\alpha_{\mathrm{CoFe}}\mathrm{A}_{\mathrm{CoFe}})^2$ [42], where $\mathrm{R}_{\mathrm{CoFe}}$ is the spin resistance of the CoFe injector given by $\mathrm{R}_{\mathrm{CoFe}} = \frac{(2\rho_{\mathrm{CoFe}}\lambda_{\mathrm{CoFe}})}{(\mathrm{A}_{\mathrm{CoFe}}(1-\alpha^2_{\mathrm{CoFe}}))}$ and $\mathrm{A}_{\mathrm{CoFe}}$ is the cross-sectional area of the CoFe injector perpendicular to the spin current. The spin diffusion length of ferromagnets are very short [10, 55, 154, 207], so the spin current will decay rapidly in the vicinity of the CoFe/Cu interface and the relevant region for spin relaxation is the injecting interface area $\mathrm{A_{CoFe} = w_{CoFe_1} w_{Cu}}$. γ is the dominant term in equation 2.15 that determines the y-axis offset of the entire $\Delta \mathrm{R_S(L)}$ curve and is proportional to the spin injection efficiency when $\mathrm{R_{FM} < R_{NM}}$, as in this work.

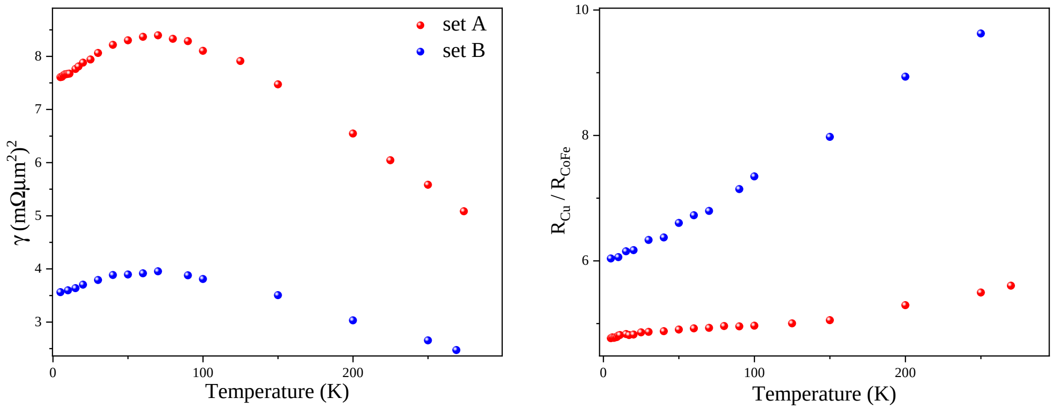

(a) (b)

Figure 4.15: (a) Calculated values of γ for each CoFe thickness (15 nm in red and 30 nm in blue), which is proportional to the efficiency of spin injection. For thin CoFe electrodes, γ and thus the spin injection efficiency is higher at all temperatures. The temperature dependence of γ follows the spin polarisation of the CoFe, which is the dominant term. (b) Calculated spin resistance ratio $\frac{\mathrm{R_{Cu}}}{\mathrm{R_{CoFe}}}$, which reflects the severity of the spin resistance mismatch between the Cu channel and CoFe injector. At all temperatures, the ratio is larger for the thick CoFe set (blue) suggesting that the spin resistance mismatch in these LSVs is more severe, the backflow of spins into the CoFe injector is larger and thus the spin injection efficiency is lower.

As shown in Figure 4.15(a), γ in set A is twice that in set B demonstrating that the spin injection efficiency is higher with thin CoFe electrodes. Given the identical deposition procedures for each set, and that the concentration of MIs at the interfaces are very similar, the lower injection efficiency in set B is likely related to the increased interface area. Although the patterned widths of the Cu and CoFe wires in each set are very close, if we consider that the sides of the CoFe wires are also in contact with the Cu channel the actual injecting interface area is $\mathrm{A_{CoFe} = w_{CoFe_1} w_{Cu} + 2(t_{CoFe} w_{Cu})}$. The injector interface area in set B $A_{CoFe} \approx 0.023\ \mu m^2$ is then about 30% larger than set A $A_{CoFe} \approx 0.018\ \mu m^2$. As pointed out by Kimura et al. [103], increasing the area of the injecting FM/NM interface exponentially decreases the injected spin polarisation and the magnitude of ΔR_s. This is because increasing the interface area, decreases the spin resistance of the FM injector and increases the backflow of injected spins; thus lowering the spin injection efficiency. Another potential factor is the lower CoFe resistivity in set B. It is generally assumed, without much experimental evidence, that $\rho_{FM} \propto \frac{1}{\lambda_{FM}}$. If true, then any decrease in ρ_{FM} will be counterbalanced by an increase in λ_{FM} and R_{FM} will remain unchanged. Otherwise, a reduction in the resistivity may decrease the spin resistance further, exacerbate the spin backflow and reduce the injected spin polarisation. Further work is required to examine the relationship between ρ_{FM} and λ_{FM} upon decreasing the thickness of the FM. As the severity of the spin backflow is determined by the relative sizes of R_{CoFe} and R_{Cu}, rather than R_{CoFe} alone, we compare the spin resistance ratio $\frac{R_{Cu}}{R_{CoFe}}$ which is large when $R_{CoFe} << R_{Cu}$ and the backflow of spins is high [41, 42, 44]. As shown in Figure 4.15(b), the spin resistance ratio is larger at all temperatures in set B indicating that the backflow of injected spins into the CoFe injector is higher.

4.5 Conclusions

In this chapter, the temperature dependence of charge and spin transport in shadow deposited CoFe/Cu LSVs with t_{CoFe}= 15 nm and 30 nm were investigated. Contamination of the Cu channel with CoFe electrode material was exacerbated by increasing t_{CoFe}, exemplified by the appearance of the charge Kondo effect in the 30 nm set. The presence of the Kondo effect in the Cu resistivity suggested that MI contaminants introduced in this way, even when unannealed, are not necessarily confined to the surfaces/edges of the Cu channel as was previously suggested [46, 120]. The spin signal was 2 to 4 times smaller at all electrode separations in the 30 nm set; primarily as a result of the shorter λ_{Cu} and to a lesser extent a lower α_{CoFe}. In the 15 nm set, a long λ_{Cu} was obtained which was toward the higher end of published values. Increased Cu contamination from the CoFe electrode material in the 30 nm set led to a dramatic reduction of λ_{Cu}. Spin scattering from these contaminants led to multiple temperature dependent contributions that distorted and suppressed the spin relaxation time from the conventional EY expectation of $\tau_{sf} \propto \tau_e$. The behaviour could not be entirely accounted for by spin scattering from the Fe impurities, which were detectable in charge transport. It was suggested that there were additional spin scattering contributions either from high T_K bulk Kondo scattering from Co, or heavily contaminated regions at the surfaces. Unfortunately, both interpretations have very similar temperature dependences and consequently, the present results are ambiguous. To attempt to distinguish between the two, the MMA protective coating was removed with acetone from a set of t_{CoFe}= 30 nm devices and were left to oxidise at atmosphere. As suggested in [120], eventually a layer of CuO (about 6 nm thick) would form at the exposed sides/surfaces and render any MIs in this region inaccessible to the electrons. If the weak temperature dependence of τ_{sf} was a result of a high surface spin-flip probability rather than bulk Kondo effects, we would have observed a return to a slightly more EY like high temperature behaviour. Unfortunately, due to COVID–19, this work could not be completed. The efficiency of spin injection was also lower in the 30 nm set and was suggested to be a consequence of the increase in injection interface area and potentially the lower CoFe resistivity; both of which lowered the spin resistance of the CoFe and increased the backflow of spins into the CoFe. This work has demonstrated that the electrode thickness is an important parameter in shadow deposited devices. The use of a thinner electrode appears to be a wiser choice to achieve a higher spin injection efficiency and longer spin diffusion length.

Chapter 5

Thermal Effects in Lateral Spin Valves

5.1 Introduction

Thermal effects in lateral spin valves (LSVs) have generally been overlooked, and misinterpreted, since their inception in the early 2000's. In 2005, Garzon et al. [52] observed an unexpected asymmetry in the temperature dependence of the parallel ($\mathrm{R_P}$) and antiparallel ($\mathrm{R_{AP}}$) spin resistance states. The effect was attributed to a temperature dependent interfacial spin scattering at the ferromagnetic/non-magnetic (FM/NM) interfaces. A similar observation in 2007 by Johnson and Silsbee [166] led to a different conclusion; they proposed that the assumption of a quasi 1D wire, which is necessary for symmetric $\mathrm{R_{AP}}$ and $\mathrm{R_P}$ states, veered too far from reality. They concluded that this deviation from an ideal geometry led to the asymmetry between the electrode states, which then coined the name 'baseline resistance' or BLR. Up to this point, all measurements were performed with lock–in amplifiers that examine only the linear response to the injection current. Direct current (DC) measurements by Casanova et al. [50] revealed the ohmic nature of the BLR and suggested an inhomogeneous current density as the culprit. Their measurements also revealed an additional background signal, not identifiable in alternating current (AC) measurements, which arose as a consequence of Joule heating in the path of the injection current. Before long, Bakker et al. [58] suggested that the BLR was also thermal in origin and arose from the Peltier heating/cooling of the injecting interface. The thermal origins of both background signals were confirmed by Kasai et al. [167] by fabricating LSVs on two substrates with very different thermal conductivities; the spin signal ($\Delta \mathrm{R_S}$) remained the same, but the BLR and Joule heating voltages were greatly reduced on the high thermal conductivity substrate. In recent work by the author's colleague Dr G. Stefanou [4], Scanning Thermal Microscopy (ShTM) enabled the direct observation of the temperature distribution within a Py/Ag LSV under current bias at room temperature. This technique directly imaged the Peltier heating/cooling at the injecting interface for the first time and identified that the exposed region of the FM was a 'hot spot' and the primary source of Joule heating in the LSVs.

Although thermal effects were originally viewed as unwanted background signals to be minimised, many groups have now taken advantage of the interplay between spin and heat currents spawning the field 'spin caloritronics'. Studying high bias effects on LSVs, M. Erehinsky et al. [37] identified that under large thermal gradients additional spin injection through the Spin Dependent Seebeck Effect (SDSE) could contribute to the non-local voltage. LSVs deposited upon low thermal conductivity (Si–N) membranes showed a dramatic enhancement in thermal phenomena and revealed that under these extreme conditions an additional thermal effect arose as a result of temperature gradients within the FMs – the Anomalous Nernst Effect (ANE) [57]. Additionally, under large current biases, Joule heating was demonstrated to have a significant impact on spin transport [50].

Central to this field is the understanding of thermal transport and thermoelectric properties of metallic elements as their dimensions approach the nanoscale. In particular, the distribution of heat currents, calculations of thermal gradients, measurements of nanoscale thermal conductivities and thermopowers. Specific to the LSV, the complexity of nanoscale thermal transport has so far precluded explanation of the length dependent decay and temperature dependence of the thermal signals arising from the Joule and Peltier effects. In this chapter, the thermal background signals arising in Cu/$Co_{70}Fe_{30}$ LSVs are examined for the first time. It is expected that the thermal background voltages arise from the Peltier heating/cooling at the interface and Joule heating. Although the origins of these effects are now widely accepted, their variations with temperature and transport length have been given very little attention in the literature.

5.2 Non-Local Voltages

The devices considered here are $Co_{70}Fe_{30}$(15 nm)/Cu(100 nm) LSVs upon a SiO_2(100 nm)/Si substrate, with lateral geometries of $W_{Cu} \approx 100$ nm, $W_{CoFe_1} \approx 120$ nm and $W_{CoFe_2} \approx 140$ nm. Critical to the thermal effects are the conditions around the LSV during the measurement; all devices were measured in a shielded cryostat with inert He gas flow to control the measurement temperature (T_m). Each device was thermally anchored with Ag paint to an O_2 free Cu measurement head which acted as a heat sink. Prior to each measurement, stringent temperature stability criteria (±20 mK) ensured that the substrate temperature $T_s \approx T_m$. Non-local measurements were performed under DC bias with a maximum applied current of $I_c = 500$ μA, following the procedure outlined in the previous chapters.

5.2.1 Heat Generation and Detection

During a non-local measurement there are two sources of heat generation: Joule heating and the Peltier effect. The electrical current produces Joule heating over the entire current path (depicted in Figure 5.1) according to $P_{\mathrm{Joule}} = I_c^2R$. ShTM measurements on geometrically similar Py/Ag LSVs [4] identified that the majority of the Joule heat was produced in the exposed region of the Py injector, due primarily to the resistivity of Py being greater than Ag by a factor of ten. Since there is also a factor of ten difference between the resistivity of Cu ($\rho_0 \approx 1.5$ µΩcm) and CoFe ($\rho_0 \approx 20$ µΩcm) used in this work, it was assumed that the exposed region of the $CoFe_1$ injector would also be the primary source of Joule heating.

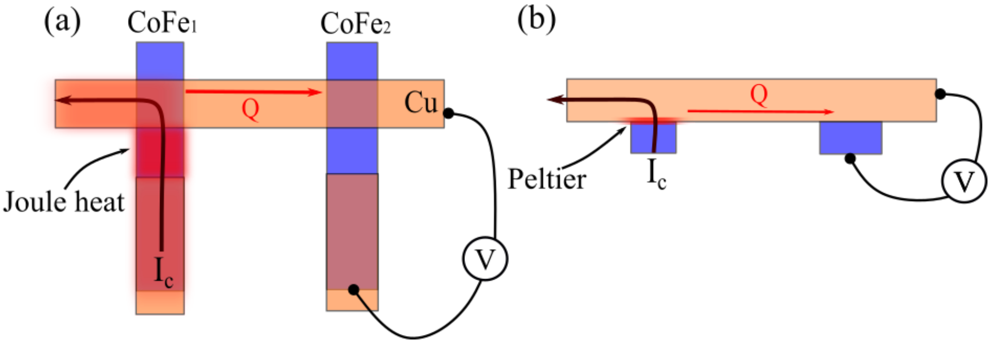

Figure 5.1: Schematic of an LSV in a non-local measurement scheme depicting the sources of heat generation. (a) Aerial view of device: Joule heat is produced over the entire current path (indicated in red), with a significant proportion generated in the exposed region of the $CoFe_1$ electrode due to its high resistivity. (b) Side view: Peltier heating/cooling occurs at the $CoFe_1$/Cu interface. Heat currents (Q) generated by each effect are primarily transported along the Cu channel toward the $CoFe_2$/Cu interface.

As suggested by Bakker et al.[58], the flow of the electrical current through the injecting $CoFe_1$/Cu interface results in local Peltier heating/cooling. This is a consequence of the difference in heat currents carried by the conduction electrons, represented by the absolute Peltier coefficients Π_{CoFe} and Π_{Cu}, either side of the interface. In order to maintain charge neutrality, there is a discontinuity in the heat current at the interface resulting in local heating or cooling depending on the direction of the current flow. The Peltier heat is given by $\dot{Q}_P = \Pi_{\mathrm{CoFe,Cu}} J$, where J is the current density and $\Pi_{\mathrm{CoFe,Cu}} = \Pi_{\mathrm{CoFe}} - \Pi_{\mathrm{Cu}}$.

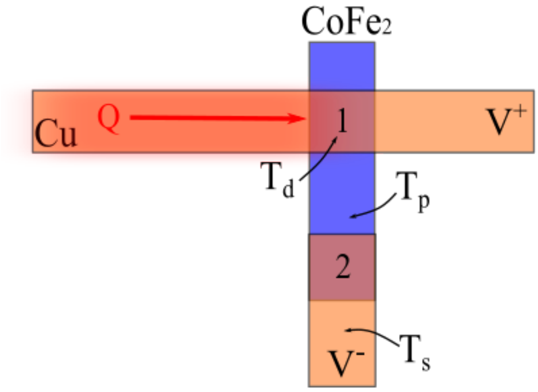

Figure 5.2: Schematic of the $CoFe_2$/Cu detecting interface depicting the positive and negative voltage terminals.

The heat currents produced by Joule and Peltier heating in the injecting side of the device flow into the SiO_2/Si substrate and along both directions of the Cu channel. Although the contact area between the device and substrate is large, the high thermal conductivity of the Cu (k_{Cu}) compared to the substrate results in a considerable thermal current diffusing along the Cu toward the $CoFe_2$/Cu detecting interface. This raises the temperature of the detecting interface (T_d) with respect to the substrate (T_s). The detector circuit then acts as a thermocouple producing a measurable Seebeck voltage in response to each heating effect. A schematic of the detector circuit is depicted in Figure 5.2. Between the positive and negative voltage probes there are two interfaces: (1) where the Cu channel overlays the CoFe electrode (the detection interface) at some temperature T_d and (2) where the Cu connection to the voltage probe is made at a temperature T_p. Equating the electrochemical potential at both interfaces [7] leads to:

$$\mu^1_{Cu}(T_s) - \mu^2_{Cu}(T_s) = |e| \left[\int_{T_d}^{T_s} S_{Cu} dT + \int_{T_d}^{T_p} S_{CoFe} dT + \int_{T_s}^{T_p} S_{Cu} dT \right] \tag{5.1}$$

where, $\mu^1_{Cu}(T_s)$ is the electrochemical potential of the Cu at $T = T_s$ and S_{Cu} and S_{CoFe} are the absolute Seebeck coefficients for Cu and CoFe. Previous ShTM measurements on similar Py/Ag LSVs [4] demonstrated that the contact pad was at the same temperature as the substrate $T_p = T_s$ (at least at room temperature), which gives the total Seebeck voltage detected as:

$$\nabla\mathrm{V} = \mathrm{V}^1_{\mathrm{Cu}}(\mathrm{T_s}) - \mathrm{V}^2_{\mathrm{Cu}}(\mathrm{T_s}) = (\mathrm{S_{Cu}}(\mathrm{T_s}) - \mathrm{S_{CoFe}}(\mathrm{T_s}))(\nabla\mathrm{T}) \tag{5.2}$$

where, $\nabla\mathrm{T} = \mathrm{T_d} - \mathrm{T_s}$. Since we have used DC bias, the temperature changes induced by Joule heating will vary as $\nabla\mathrm{T} \propto \mathrm{I}^2$ and the Joule induced Seebeck voltage will be quadratic in applied current. Conversely, the linear current dependence of the Peltier effect leads to $\nabla\mathrm{T} \propto \mathrm{I}$ across the detecting interface thus a linear Seebeck voltage.

5.2.2 Response Regime

In the linear response regime the transport coefficients that dictate device response are constant. In the context of a non-local measurement, this means that the spin, charge and thermal coefficients (all of which are strongly temperature dependent) do not change during a non-local voltage measurement. The non-local voltage in the linear regime takes the form of a second order polynomial:

$$\mathrm{V_{NL}} = \mathrm{R_1 I} + \mathrm{R_2 I^2} + \mathrm{c} \tag{5.3}$$

where, the linear coefficient ($\mathrm{R_1}$) contains the linear voltage responses, namely, the spin accumulation and Peltier induced Seebeck voltage. Here, $\mathrm{R_2}$ contains the quadratic voltage responses brought about by Joule heating, which we expect to be limited to the Joule induced Seebeck voltage, and c is an offset from the measurement equipment. If the Joule heating induced temperature changes ($\propto \mathrm{I}^2$) are large enough to change the transport coefficients during a non-local voltage measurement higher order voltages arise. In this instance, the device response is in the non-linear regime and the non-local voltage becomes:

$$\mathrm{V_{NL}} = \mathrm{R_1 I} + \mathrm{R_2 I^2} + \mathrm{R_3 I^3} + \mathrm{R_4 I^4} + \ldots \tag{5.4}$$

where, the $\mathrm{R_3}$ term is produced by Joule heating induced temperature changes to the linear term $\mathrm{R_1}$. Similarly, the $\mathrm{R_4}$ term is a result of Joule heating on the quadratic term $\mathrm{R_2}$.

Non-Linear Responses

Previously, non-linear responses have been observed in lateral devices where thermal effects are intentionally exacerbated through the use of low thermal conductivity substrates [57] or under large current biases [58]. The devices considered in this work were fabricated on a moderate thermal conductivity SiO_2/Si substrate and exposed to comparatively low current densities: a maximum of $J_{max} \approx 2x10^{11}$ A/m^2 in the $CoFe_1$ electrode; $J_{max} \approx 3.2x10^{10}$ A/m^2 in the Cu channel; and, $J_{max} \approx 3.3x10^{10}$ A/m^2 at the $CoFe_1$/Cu interface. Indeed, studies measuring devices in very similar conditions to this work have assumed a purely linear response, as relatively good fits to V_{NL} are obtained with a 2nd order polynomial. For a closer examination of the current dependences arising in our non-local measurements, we consider the form of V_{NL} in the parallel (V_P) and anti-parallel (V_{AP}) electrode states. The purely thermal voltages arising from Peltier and Joule heating will have no dependence on the alignment of the magnetic electrodes, whereas spin dependent voltages will reverse polarity as the electrodes switch between the P and AP states. Therefore, the spin dependent voltage can be obtained as $V_S = V_P - V_{AP}$ and the thermal voltage as $V_T = V_P + V_{AP}$.

Figure 5.3(a) depicts V_S from an L $\approx$ 800 nm device at 5 and 150 K. At both temperatures, V_S appears to be linear and reversible; as expected from the known behaviour of the spin accumulation under electrical spin injection [3, 50, 167]. We note, however, this apparent linear dependence is deceiving. To demonstrate this the differential spin resistance dV_s/dI was calculated, shown in Figure 5.3(b), which should be a constant if V_S contains no higher order voltage components. At 5 K, there is a small positive I^2 term (a fit is depicted as the black line) which suggests that the spin voltage at this temperature is a superposition of the linear response $R_1^S I$ and a higher order response $R_3^S I^3$. This higher order term is not present at 150 K. V_T is depicted in Figure 5.3(c) and in the linear regime is expected to be a combination of the quadratic and linear voltages arising from Joule and Peltier heating, which appears to be the case at both temperatures. However, upon examining the differential resistance (dV_T/dI), there are significant differences between the thermal responses at 5 and 150 K. In the linear response regime, the thermal voltage can be written as $V_T = 2R_2I^2 + 2R_1^{Peltier}I$, thus the differential resistance should be linear $dV_T/dI = 4R_2I + R_1$. As shown in Figure 5.3(d), at 150 K dV_T/dI is linear, whereas at 5 K dV_T/dI contains an additional term which varies as I^3. This corresponds to a fourth order thermal voltage response

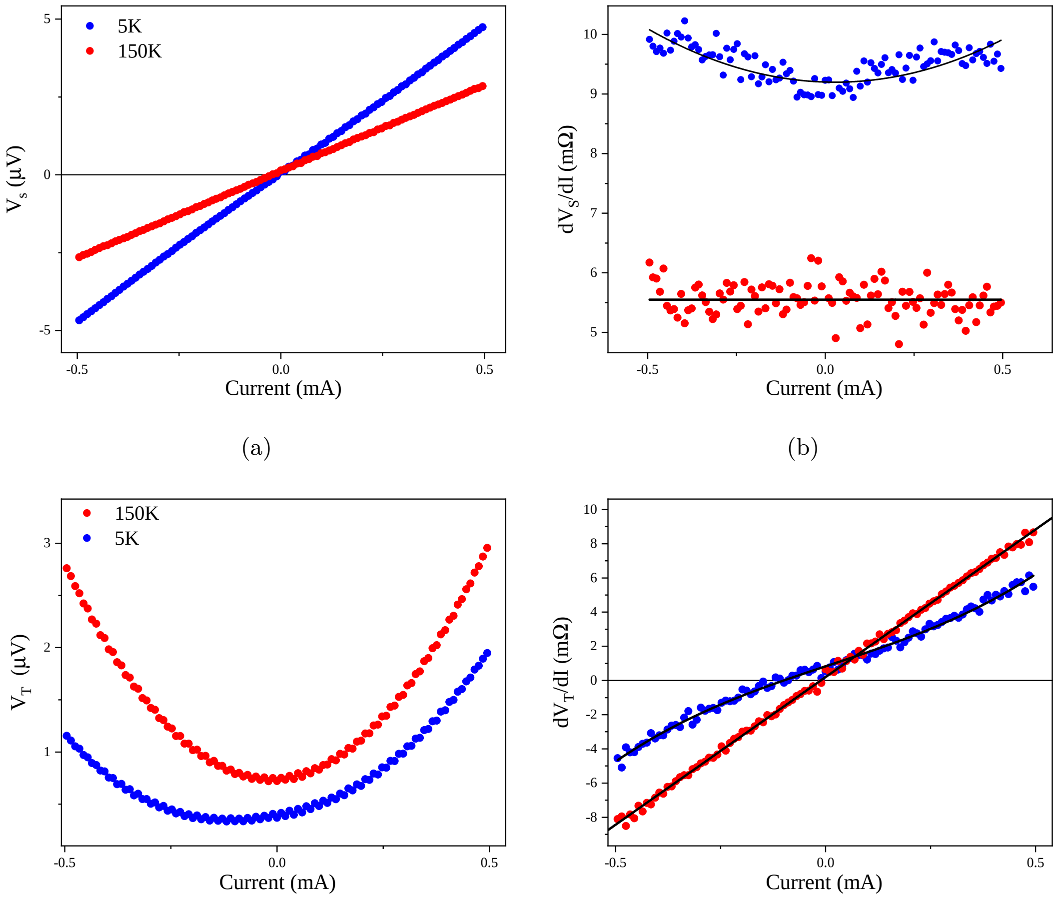

(a) (b)

(c) (d)

Figure 5.3: Spin (a) and thermal (c) voltages extracted from the non-local voltage in the P and AP states, as detailed in the text. Two measurements are shown at 5 and 150 K from an L ≈ 800 nm LSV. At 150 K, the differential spin resistance (b) is constant which demonstrates that the spin voltage contains no higher order terms. At 5 K, the differential spin resistance contains an I^2 term (fit as black line) which corresponds to a higher order $R_3^S I^3$ term in the spin voltage. Similarly, the differential thermal resistance (d) contains no higher order voltages at 150 K; whereas, at 5 K it contains an I^3 term (fit as black line) which corresponds to a $R_4 I^4$ term in the thermal voltage.

($R_4 I^4$) which emerges at low temperatures.

Fitting Non-Local Voltages

Close examination of the thermal and spin voltages suggests that the device response becomes non-linear at low temperatures. This is not entirely surprising given the mesoscopic device dimensions and that heat flow into the substrate should be greatly reduced at low temperatures [168]. To determine the temperature at which the transition occurs, 4th and 2nd order polynomials were fitted to V_{NL} at each applied field, within each T_m, for every LSV. In the linear response regime, where the R_3 and R_4 terms are negligible, the 2nd and 4th order fits will be equivalent. Figure 5.4 depicts the average χ^2 parameter (used here as an indicator of 'goodness of fit') at each T_m for 2nd and 4th order fits to a single LSV. χ^2 is equivalent for the 2nd and 4th order fits down to 20 K, below which it increases for the 2nd order fit only. This indicates that below 20 K the device response has been driven into the non-linear regime and the higher order terms R_3 and R_4 are no longer negligible.

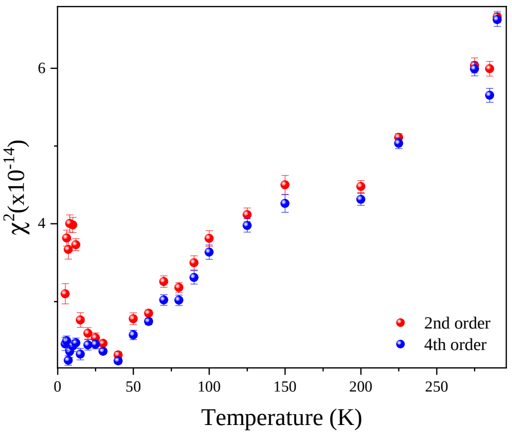

Figure 5.4: Average χ^2 parameter at each measurement temperature for 4th and 2nd order fits to the non-local voltage. Overall, both χ^2 reduce as the temperature decreases due to the increasing signal to noise ratio. The upturn in χ^2 below 20K for the 2nd order fit corresponds to the onset of non-linear device response regime, where a 4th order fit is required to accurately represent the device response.

Figure 5.5 shows two V_{NL} with 2nd and 4th order fits from temperatures above and below this transition. Both fits are equivalent at 50 K, whereas at 10 K the 4th

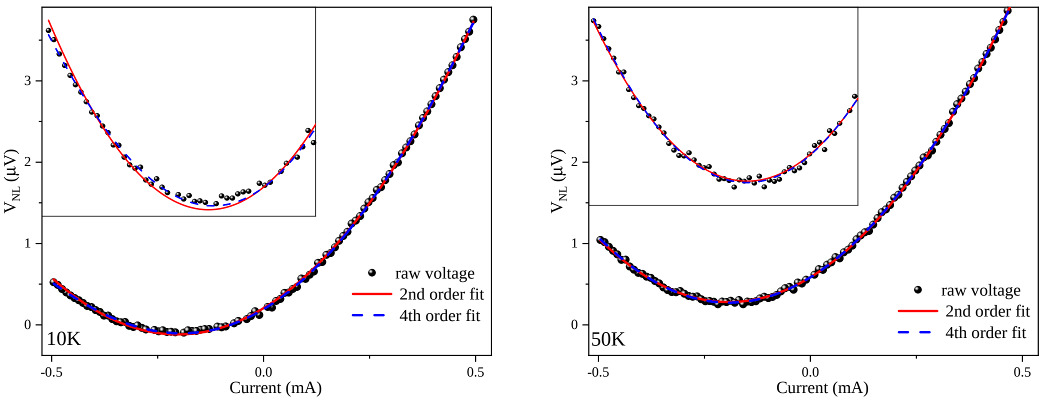

(a)

(b)

Figure 5.5: An example of the non-local voltage measured at 10 K (a) and 50 K (b) with 4th (blue) and 2nd order (red) polynomial fits. The inset graph shows an expanded view of the main figure between $-0.5\text{mA} > \text{I}_\text{C} > 0\text{mA}$, to highlight the differences between the 4th and 2nd order fits that are only present at 10 K.

order fit is slightly better. The inset graph of Figure 5.5(a) shows an expanded view of part of the main figure to illustrate this more clearly. As the difference is very small, it is difficult to identify from fitting the non-local voltages alone and reinforces the need to examine the differential resistances to identify small higher order voltages in these studies. For each LSV, V_NL was fitted to a 4th order polynomial to extract the magnetic field dependence of each voltage contribution at each measurement temperature.

5.3 Magnetic Field Dependence

Quadratic Term - R_2

An example of the quadratic voltage (R_2I^2) as a function of applied current in the P and AP electrode states at 100 K is shown in Figure 5.6(a). In addition, Figure 5.6(b) shows the extracted quadratic coefficient (R_2) at three temperatures against the applied magnetic field. Clearly, the quadratic response has no dependence on the small magnetic fields required to align the CoFe electrodes and no dependence on their magnetisation orientation. As stated previously, this term is a consequence of Joule heating from the injection current which is converted into a voltage through the Seebeck effect at the

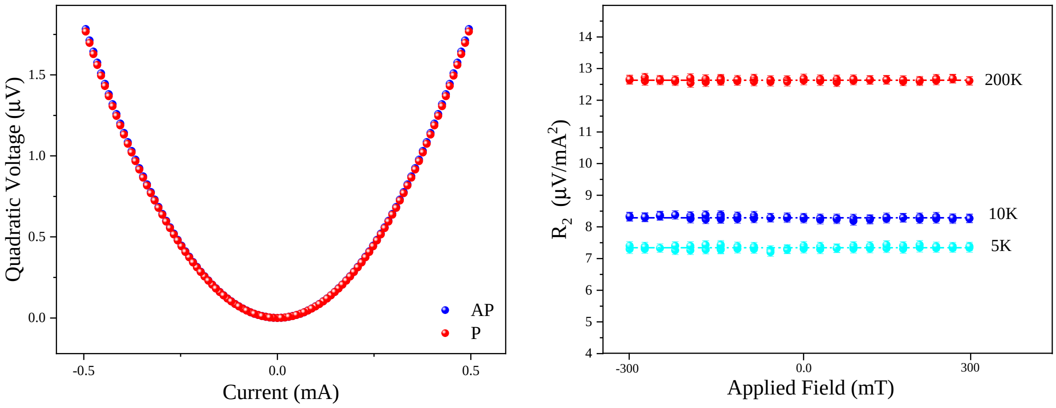

(a)

(b)

Figure 5.6: (a) The quadratic voltage response in the P and AP electrode magnetisation states at 100 K. (b) Applied field dependence of quadratic coefficient (R_2) at three temperatures. The applied magnetic field and magnetic configuration of the electrodes have no effect on the quadratic voltage measured.

detector. It is well known that magnetic fields can lead to resistance changes in CoFe and Cu [169], which could alter the Joule heating and absolute Seebeck coefficients. For relatively pure Cu, resistance changes from magnetic fields of a similar magnitude to those used in this study (< 300 mT) are negligible and changes to the Seebeck coefficient are equally as small; even for a 2.7 T field at room temperature $\Delta S < 1$ nV/K [170]. In FMs, the phenomenon of anisotropic magnetoresistance (AMR) leads to changes in the resistivity which depend on the angle (θ) between the charge current (I_c) and magnetisation ($\mathbf{M}$) as: $\rho(\theta) = \rho_\perp + (\rho_\parallel + \rho_\perp)\cos^2(\theta)$. In our case, both CoFe electrodes were designed to switch with the injection of a single domain wall (no continuous rotation of $\mathbf{M}$) from $\theta=0^o$ to $\theta=180^o$. Given that $\rho_{0^o}=\rho_{180^o}=\rho_\parallel$, no AMR effects are observed. Similarly, the spin-orbit coupling (SOC) induced anisotropy that is at the heart of AMR also leads to changes in the Seebeck coefficient (thermopower) of FMs [171]. This anisotropic magneto-thermopower depends on the angle between $\mathbf{M}$ and ∇T, again with a $\cos^2(\theta)$ dependence [172]. The argument given above for the lack of AMR in the devices also applies, so no anisotropic effects in S_{CoFe} are observed. Therefore, an average R_2 with standard error was calculated for each measurement temperature.

Linear Term - R_1

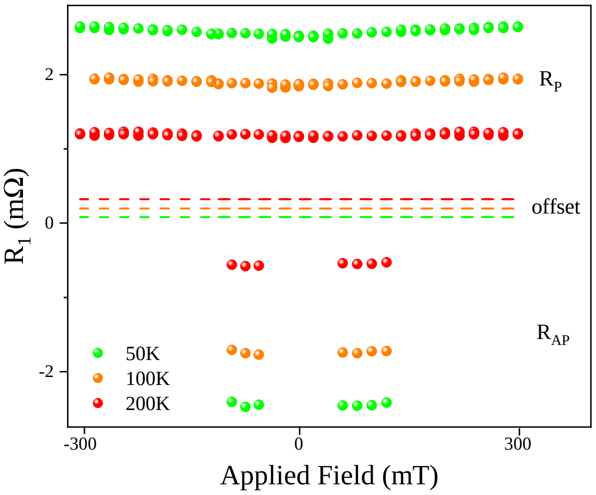

Figure 5.7: The applied field dependence of the linear coefficient at three temperatures. The spin dependent resistance reverses polarity as the CoFe electrodes switch between the parallel (R_P) and anti-parallel (R_{AP}) states. As detailed in Chapter 4, the spin signal is given by $\Delta R_S = R_P - R_{AP}$ and reduces in magnitude with increasing temperature due to thermally induced spin scattering in the Cu and loss of spin polarisation in the CoFe. In contrast, the offset voltage induced by the Peltier heating (dashed lines) has no magnetic field dependence and increases with temperature.

The linear voltage response contains two terms: the spin accumulation induced voltage and the thermal voltage arising from the Peltier heating/cooling at the injection interface. As outlined in Chapter 4, the two can be separated by considering the differences in the magnetic field dependence of each. Akin to the thermopower, the Peltier coefficient is anisotropic in FMs due to the anisotropic magneto-Peltier effect [173]. In this instance, Π varies as $\cos^2(\theta)$, where θ is the angle between I_c and **M**. Once again, given the $\cos^2(\theta)$ dependence, no changes in Π occur during the field sweep. Therefore, the Peltier induced thermal voltage is manifested as a constant offset between the R_P and R_{AP} spin states (depicted as the dashed lines in Figure 5.7) and can be calculated as $R^1_{\text{offset}} = \frac{R_P + R_{AP}}{2}$ at each measurement temperature. At low temperatures, the offset voltage is small and the R_P and R_{AP} spin resistance states are nearly symmetric about zero. The offset voltage increases with temperature, in part due to the increase in the Peltier heat generated. The temperature dependence of the offset voltage will be discussed in more detail later in this chapter. Note that the offset voltage is the BLR referred to in other work.

As a brief aside, we note that further thermal effects have been observed in the linear voltage response of LSVs namely, ANE and the Thermal Hall Effect (THE) [57, 174]. Convetionally, ANE is observed in FMs and occurs when there is a thermal gradient perpendicular to the magnetisation. It produces a transverse voltage which reverses with the reversal of the magnetisation. In an LSV this effect may occur in the FM voltage probe as a result of the thermal gradient produced via Joule/Peltier heating at the injecting interface. It is identifiable as an asymmetry between each $\mathrm{R_P}$ (and $\mathrm{R_{AP}}$) state (akin to the addition of a magnetic hysteresis loop to the linear response) and is largest at high temperatures where the Seebeck/Peltier coefficients are considerable. A similar asymmetry arises from the THE, which occurs instead in the injecting electrode. Neither of these effects are observable in any of our measurements.

Fourth Order Term - $\mathrm{R_4}$

The $\mathrm{R_4}$ term is negligible until the temperature falls below 20 K for every LSV. Figure 5.8 shows the applied field dependence of $\mathrm{R_4}$ at two temperatures. Although noisy given the small signal, $\mathrm{R_4}$ has no dependence on the applied field or the magnetisation of the CoFe electrodes. From the current dependence it can be surmised that this term is a result of Joule heating induced temperature dependent changes to $\mathrm{R_2}$; the lack of field and magnetisation dependence supports this suggestion. At each measurement temperature an average $\mathrm{R_4}$ with standard error was calculated.

Third Order Term - $\mathrm{R_3}$

$\mathrm{R_3}$ is significantly smaller than the other voltage contributions and only above the noise level in the lowest separation LSVs. An example of the field dependence of $\mathrm{R_3}$ is depicted in Figure 5.9. Akin to $\mathrm{R_1}$, it consists of a positive spin signal ($\Delta\mathrm{R_S^3} = \mathrm{R_P^3}$ - $\mathrm{R_{AP}^3}$) and a small thermal offset ($\mathrm{R^3_{offset}}$). As this higher order spin signal varies as $\mathrm{I^3}$, it is not a result of additional spin injection from the SDSE nor thermally assisted spin injection [37, 57]. Both mechanisms are generated by thermal gradients in the injecting electrode, which at low temperatures are predominantly generated by Joule

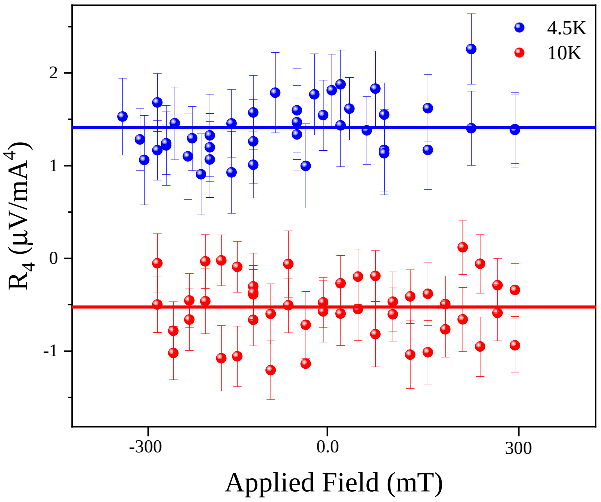

Figure 5.8: Applied field dependence of the fourth order coefficient in an L = 600 nm LSV. This term has no discernable magnetic field dependence (the solid lines are guides to the eye) and does not change with the magnetic state of the CoFe electrodes, allowing for an average value to be calculated at each measurement temperature.

heating (as the Peltier heat tends toward zero with the thermopower) and would lead to spin dependent voltages that vary as I^2. Moreover, the spin dependent component of R_3 is dependent on the magnetic alignment of the CoFe electrodes in the same way as the first order spin dependent resistances depicted in Figure 5.7. Therefore, the most likely origin of this third order spin dependent term is the Joule induced heating of the first order spin response, as observed previously [50, 58]. In contrast to [58], where this higher order spin signal was negative, ours is positive. This is because the onset of ΔR_S^3 in this case occurs below 30 K, where the first order spin signal is reducing with decreasing temperature due to Kondo scattering (see Chapter 4). Consequently, an increase in local device temperature leads to a positive ΔR_S^3. A similar effect was observed at 4.2 K by Casanova et al. [50]. Similarly, the thermal offset in this term is a result of temperature dependent changes to the offset voltage, R^1_{offset}.

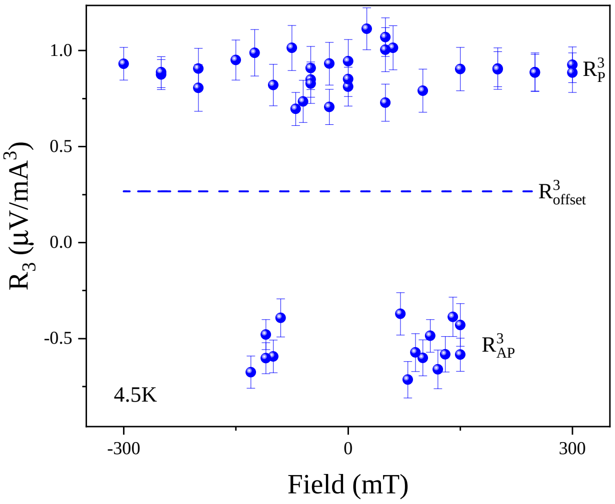

Figure 5.9: Applied field dependence of the third order coefficient at 4.5 K in an L = 600 nm LSV. This term contains a spin dependent resistance that switches from positive (R^3_P), when the CoFe electrodes are in the P state, to negative (R^3_{AP}), when the electrodes are in the AP state, which is characteristic of the spin accumulation induced resistance. The difference between the P and AP states yields the third-order spin signal (ΔR^3_S). Moreover, as the P and AP states are not quite symmetric about zero, this term contains an additional thermal offset (R^3_{offset}, dashed lines) which remains constant with applied field.

5.4 Temperature Dependence of Thermal Signals

From the current and field dependences of the higher order thermal voltages we anticipate that they arise as a result of Joule heating induced changes to the quadratic voltage and linear offset voltage; with the even terms originating from Joule heating and odd terms from Peltier. Figure 5.10 depicts the temperature dependence of the even voltage response terms (a) and the odd voltage responses (b). It is immediately clear is that there is a link between the V_2 and V_4 responses; they follow a similar, but opposing, temperature dependence. Similarly, at low temperatures where V^1_{offset} is very small ($\approx$ 0.01 μV) and slowly decreasing, the V^3_{offset} term is of a similar magnitude and increasing as the temperature falls to 0 K. This suggests that the higher voltages are

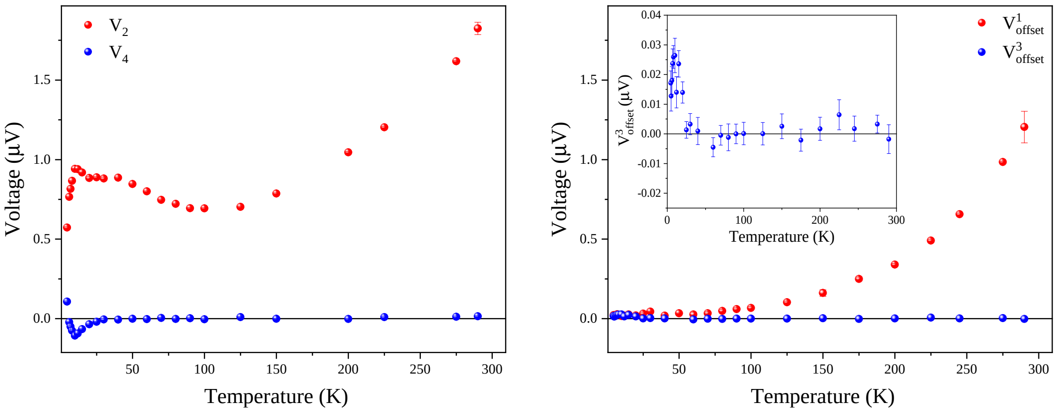

(a)

(b)

Figure 5.10: Temperature dependence of the even (a) and odd (b) in applied current thermal voltages in an L = 600 nm LSV. The higher order voltages (V_4 and V^3_{offset}) are negligible above 20 K. Below this, each higher order voltage follows an opposing temperature dependence to the corresponding linear response voltage. The inset graph in (b) is an expanded view of the main figure to show the increase in V^3_{offset} with decreasing temperature.

driven by temperature dependent changes to the V_2 and V^1_{offset} terms.

To better understand the factors contributing to the magnitude and temperature dependences of the thermal background voltages, we examine the linear response voltages V_2 and V^1_{offset} from which the higher order voltages arise. Figure 5.11 shows the temperature dependence of each for multiple LSVs with different electrode separations.

For every device V_2 is roughly a factor of ten larger than V^1_{offset}; primarily a result of the difference in the amount of heat generated by the Joule and Peltier effects. To illustrate this, we can estimate the heat generated from each effect at T = 200 K with the maximum applied current of I = 500 μA. For the Peltier heating $\dot{Q}_{\text{Peltier}} = TS_{\text{eff}}I$, which with a rough estimate of $S_{\text{eff}} = 2\mu V/K$ leads to $\dot{Q}_{\text{Peltier}} \approx 2$ μW. Joule heating will occur over the entire current path and although we could not measure the resistance of this path (due to a limited number of device contacts), earlier we stated that the primary source of Joule heating was the exposed region of the CoFe injector, so we can obtain a lower limit estimate of $\dot{Q}_{\text{Joule}} = I^2R_{\text{CoFe}}$ with $R_{\text{CoFe}} \approx 20\ \Omega$ as $\dot{Q}_{\text{Joule}} \approx 12$ μW. As $\dot{Q}_{\text{Joule}} \approx 10 * \dot{Q}_{\text{Peltier}}$, the difference in power dissipated by each mechanism is the primary contributor to the difference in magnitude of the two voltages.

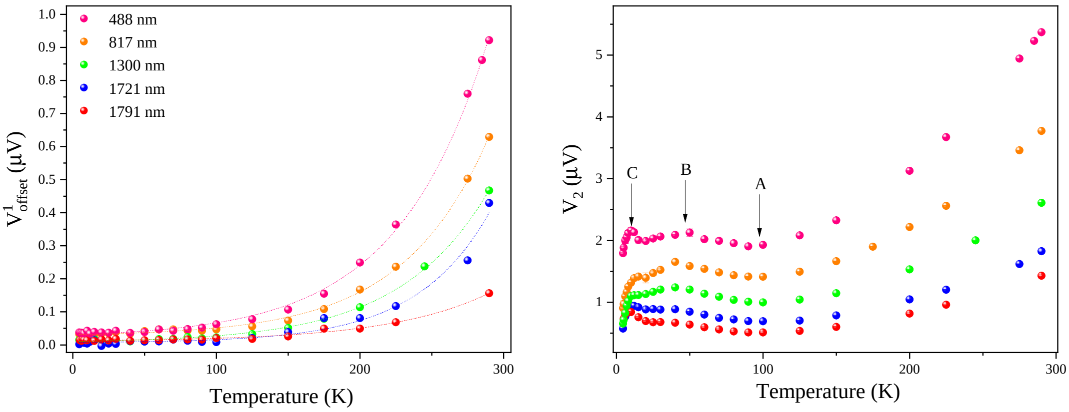

(a) (b)

Figure 5.11: The offset (a) and quadratic (b) voltages as a function of temperature for multiple LSVs with different electrode separations. As both the Joule and Peltier heat are generated in the injector circuit, both voltages decrease with increasing electrode separation. Below 100 K, the offset voltage is small and constant, whereas the quadratic voltage increases with decreasing temperature (point A) and exhibits two features (points B and C) at low temperatures.

In terms of the temperature dependent behaviour the data can be split into two regimes: high temperatures for $T > 100$ K; and, low temperatures for $T < 100$ K. At high temperatures both V_2 and V^1_{offset}, increase with temperature in a similar way. Below 100 K, V^1_{offset} slowly decreases towards a constant as T approaches 0 K. On the other hand, V_2 has a shallow minimum at 100 K that is common to all samples (A in Fig. 5.11(b)), increases to a broad peak at roughly 30 K (B in Fig. 5.11(b)) and a sharp drop below 10 K (C in Fig. 5.11(b)). To understand the evolution of each thermal voltage with temperature we have to consider:

1. The amount of heat generated, given by $\dot{Q}_{\text{Joule}} \approx I^2 R_{\text{CoFe}}$ or $\dot{Q}_{\text{Peltier}} = T S_{\text{eff}} I$.
2. The efficiency of heat transport into the SiO_2 substrate, determined by the thermal interface conductance (h).
3. The efficiency of thermal conduction along the Cu channel, determined by k_{Cu}.
4. The efficiency of heat detection, determined by the effective Seebeck coefficient of the interface ($S_{\text{eff}} = S_{\text{Cu}} - S_{\text{CoFe}}$).

In most metals, the magnitude of S linearly increases at high temperatures following the Mott electron diffusion contribution [7, 8, 175]. In the linear response regime, as is the case at high temperatures, the Seebeck and Peltier coefficients are related through the Thomson-Onsager reciprocity relation $\Pi = \mathrm{ST}$ [47, 176]. Consequently, both the Peltier heat generated and detection efficiency increase with temperature leading to an increase in $\mathrm{V}^1_{\mathrm{offset}}$. Similarly, Joule heating increases with temperature (as the resistance of the Cu and CoFe increases) as does the detection efficiency, leading to a rise in V_2 with temperature. The origin of the differences between the two thermal voltages at low temperatures is not so clear. Most thermopowers tend toward zero as the temperature reduces, so both the detection efficiency and Peltier heat will become very small. To some extent this explains the very small, slowly decreasing $\mathrm{V}^1_{\mathrm{offset}}$ at low temperatures. The low temperature increase and non-linear behaviour of V_2 below 100 K is not so straightforward. In theory, the only difference between the Joule and Peltier induced voltages should be the amount of heat generated. The Joule heating is first decreasing and then constant at low temperatures, so cannot explain these features in V_2.

5.5 Thermal Model

To unravel this behaviour, we consider the length dependence of V_2 and V^1_{offset} and employ a simple analytical model developed in our recent work [4] on Py/Ag LSVs to describe the heat diffusion through the Ag channel. As demonstrated by Kasai et al. [167] the vast majority of heat transported to the detector that is picked up as a voltage occurs through the wire itself and not through the substrate. We can therefore consider conduction through the wire alone with the substrate acting as a heat sink. Considering a rectangular Cu element with length dx, width w and thickness t at some temperature T. The heat diffusing into the cell ($\dot{\text{Q}}_{\text{in}}$) will be equal to the heat diffusing into the SiO_2 substrate ($\dot{\text{Q}}_{\text{sub}}$) and the heat leaving the cell ($\dot{\text{Q}}_{\text{out}}$):

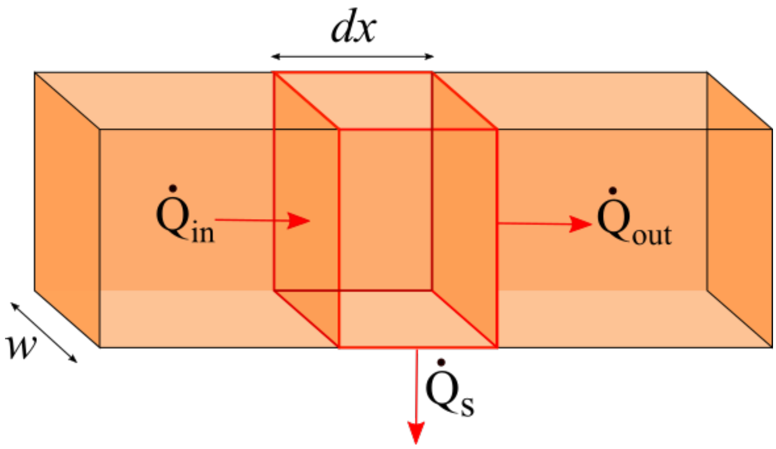

Figure 5.12: Schematic of the basis of the thermal model.

$$\dot{\text{Q}}_{\text{in}} = \dot{\text{Q}}_{\text{sub}} + \dot{\text{Q}}_{\text{out}} \tag{5.5}$$

Radiative heat losses are negligible from the top/sides of the Cu, as the temperature differences are small, so we consider only conduction and use Fourier's law:

$$\dot{\text{Q}}_{\text{in}}(\text{x}) = -2k\text{A}\frac{d\text{T}(\text{x})}{dx} \tag{5.6}$$

where, $k = \text{k}_{\text{Cu}}$ and $\text{A}=wdx$ is the cross–sectional area of the Cu channel. A factor of 2 is required to account for heat diffusing in both directions along the Cu wire.

Diffusive heat flux across the wire/substrate interface may be written as: J=$h\nabla$T where ∇T is the temperature gradient across the interface and h is the thermal interface conductance between Cu/SiO$_2$ which dictates the efficacy with which heat crosses the interface. This can be rewritten as:

$$\dot{\mathrm{Q}}_{\mathrm{s}} = h(\mathrm{T} - \mathrm{T}_{\mathrm{s}})wdx \tag{5.7}$$

Stringent temperature stability criteria ensure that T$_{\mathrm{s}}$ only varies by a maximum of ±20 mK prior to a measurement, thus it can be assumed constant for any particular measurement temperature. Here, wdx is the area of conduction. The heat diffusing out of the cell $\dot{\mathrm{Q}}_{\mathrm{out}}$ can be written as:

$$\dot{\mathrm{Q}}_{\mathrm{out}} = \dot{\mathrm{Q}}_{\mathrm{in}}(x + dx) = \dot{\mathrm{Q}}_{\mathrm{in}} + \frac{d\dot{\mathrm{Q}}_{\mathrm{in}}}{dx}dx \tag{5.8}$$

Combining 5.6, 5.7 and 5.8 leads to:

$$\dot{\mathrm{Q}}_{\mathrm{in}} = h(\mathrm{T} - \mathrm{T}_{\mathrm{s}})wdx + (\dot{\mathrm{Q}}_{\mathrm{in}} + \frac{d\dot{\mathrm{Q}}_{\mathrm{in}}}{dx})dx \tag{5.9}$$

Differentiating 5.6 leads to $\frac{\mathrm{d}\dot{\mathrm{Q}}_{\mathrm{in}}}{dx} = -2k\mathrm{A}\frac{d^2\mathrm{T(x)}}{dx^2}$. So, 5.9 can be simplified to:

$$\frac{d^2\mathrm{T(x)}}{dx^2} - \frac{wh}{2k\mathrm{A}}(\mathrm{T} - \mathrm{T}_{\mathrm{S}}) = 0 \tag{5.10}$$

Defining $\mathrm{T}^{'} = \mathrm{T} - \mathrm{T}_{\mathrm{S}}$ and $\alpha^2 = \frac{wh}{2k\mathrm{A}} = \frac{h}{2kt}$ leads to:

$$\frac{d^2\mathrm{T}^{'}}{dx^2} - \alpha^2\mathrm{T}^{'} = 0 \tag{5.11}$$

$\frac{1}{\alpha}$ is the decay length of the temperature; determined by the ratio of k and h. The general solution to 5.11 is of the form: $\mathrm{T}^{'}(\mathrm{x}) = \mathrm{B}_1\mathrm{e}^{\alpha\mathrm{x}} + \mathrm{B}_2\mathrm{e}^{-\alpha\mathrm{x}}$. To solve we impose boundary conditions for our geometry: at the injector (x=0) $\mathrm{T} = \mathrm{T}_\mathrm{i}$, where T_i is the injector temperature; and, at x=∞ the temperature should return to the substrate temperature $\mathrm{T} = \mathrm{T}_\mathrm{s}$. This leads to:

$$\mathrm{T}(\mathrm{x}) = (\mathrm{T}_\mathrm{i} - \mathrm{T}_\mathrm{s})\mathrm{e}^{-\alpha\mathrm{x}} + \mathrm{T}_\mathrm{s} \tag{5.12}$$

From equation 5.12, the length dependent temperature decay can be fitted to extract the decay length $\frac{1}{\alpha}$ and obtain an estimate for either k_Cu and h. Prior to this, we convert each thermal voltage into an effective temperature T(x) using equation 5.2.

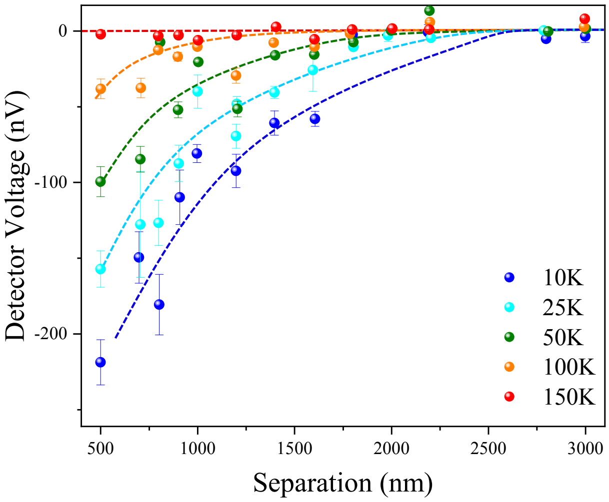

Figure 5.13: Detector voltages measured in control device composed of V only (dashed lines are guides to the eye). Data courtesy of Dr G. Stefanou [4].

To ensure that the thermal voltages measured are a consequence of thermal gradients within the LSV itself and not from other bimetallic junctions in the measurement circuit (i.e. where the Cu channel meets the Au/Cr inner contacts), Dr G. Stefanou fabricated LSVs composed entirely of V with the existing Au/Cr contacts (identical to those in this study). In this instance, no Peltier or Seebeck effects should arise in the device itself as it is composed of a single material and any voltages measured at the detector are a consequence of thermal effects arising elsewhere in the measurement circuit. The resulting detector voltage at various electrode separations and measurement temperatures is shown in Figure 5.13; the largest signal observed at 10 K is only 240 nV which is much smaller than the µV signals we observed.

5.5.1 Fitting the Thermal Model

As the thermal decay length is given by $\alpha = \sqrt{\frac{\mathrm{h}}{2\mathrm{k}_{\mathrm{Cu}}\mathrm{t}_{\mathrm{Cu}}}}$, where both k_{Cu} and h are unknowns, an estimate of one is required. The total thermal conductivity is the sum of the phonon (k_{ph}) and electron (k_{e}) contributions. As the Cu wires considered here are low resistivity, the electronic contribution should be dominant and $\mathrm{k}_{\mathrm{e}} \approx \mathrm{k}_{\mathrm{Cu}}$. This allows for an estimation of k_{Cu} from the measured electrical conductivity ($\sigma = \frac{1}{\rho}$) through the Wiedemann-Franz law: $\mathrm{k} = \sigma \mathrm{LT}$, where L is the Lorenz number and T is the absolute temperature. As the Sommerfield value, which assumes purely elastic scattering in a free electron metal, of $\mathrm{L}_0 = 2.44\mathrm{x}10^{-8}\ \mathrm{V}^2/\mathrm{K}^2$ is almost certainly inaccurate for the temperature range we are interested in, equation 2.26 (see Chapter 2) was used to calculate a temperature dependent Lorenz number. Theoretically, the use of this formula should be reasonable for Cu due to its highly spherical Fermi surface (apart from the ‘necks’). The only comparison between $\mathrm{L}_{\mathrm{theory}}$ (calculated from equation 2.26) and an experimentally obtained Lorenz number ($\mathrm{L}_{\mathrm{exp}}$) in 75 nm thick Cu films found that $\mathrm{L}_{\mathrm{exp}} > \mathrm{L}_{\mathrm{theory}}$ for temperatures between 75 and 200 K; suggesting a larger than anticipated phonon contribution [100]. This is likely due to the large residual resistivity in the films ($\rho_0 = 4.48\ \mu\Omega\mathrm{cm}$), as strong scattering from disorder can reduce the electronic contribution. Previous studies of Cu thin films with resistivities closer to those in this work have observed that k_{ph} is in fact small; quoting values between 6-10% of the total [177–179]. Therefore, we should obtain a reasonable estimation of k_{Cu} from equation 2.26.

To calculate L(T), the Debye temperature (Θ_{D}), residual resistivity (ρ_0) and electron-phonon coupling constant ($\mathrm{K}_{\mathrm{el-ph}}$) were extracted from fitting the Bloch-Grüneisen (BG) formula (see equation 4.1 in Chapter 4) to the average measured ρ_{Cu} (see Figure 4.2 in Chapter 4) with a fixed n=5. The fit yielded: $\Theta_{\mathrm{D}} = (286 \pm 1)$ K, ρ_0=$(1.251 \pm 0.003)\ \mu\Omega\mathrm{cm}$ and $\mathrm{K}_{\mathrm{el-ph}} = (10.75 \pm 0.02)\ \mu\Omega\mathrm{cm}$. Using the BG parameters, the Lorenz ratio (L/L_0) and temperature dependent Lorenz number (L(T)) were calculated using equation 2.26 and are depicted in Figure 5.14.

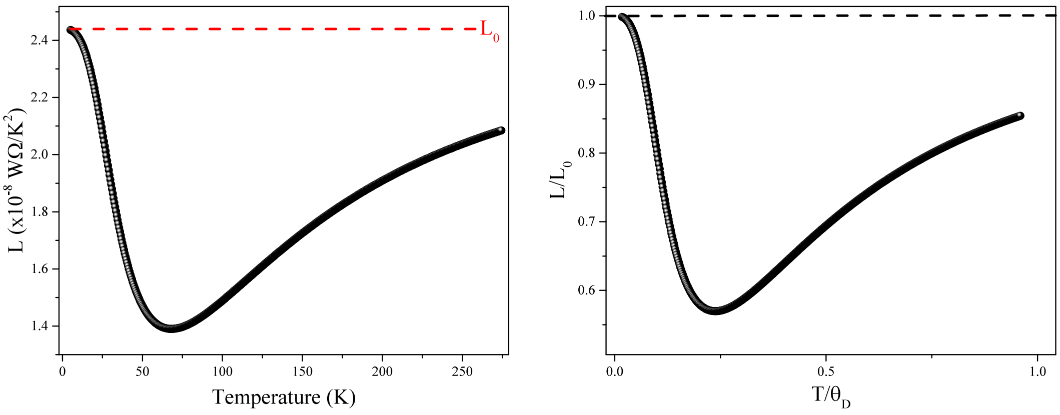

(a) (b)

Figure 5.14: (a) Temperature dependent Lorenz number calculated from a theoretical expression that takes into account phonon and impurity scattering in a free electron like metal. Parameters obtained from fitting the BG formula to the average Cu resistivity of the LSVs are used in the calculation, the values are given in the main text. (b) The ratio of the calculated Lorenz number to the Sommerfield value (L/L_0), which is equal to 1 when scattering is primarily elastic and falls below 1 due to inelastic scattering. As the Debye temperature of the Cu ($\Theta_D = (286 \pm 1)$ K) exceeds the highest measurement temperature, the theoretical value of L is reduced from L_0 at high temperatures.

The calculated Lorenz number shows the expected behaviour for a relatively pure metal. At the lowest temperatures ($T < 5$ K), where elastic scattering from impurities/defects dominates, L is equal to L_0. As the temperature increases, L is reduced from L_0 due to inelastic electron-phonon scattering which degrades thermal currents more than electrical currents. The competition between impurity/defect and phonon scattering leads to a minimum at $\frac{T}{\theta_D} = 0.23$. The depth of this minimum is known to depend on the purity of the material, which can be inferred from the ratio $\frac{\rho_0}{K_{el-ph}}$; a ratio less than 0.02 is typical for high purity bulk materials [180]. In this case, $\frac{\rho_0}{K_{el-ph}} \approx 0.116$ with a minimum value of $\frac{L}{L_0} \approx 0.6$. At high temperatures, there are numerous large wave-vector phonons capable of wide angle scattering that degrades both thermal and electrical currents equally, and L should return to L_0. However, at 275 K the calculated Lorenz number is reduced from L_0 ($\frac{L}{L_0} \approx 0.85$). This reduction is a consequence of inelastic scattering and is frequently observed in bulk Cu given that Θ_D exceeds room temperature; and, more recently in nanowires the reduction was attributed to dislocations [181]. Using our estimate of L, k_{Cu} was calculated as $k_{Cu} = \frac{L(T)T}{\rho_{Cu}(T)}$; the result is shown in Figure 5.15.

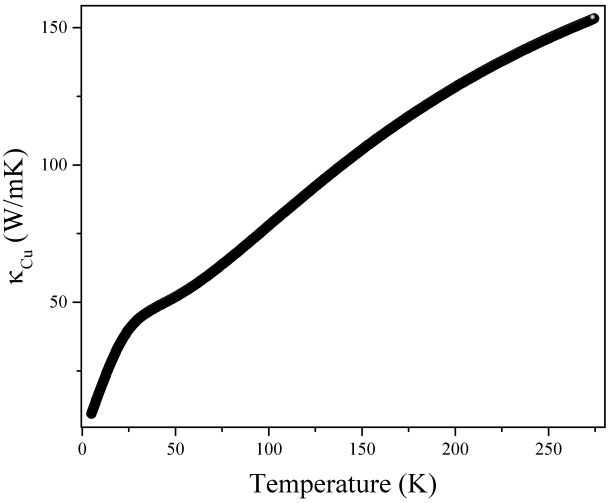

Figure 5.15: Estimate of the Cu thermal conductivity used to fit the thermal model; calculated using the Wiedemann-Franz law with the average Cu resistivity and theoretical Lorenz number.

Compared to bulk Cu, where $k_{Cu} \approx 401$ W/mK at 300 K, our estimate of k_{Cu} is reduced to ≈ 155 W/mK at 290 K. This reduction is comparable to actual measurements of k_{Cu} in a 75 nm Cu thin film [100] and in thickness dependent studies of Cu thin films [112, 175, 177, 182, 183]. The temperature dependence of k_{Cu} is completely different to bulk samples which tend to have a distinctive shape: a roughly constant (or increasing with reducing temperature) high temperature regime, followed by a peak around $\frac{\Theta_D}{5}$ and a final linear decrease at low temperatures where impurity scattering dominates. Here, our estimated k_{Cu} falls by 67% upon cooling from 275 to 50 K. Similar behaviour has been observed experimentally in Ag [136] and Ni [182] nanowires, Au [184] and Cu [100] thin films and other nanostructures [185]. Again, this is a result of an increase in disorder (due to the reduced dimensions) which results in a significant contribution from structural scattering in addition to phonons at high temperatures. These additional defect scattering contributions also suppress the peak (at T $\approx$ 40 K) to more of a point of inflection (in bulk the peak is of the order of $\approx 10^3$), as is often observed experimentally for non–bulk samples [180].

Thermopowers

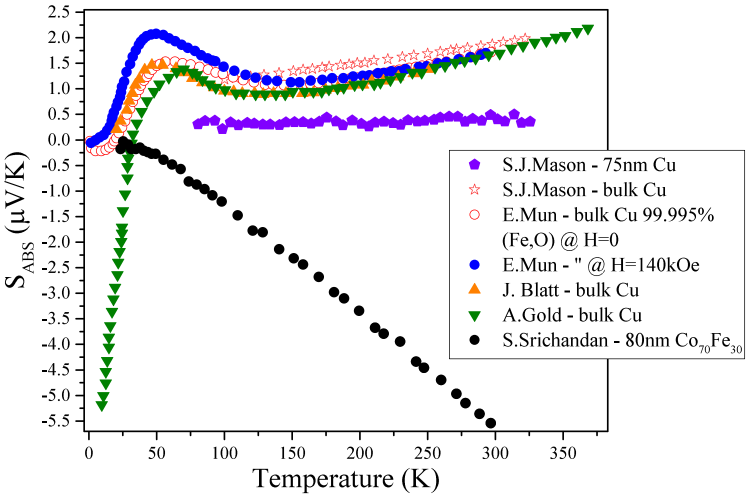

Figure 5.16: Summary of measured Seebeck coefficients for CoFe and Cu samples from the literature. References: S. J. Mason [5]; E. Mun [6]; J. Blatt [7]; A. Gold [8]; S. Srichandan [9]. Bulk Cu has been studied quite extensively and different samples tend to behave comparably in the high temperature linear region (T>100 K). Below this, however, the behaviour is diverse and heavily dependent on the impurity content of the sample. In particular, the Kondo impurities Fe and Co lead to giant negative thermopower peaks around T_K [8] - sometimes of the order of a few tens of microvolts. This phenomenon is demonstrated by the data sets from A. Gold (green triangles) and E. Mun (red open circles), which are from Cu with traces of Fe impurities (high and low concentrations respectively).

To fit the thermal model, we also require initial values of S_{Cu} and S_{CoFe} to convert the measured thermal voltages into temperatures. Finding a reasonable initial value is problematic, as even for bulk samples the exact magnitude and temperature dependence of S can be incredibly sensitive to growth conditions, oxidation, impurity content, roughness and other factors [5, 186]. Additionally, a growing body of thermopower measurements on nanoscale samples generally suggest that S can be greatly modified by the increase in defects, strain, grain boundaries and surfaces; in addition to classical size effects that become increasingly important as the dimensions approach the electronic mean free path [5, 187, 188]. A sample of the literature data for S_{Cu} is summarised in Figure 5.16, along with the only measurement of an 80 nm thick evaporated thin film of our particular $Co_{70}Fe_{30}$ alloy from [9]. Clearly, given the sparse data avaliable for S_{CoFe} and the multiplicity of possible variations in S_{Cu} without in situ measurements for our particular samples, the overall magnitude and temperature dependence of both are highly uncertain. Provided that the thermal diffusion length is dependent on the length scale over which the temperature decays - not the overall magnitude - it is insensistive to the uncertainty in S_{eff}. As the converted temperature is determined by the ratio $\frac{V_{th}}{S_{eff}}$, the larger our input S_{eff}, the smaller the converted temperature. Therefore, the least trustworthy aspects of the forthcoming analysis will be the predicted device temperatures which depend heavily on the input S_{eff}.

5.5.2 Fitting Results

The length dependence of V_2 and V^1_{offset} were fitted separately to extract characteristic decay lengths for each. To ensure that the length dependent parameters extracted were insensitive to the input S_{eff} two fits were performed: fit 1 using S_{CoFe} from [9] and a bulk like S_{Cu} from [7]; and, fit 2 where S_{Cu} was reduced by $\sim 75\%$ to match the magnitude of the only thin film 75 nm Cu sample (S.J. Mason et al. in purple in Figure 5.16). At low temperatures, where no data was avaliable, the thermopowers were extrapolated to zero. Having converted the thermal voltages into effective temperatures using the initial S_{eff}, the spatial decay was fitted to equation 5.12 with k_{Cu} fixed (to the estimate in Figure 5.15), and h and T_i left as free fitting parameters. T_i was constrained to a range of reasonable values which allowed S_{eff} to be adjusted during each fit; the input values of S_{eff} and those returned by the fitting procedure are depicted in Figure 5.16(d) as the black lines and coloured data points respectively.

In the linear response regime ($T > 20$ K), the model accounts for the length dependence of V_2 incredibly well; a few example fits are depicted in Figure 5.17(b-d). The extracted thermal conductance (h) of the Cu/SiO_2 interface and characteristic thermal diffusion length extracted from the fits to V_2 in the linear regime are depicted in Figure 5.18(a) and (b) respectively. Both h and the thermal diffusion lengths extracted from fit 1 (bulk like S_{Cu}) and fit 2 (thin film like S_{Cu}) are identical. At 290 K, the fit returns a thermal interface conductance of $h \approx 35$ $\mathrm{MWm^{-2}K^{-1}}$ which falls well within the $10 - 100$ $\mathrm{MWm^{-2}K^{-1}}$ range of measured metallic/dielectric interface conductance at room temperature [189–192]. Thermal transport across the Cu/SiO_2 interface will be mediated by phonons and is usually approximated by a diffuse mismatch model (DMM) that predicts a temperature dependence of $h \propto T^{-3}$ [189], which our h is consistent with. This is good evidence our estimation of k_{Cu} was reasonable. Between 290 and 100 K, the V_2 thermal diffusion length is roughly constant at 1100 nm, below which it starts to increase. As the thermal diffusion length is proportional to $\sqrt{\frac{k_{Cu}}{h}}$, its behaviour is determined by the competition between the efficacy of heat flow into the substrate and along the Cu channel; determined by h and k_{Cu} respectively. Below 100 K, h is rapidly declining, heat transfer into the substrate is increasingly limited and more heat is forced to diffuse within the device. This, rather than the slower decrease in k_{Cu}, is the dominant factor leading to a rise in the thermal diffusion length and the increase in V_2 (point A in Figure 5.11(b)) at 100 K.

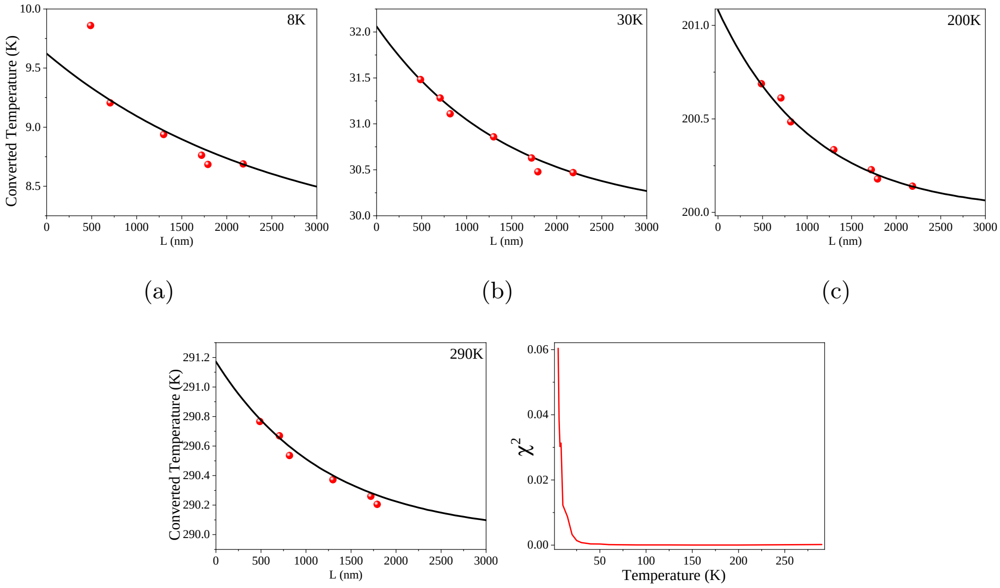

(a) (b) (c)

(d) (e)

Figure 5.17: Fits to the thermal model for the Joule induced voltage (V_2) at four temperatures (a-d) and goodness of fit parameter χ^2 as a function of temperature (e).

The tenfold reduction in h upon cooling to 20 K also explains why the device re-

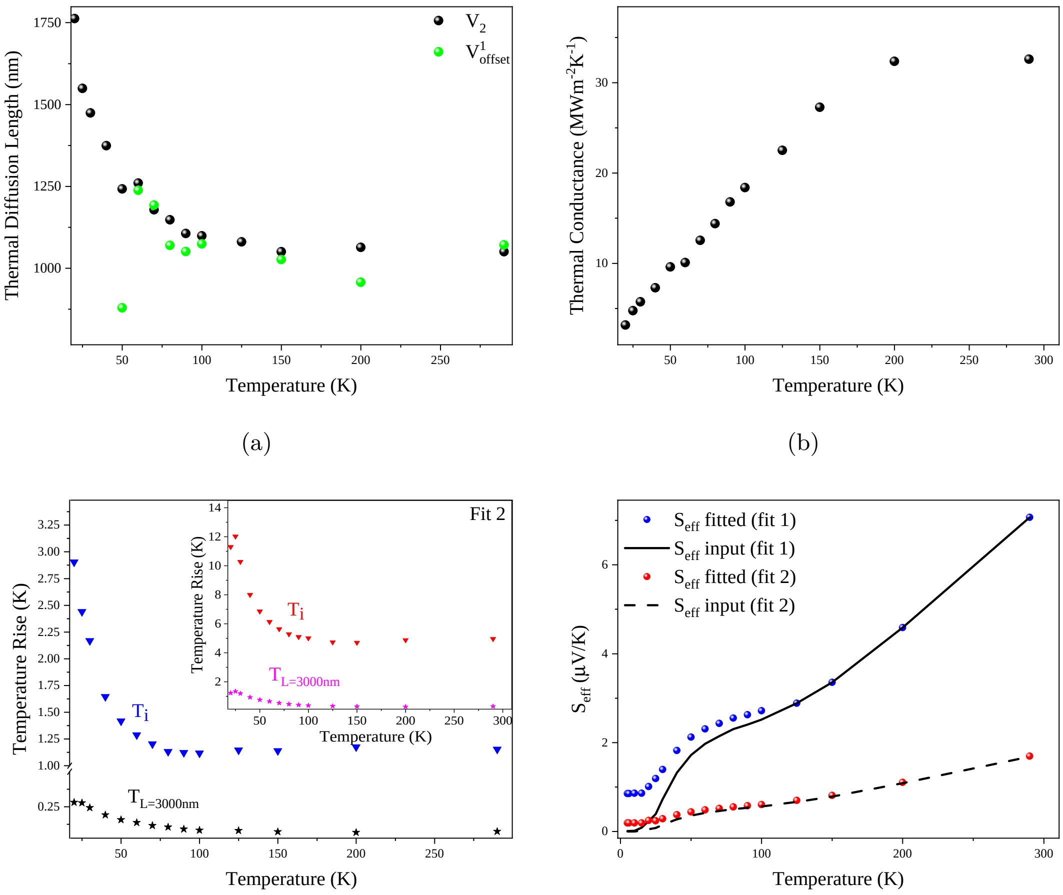

(a)

(b)

(c)

(d)

Figure 5.18: (a) Thermal diffusion lengths extracted from fitting the Joule (V_2) and Peltier (V^1_{offset}) induced thermal voltages. (b) Extracted thermal conductance of the Cu/SiO$_2$ interface. (c) Predicted temperature rise at the injector (T_i) and a position 3000 nm along the Cu ($T_{L=3000nm}$). The main figure depicts the predicted temperatures for fit 1, which used a bulk like S_{eff}, and the inset depicts the predicted temperatures for fit 2, with a thin film like S_{eff}. (d) Input values of S_{eff} and those returned by the fit: for fit 1, the input values of S_{eff} are the black solid lines and the fit values are in blue; and, for fit 2, the input values are the dashed black lines and those returned by the fit are in red.

sponses become non-linear. Although at low temperatures the power dissipated by Joule heating is constant (≈10.8 μW), the thermal interface conductance is very low

(≈ 3 MWm^{-2}K^{-1}) and will continue to fall as T→0 K. The dramatic reduction of heat flow into the substrate exacerbates thermal gradients within the devices; leading to the emergence of higher order voltage responses as the spin and thermal coefficients change with temperature. This is also reflected in the predicted temperature rise depicted in Figure 5.18(c). As stated earlier, the exact magnitude of these temperature increases are uncertain provided we do not have in situ measurements of the thermopowers of our nanoscale device elements. However, the general trend supports our other observations; the device temperature increases significantly as the measurement temperature decreases due to limited heat flow into the substrate.

With the onset of significant device heating and the transition into the non-linear regime our model fails to fit $V_2(L)$; this is illustrated by the goodness of fit parameter χ^2 calculated from each fit in Figure 5.17(e). Figure 5.17(a) shows the length dependence of V_2 at 8 K, from which one can observe that the shortest separation has increased significantly compared to the others. As stated earlier, the onset of the higher order voltages suggests that one or more of the thermoelectric parameters which combine to form the quadratic voltage (k_{Cu}, $\rho_{Cu/CoFe}$, S_{eff} and h) are changing as the local temperature varies $\propto I^2$. The model we have used here is limited in so far as we have assumed constant values for each measurement temperature. Obviously, if Joule heating in the injector circuit is generating temperature dependent changes in any of these parameters the degree to which it does so will depend on the electrode separation.

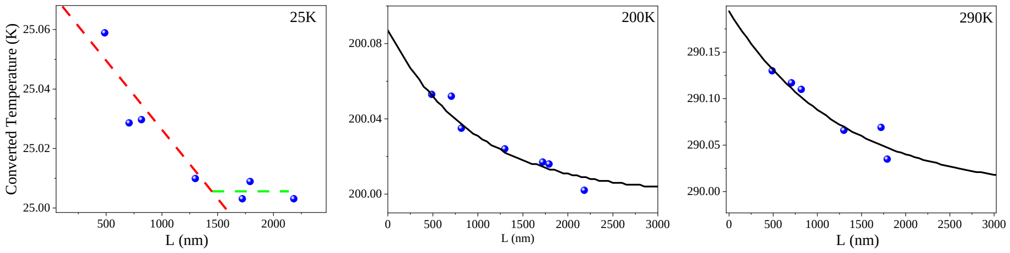

(a) (b) (c)

Figure 5.19: Fits to the thermal model for the Peltier induced voltage (V^1_{offset}) at three temperatures. At high temperatures (b-c), the decay is exponential and fits well to the model. (a) At 25 K, the decay is roughly linear down to 1500 nm and constant above this (the dashed red and green lines are guides to the eye).

The diffusion of Peltier and Joule heat through the devices should be driven by the same processes and the thermal diffusion lengths for V_2 and V^1_{offset} should be equal. As shown in Figure 5.18(a), this is true from room temperature down to about 60 K; below which V^1_{offset} diminishes on a very short length scale and is no longer exponential. This deviation from the expected exponential behaviour occurs at a much higher temperature than the 20 K onset of the non-linear response regime. As shown in Figure 5.19(a), V^1_{offset} decays almost linearly down to ~ 1500 nm. One interpretation of this is that Peltier heat loss into the substrate is negligible, which would lead to the solution of equation 5.12 being $\mathrm{T(x)} = (\frac{\mathrm{Ts}-\mathrm{T_i}}{\mathrm{L}})\mathrm{x} + \mathrm{T_i}$. Exactly why this happens is difficult to say, but it could indicate that heat transport from the sample into the substrate has become quasi-ballistic. A transition from diffusive to ballistic heat transport will occur when the mean free path of a heat carrier is comparable to the sample dimensions. Transport within the Cu never quite reaches the ballistic regime, as the electronic mean free path saturates at 50 nm (about half the width of the wire) at 5 K. In the SiO_2 substrate, kinetic theory predicts a phonon mean free path of Λ=45 nm at 10 K [193]. However, this is an average for the entire phonon distribution and does not specify which phonons are actively participating in thermal conduction [194]. Recent reports have indicated that phonons with $\Lambda >$100 nm can be responsible for almost half the heat conduction in amorphous Si at room temperature [195]. Therefore, it is possible that the mean free path of the phonons in the substrate is comparable to the ~ 100 nm Cu wire width around 60 K and the heat transfer into the substrate is entering the quasi-ballistic regime. The reduced thermal pathways avaliable for heat transfer into the substrate will reduce h, as we have observed [196]. As the Peltier heat is generated only at the $\mathrm{CoFe_1}$/Cu interface (that is small and not thermally well connected to the substrate), whereas Joule heat is produced over the entire injection current path (a comparatively large area well connected to the substrate) this reduction in interface conductance from ballistic transport will affect the Peltier heat much more significantly than the Joule heat. Even though very little Peltier heat is transferred into the substrate at low temperatures, the Peltier heat generated is so small and rapidly declining that V^1_{offset} does not increase. In contrast, the more considerable Joule heat is forced to diffuse within the device leading to an increase in V_2. Confirming this, however, would require further work.

As our model was not valid below 20 K, the origin of the low temperature features in V_2, namely: the broad peak at 30 K, sharp peak at 10 K and rapid decline below

10 K are not clear. For the latter, although the onset of quasi-ballistic heat transport would suggest that more heat is forced to diffuse within the device as the temperature decreases and V_2 would therefore continue to rise, this is hinged upon the assumption that the temperature of the CoFe detector (T_p) is still equal to the substrate temperature (T_s). When h is very low this assumption may no longer be valid and $T_p > T_s$, which would reduce the temperature gradient between the Cu channel and CoFe detector thus the Seebeck voltage measured. This could explain the rapid decline below 10 K, which occurs in every device at the same temperature. The other two features vary in magnitude and position from device to device. We suspect that these are a consequence of non-linear behaviour in S_{Cu} or k_{Cu} as both are very sensitive to the exact dimensions, impurity content and microstructure of each Cu channel [5, 197, 198]. In particular, the role of Kondo impurities in the thermal response of LSVs has not yet been investigated. It is well known that Kondo scattering from Fe leads to a large negative peak in S_{Cu} close to T_K and a positive peak in the electronic specific heat around $\sim \frac{1}{3}T_K$ [92, 93, 153], suspiciously close to the features observed at 10 K.

5.6 Conclusions

In summary, the thermal effects that arise during non-local measurements of CoFe/Cu LSVs were investigated. Thermal background signals arose from the Peltier effect at the injecting interface and Joule heating in the path of the injection current; both of which were detected through the Seebeck effect at the detecting interface. The temperature dependences of the Joule (V_2) and Peltier (V^1_{offset}) induced voltages were similar whilst $T > 100$ K; both increasing with temperature following the rise in heat generated by each effect and the detection efficiency. At low temperatures, V^1_{offset} was small and slowly decreasing, whereas V_2 increased below 100 K and exhibited a number of low temperature non-linear features. The length dependence of each thermal voltage was fitted using a simple model based on Fourier's law to extract the thermal conductance of the Cu/SiO$_2$ interface (h) and the characteristic thermal diffusion lengths. The limiting factor for heat flow within the devices was shown to be the thermal interface conductance which decreased from roughly 35 $MWm^{-2}K^{-1}$ at room temperature to 3 $MWm^{-2}K^{-1}$ at 20 K. Below 20 K, where heat flow into the substrate was greatly reduced, Joule heating induced temperature changes were large enough to change the thermal and spin dependent parameters $\propto I^2$ during a measurement and higher order voltage responses arose. The simple model could not fit the spatial dependence of V_2 once the device response became non-linear; we suspect as a result of the temperature dependent changes in k_{Cu} or S_{eff} varying with electrode separation. The length dependent behaviour of V^1_{offset} was significantly different to V_2 once $T < 60$ K. A transition from an exponential to almost linear decay occurred, which implied that Peltier heat loss into the substrate was negligible. We suggested that the phonon mean free path in the SiO_2 substrate could be comparable to the device dimensions ~ 100 nm at 60 K and there may be a transition from diffusive to quasi-ballistic heat transport into the substrate. This ballistic transition manifested differently in V_2 and V^1_{offset} given the differences in the areas of heat generation and power dissipated from each heat source. This could explain why V_2 increases below 100 K as the reduced pathways for heat transfer into the substrate ensure that more heat is reaching the detector than at higher temperatures.

Chapter 6

Spin Absorption

6.1 Introduction

The spin diffusion length is the characteristic length scale over which a non-equilibrium spin population persists. Consequently, it is a key parameter in the analysis of many spin transport and relaxation phenomena. Spin diffusion lengths of non-magnetic (NM) metals have been studied extensively through gap-dependent lateral spin valve (LSV) measurements [12, 27, 31, 55, 78, 84]. Measurements of the spin diffusion lengths of ferromagnets (λ_{FM}), however, are relatively scarce. Typical ferromagnetic spin diffusion lengths are well below 100 nm [15, 55, 71, 154, 199, 200], which negates the use of conventional gap-dependent measurement techniques. The comparative dearth of λ_{FM} measurements presents an obvious issue for spintronic research, especially the study of LSVs where the spin polarisation (α_{FM}) extracted from fitting the spatial decay of the spin signal ($\Delta \mathrm{R_S}$) is coupled to λ_{FM}. Usually, an empirical relationship that relates the resistivity (ρ_{FM}) and spin diffusion length is employed; specifically, $\lambda_{\mathrm{FM}}(\mathrm{T}) = \frac{\lambda_{\mathrm{FM}}(4.2\mathrm{K})\rho_{\mathrm{FM}}(4.2\mathrm{K})}{\rho_{\mathrm{FM}}(\mathrm{T})}$ [55], where $\rho_{4.2\mathrm{K}}\lambda_{4.2\mathrm{K}}$ is taken from the literature. One issue with this approach is that most published values of $\rho_{4.2\mathrm{K}}\lambda_{4.2\mathrm{K}}$ are derived from sputtered thin films with very different dominant defect types, dimensions and impurity contents to the ferromagnetic nanowires used in LSVs. Additionally, it assumes an inverse relationship between λ_{FM} and ρ_{FM} characteristic of Elliott-Yafet (EY) spin relaxation; not yet experimentally verified for most ferromagnets (FMs). Consequently, without an independent measurement of λ_{FM} a reliable α_{FM} cannot be determined. More broadly, verifying the dominant mechanisms of spin relaxation in FMs is important given their crucial role in many spintronic devices. Recent theoretical predictions from Berger [201] have suggested that the EY mechanism should be the dominant source of spin relaxation in certain metallic FMs; specifically, those which have no spin-up (or spin-down) 3d electrons at the Fermi energy such as the predominately Ni and Co based alloys, Py and CoFe, that are frequently used in spintronic devices. Testing the validity of this theory is vital to further our understanding of spin relaxation, but also from a practical point of view to allow for predictions of λ_{FM} to be made from ρ_{FM}, which is more straightforward to measure.

Until recently, measurements of λ_{FM} were performed through variations of current perpendicular to plane magnetoresistance (CPP-MR) techniques which, except for multilayered nanowire or nanopillar structures, are limited to low temperatures [15, 55, 154, 199, 200, 202–204]. Other methods include the inverse spin-Hall effect

[74, 75, 205, 206] and optical techniques [207]. Albeit some of the methods stated above can be performed at a range of temperatures all require varying the thickness of the FM layer. This can introduce unwanted variations in resistivity with thickness and in turn alter the spin diffusion length [208, 209]. A robust alternative is the spin absorption method, which can be performed at a range of temperatures without the need to vary the material thickness. A central floating wire, composed of the material of interest, is introduced between the FM electrodes of a regular LSV [11]. The approach relies on the concept of the spin resistance, which is defined as $\mathrm{R_S} = \frac{\rho\lambda_\mathrm{S}}{\mathrm{A}(1-\alpha^2)}$, where ρ is the element resistivity, α is the spin polarisation, λ_S is the spin diffusion length and A is the cross-sectional area of the element perpendicular to the spin current flow [11]. A device element with a low $\mathrm{R_S}$ is a preferred path for spin relaxation and acts as an efficient 'spin sink'. In the instance that the central wire has a low $\mathrm{R_S}$ compared to the transport channel, it absorbs some of the spin current and decreases the spin signal compared to a reference LSV. As the degree of absorption is related to $\mathrm{R_S}$, it is possible to extract the spin diffusion length of the central wire. The technique has proved effective to measure other short spin diffusion lengths such as those of the heavy metals Pt and Ta [71, 210–212], but measurements on FM metals are still in short supply. E. Sagasta et al. employed a spin absorption technique in Cu/Py devices fabricated in two steps to obtain $\lambda_\mathrm{Py}(\mathrm{T})$ and confirmed that the EY relationship predicted by Berger held [10]. G. Zhand et al. [71] expanded the range of absorbing FMs (also with a two-step fabrication process) to $\mathrm{Co_{60}Fe_{40}}$, $\mathrm{Ni_{81}Fe_{19}}$ and Co; but only at low and high temperatures. Whether or not the predictions of Berger apply to the Co based alloys is still yet to be determined.

In this chapter, the spin diffusion length (λ_CoFe) of two $\mathrm{Co_{70}Fe_{30}}$ absorption wires are determined from 5 to 250 K. We employ the spin absorption technique as in [71] and [10], but instead use a single-step shadow evaporation technique to avoid the need for interface cleaning. As highlighted by Pfeiffer et al. [107], two-step processes may introduce problems for spin absorption experiments. Through specialised buried interface-sensitive scanning electron microscopy (SEM), they identified regions of residual resist and inhomogeneous over–milled regions; the presence of which have no observable effect upon charge transport, but have a significant impact on the degree of spin absorption. Capturing the full temperature dependence of λ_CoFe allows us to examine the validity of the EY mechanism in this technologically relevant alloy.

6.2 Devices

Three different types of devices were fabricated for this work. Firstly, the degree of spin absorption by a CoFe wire, deduced from the suppression of the spin signal compared to a reference device without a wire, must be measured. To this end, two identical spin absorption devices (SADs) were fabricated (denoted absorber A and B) with an electrode separation of L = 600 nm and a 100 nm wide, 30 nm thick CoFe absorber at the centre of the Cu channel; an SEM image of absorber A is depicted in Figure 6.1. The reference device was a regular LSV that was geometrically identical to the SADs, just without the central absorbing wire.

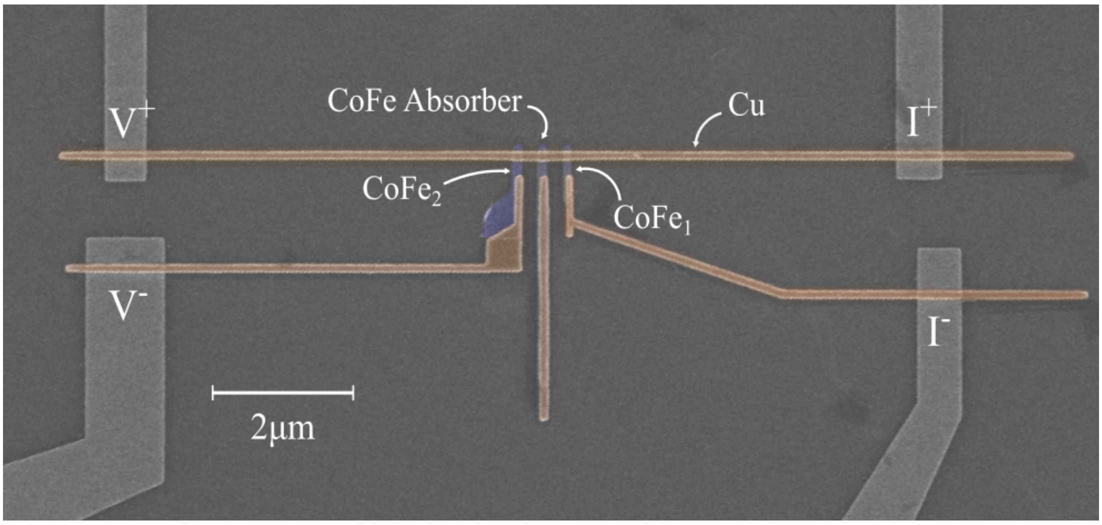

Figure 6.1: SEM image of one of the SADs (absorber A) in the non-local measurement scheme, where CoFe_1 is used as the injecting electrode and CoFe_2 is the detecting electrode. False colours indicate the materials Cu (orange) and CoFe (blue).

To obtain λ_{CoFe} from the degree of spin absorption measured, the key spintronic and charge transport parameters for the CoFe and Cu that feature in the 1D spin diffusion equations must be determined, namely: λ_{Cu}, α_{CoFe}, ρ_{Cu} and ρ_{CoFe}. The first three parameters can be obtained from regular LSV length dependent studies. Although other studies have used values from previous work [71], these parameters can vary with minute changes to the LSV dimensions, microstructure and impurity content [56, 81, 106]. Therefore, a set of CoFe(30 nm)/Cu(100 nm) LSVs with electrode separations (L) ranging from 300 nm to 3 µm were fabricated. All the SAD and LSV devices were fabricated on the same chip and deposited at the same time in order to maintain consistent material properties.

A shadow deposition method was used to ensure high quality transparent interfaces between the CoFe and Cu. In the first deposition step, both the CoFe electrodes and absorbing wires were evaporated at a 45° angle to the substrate. Following this, Cu was deposited normal to the substrate. Consequently, only part of the absorbing CoFe wire was exposed (blue region of central wire in Figure 6.1) and the remainder topped with Cu. As $\lambda_{\mathrm{CoFe}} < 20$ nm [55, 71, 154], the relevant region for spin relaxation lay close to the interface which was roughly 300 nm away from the region in contact with Cu. Therefore, it was assumed that this should not interfere with the spin absorption process at the interface.

Finally, ρ_{CoFe} could not be measured in situ given the geometry of each device. Therefore, three CoFe nanowires with $\mathrm{t}_{\mathrm{CoFe}} = 30$ nm and $\mathrm{w}_{\mathrm{CoFe}} = 100$ nm were fabricated and deposited in equivalent conditions to the SAD and LSV devices. An SEM image of one of these nanowires and the average resistivity of the set are depicted in Figure 6.2. Growth rates were 0.2 Å/s for the Cu and 0.1 Å/s for the CoFe.

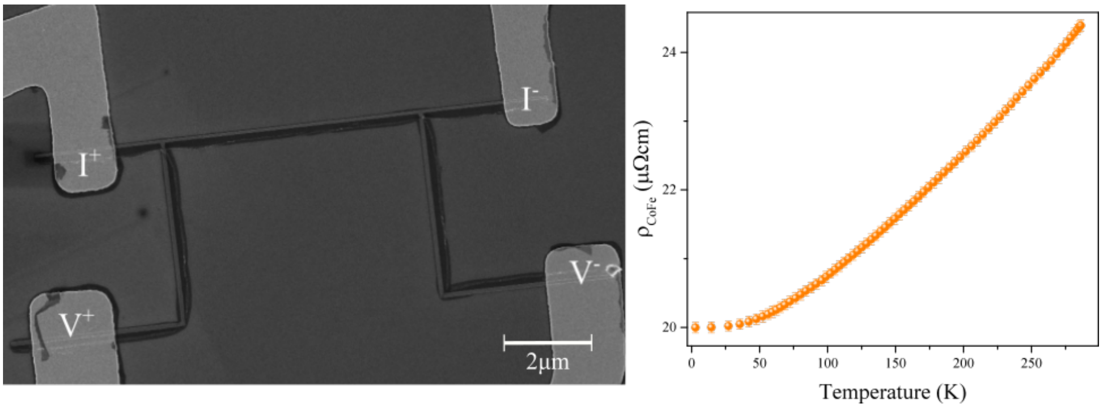

Figure 6.2: SEM image of one of three 30 nm thick, 100 nm wide CoFe nanowires (left) and the average resistivity of the three nanowires (right).

6.3 Spin Transport

6.3.1 Lateral Spin Valves

Seven LSVs with electrode separations between 300 nm and 1.2 µm were used to determine ρ_{Cu}, λ_{Cu} and α_{CoFe}. Local measurements were performed whilst cooling from 250 to 5 K to obtain the temperature dependence of the resistance of each Cu channel. From this, SEM measurements of the channel geometry were used to obtain the Cu resistivity and calculate an average value for the set, as depicted in Figure 6.3(a).

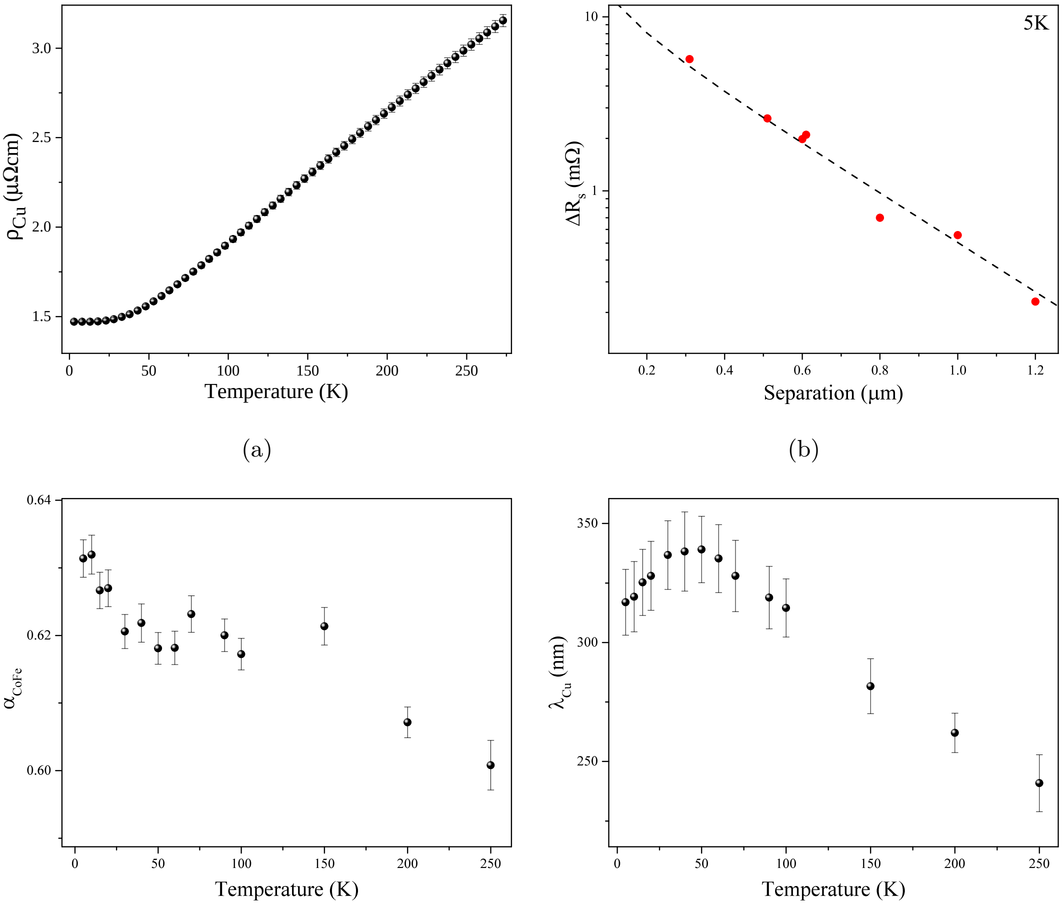

(a) (b)

(c) (d)

Figure 6.3: (a) Average resistivity as a function of temperature for the Cu transport channels. (b) The spatial decay of ΔR_S at 5 K, the dashed line is a fit to equation 2.15. Temperature dependence of α_{CoFe} (c) and λ_{Cu}(d) extracted from the fits to $\Delta R_S(L)$.

Following the procedure detailed in Chapter 4, the non-local voltage (V_{NL}) was measured as a function of applied magnetic field and temperature for each LSV. From V_{NL}, the linear voltage response (V_1) was extracted and normalised by the injection current (I) to obtain the linear coefficient ($R_1 = \frac{V_1}{I}$). As discussed in previous chapters, the spin signal (ΔR_S) can be obtained as the difference between R_1 in the parallel (P) and anti-parallel (AP) electrode magnetisation states. At each measurement temperature, the spatial decay of ΔR_S was fitted to equation 2.15 with a constant $\lambda_{CoFe} = 10$ nm for simplicity; an example fit at 5 K is depicted in Figure 6.3(b). The temperature dependence of the extracted values of λ_{Cu} and α_{CoFe} are shown in Figure 6.3(d) and (c) respectively. Of note, the values obtained for λ_{Cu} are all quite low due to contamination of the Cu channel from the electrode material. However, they are consistent with the values found in other $t_{CoFe} = 30$ nm LSVs in Chapter 4 and should not interfere with the degree of spin absorption.

6.3.2 Spin Absorption Devices

Three devices formed the basis of the spin absorption analysis - two identical SADs (absorber A and B) and a reference LSV. Again, non-local measurements were performed (schematic depicted in Figure 6.1) to obtain R_1 as a function of applied magnetic field and temperature for each device. Figure 6.4(a) shows R_1 as a function of applied magnetic field at 10 K for each SAD and the reference LSV. At low temperatures, where the Peltier contribution to R_1 is negligible, the linear component is entirely due to the spin accumulation at the detecting interface. There is a clear suppression of R_1 in both the P and AP states for both SADs compared to the reference LSV, demonstrating that the CoFe absorber wires are acting as spin sinks and reducing the spin accumulation that reaches the detecting interface. Moreover, for both SADs, R_1 is suppressed equally ($\approx 56\%$) in the P and AP states. Therefore, the degree of spin absorption does not depend on the magnetic configuration of the CoFe electrodes nor the absorbing wire. This is expected, as all magnetisations and thus spin polarisations are collinear [74]. Consequently, the amount of spin absorption by the central CoFe wire is determined by its spin resistance $R_S = \frac{\rho_{CoFe}\lambda_{CoFe}}{A_{CoFe}(1-\alpha_{CoFe}^2)}$ (where A_{CoFe} is the interface area between the Cu channel and the CoFe absorber), which is independent of the magnetisation of the CoFe absorbing wire, the magnetisation state of the CoFe electrodes and the small magnetic fields applied.

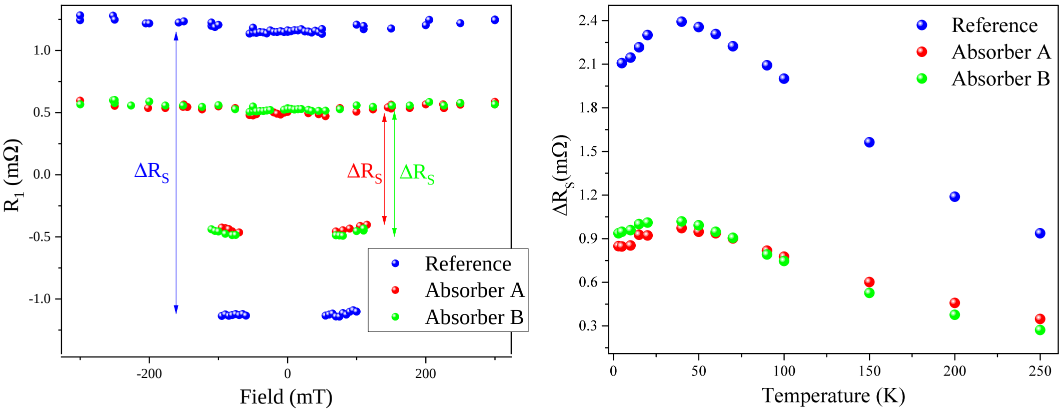

(a) (b)

Figure 6.4: (a) R_1 as a function of applied magnetic field at 10 K for the reference LSV (blue), absorber A (red) and absorber B (green). R_1 is positive in the P electrode state and negative in the AP state. The difference between R_1 in the P and AP states is the spin signal, ΔR_S. (b) Temperature dependence of ΔR_S for each device, which is lower in both absorber A and B compared to the reference LSV due to spin absorption by the central wires.

As indicated in the figure, the difference between R_1 in the P and AP electrode states is ΔR_S. Figure 6.4(b) shows the evolution of $\Delta R_S(T)$ for each of the devices. Compared to the reference LSV, the spin signal in each SAD is lower at all temperatures due to spin absorption by the central wires. All $\Delta R_S(T)$ have a non–monotonic temperature dependence with a peak at $T \approx 50$ K; reaching a maximum of $\Delta R_S \approx 2.4$ mΩ in the reference LSV and $\Delta R_S \approx 1.0$ mΩ in the SADs. Absorber A and B are two identical devices, so $\Delta R_S(T)$ should be the same. Indeed, the magnitude and temperature dependence of ΔR_S for each SAD are close with a maximum difference of only 0.1 mΩ at 5 K.

Extracting α_{CoFe} and λ_{CoFe}

Following the procedure outlined in [10], the ratio (η) of the spin signal in each SAD (ΔR_S^{abs}) to the spin signal in the reference LSV (ΔR_S^{ref}) was calculated as $\eta = \frac{\Delta R_S^{abs}}{\Delta R_S^{ref}}$. At each temperature, the calculated value of η and the values of ρ_{Cu}, α_{CoFe} and λ_{Cu} extracted from the LSV measurements, were substituted into equation 2.16 to obtain an estimate of λ_{CoFe}. Following this, the spatial decay of $\Delta\mathrm{R_S}$ was fitted once again to equation 2.15 using the new estimate of λ_{CoFe}, to yield new values of α_{CoFe} and λ_{Cu}. This process of substitution into equation 2.16 and refitting equation 2.15 was repeated until the parameters converged. The above procedure was followed to extract values of λ_{CoFe}, α_{CoFe} and λ_{Cu} for absorber A and B.

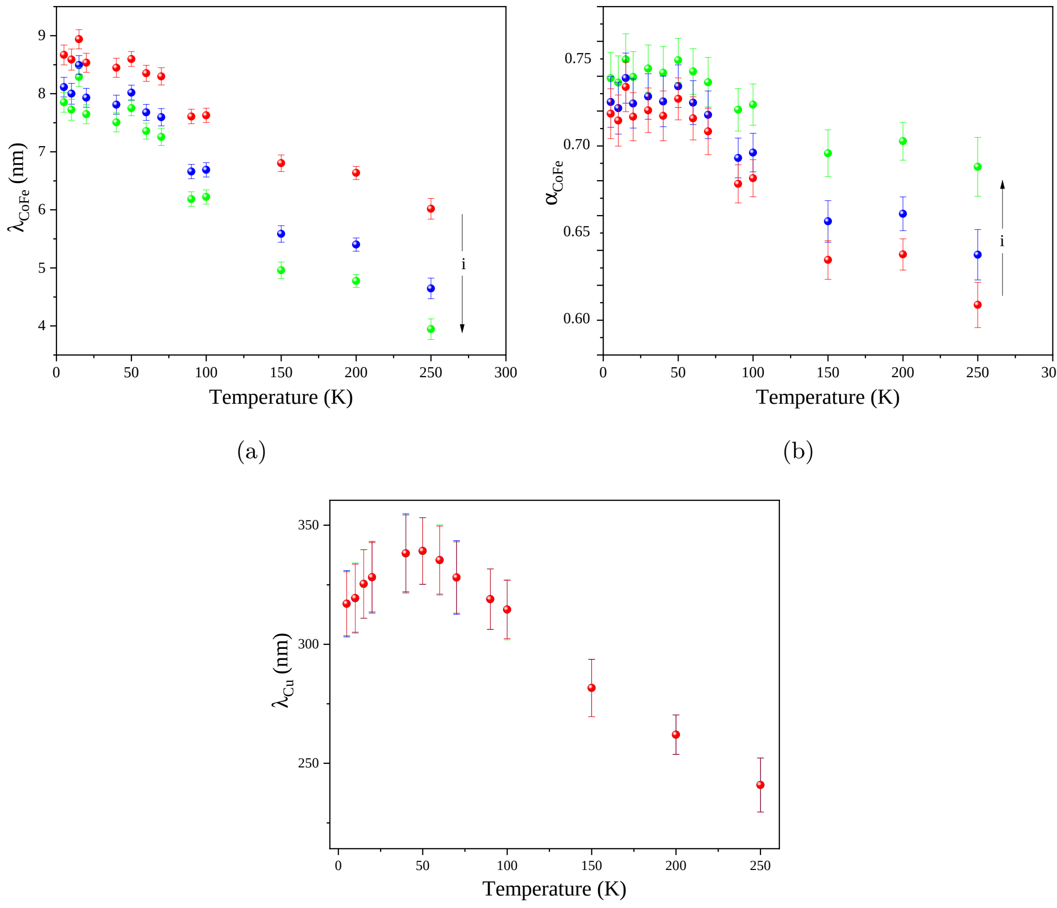

(a)

(b)

(c)

Figure 6.5: Absorber A: values of λ_{CoFe}(a), α_{CoFe}(b) and λ_{Cu}(c) extracted at three stages during the substitution and refitting procedure outlined in the text. The final values are depicted in green and the arrows (labelled i) denote the direction of the change in each parameter over the iteration process.

Figure 6.5 shows each parameter at three stages of the iteration process (one iteration here refers to one round of substitution into equation 2.16 and fitting of equation 2.15) for absorber A. As λ_{Cu} is determined by the length scale over which ΔR_S decays, not the overall magnitude, it does not change significantly over the iteration process. Given that the initial estimate of $\lambda_{\mathrm{CoFe}} = 10$ nm was quite high, λ_{CoFe} gradually decreases over the iteration process. This decrease in λ_{CoFe} leads to an increase in α_{CoFe}, as the product $\lambda_{\mathrm{CoFe}}\alpha_{\mathrm{CoFe}}$ determines the y-axis offset of the measured $\Delta R_S(L)$ curve.

The above process was repeated for absorber B leading to the results in Figure 6.6. Note that λ_{Cu} is not plotted as it is identical to that in Figure 6.5(c). As stated earlier, absorber A and B are two identically designed devices, which were fabricated alongside one another and deposited at the same time. In theory, therefore, the values of α_{CoFe} and λ_{CoFe} obtained from each device should be identical. The extracted values of λ_{CoFe} have similar temperature dependences but is slightly larger (≈ 1 nm) in absorber A. The overall magnitude of the extracted values of α_{CoFe} are comparable and decay in a similar fashion with increasing temperature above 50 K. At low temperatures, however, α_{CoFe} from absorber A is roughly constant, whereas α_{CoFe} from absorber B increases from 0.7 to 0.75. These slight differences suggest that there are variations between the devices despite the identical processing conditions.

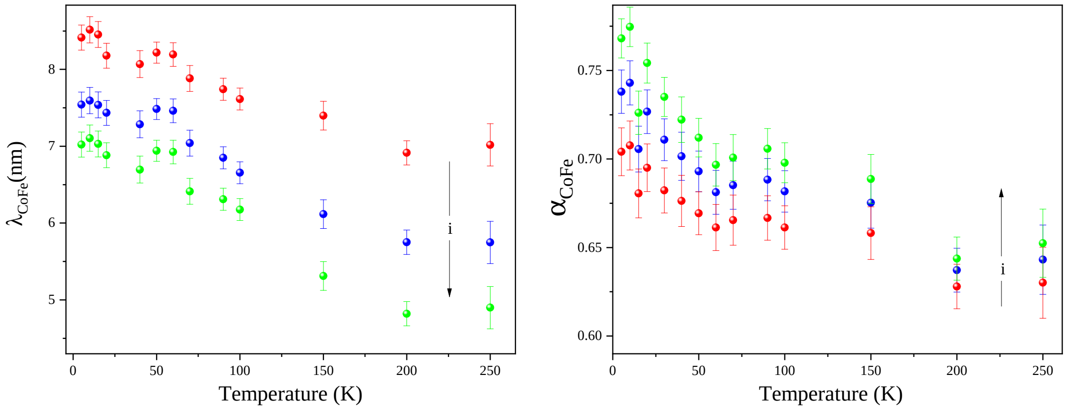

(a)

(b)

Figure 6.6: Absorber B: values of λ_{CoFe}(a) and α_{CoFe}(b) extracted at three stages during the substitution and refitting procedure outlined in the text. The final values are depicted in green and the arrows (labelled i) denote the direction of the change in each parameter over the iteration process.

Many factors could contribute to these differences, including variations in: the resistivity and spin diffusion lengths of each device element; the microstructure and defect concentrations at the CoFe/Cu interfaces; and, the device geometry. For the latter, the deposited thickness of the Cu and CoFe in each device were identical and the element widths were all within ±3 nm of one another. Moreover, the resistivity of the Cu transport channels were equivalent. As the EY mechanism governs spin relaxation in Cu [56, 78, 84, 85, 158], it can be assumed that the very similar Cu resistivities implies close Cu spin diffusion lengths in each device. This leaves the spin diffusion length and resistivity of each CoFe element, and the properties of the CoFe/Cu interfaces. Unfortunately, given the device geometries, the resistivity of each individual CoFe absorber and electrode cannot be measured. Slight variations in CoFe resistivity between the devices could lead to the variations observed. Additionally, the magnitude and temperature dependence of the spin polarisation (α_{FM}) extracted in LSV measurements is known to be sensitive to the local defect concentrations at the FM/NM interfaces [3, 98, 121]. In this instance, the observed differences in α_{CoFe} may arise due to variations in the microstructure and defect content of the CoFe/Cu interfaces between the two SADs. Variations in FM/NM interface properties between devices fabricated alongside one another have not yet been discussed in the literature. This is because in regular LSV measurements an average value of α_{FM} is extracted from a set of many LSVs, thus device to device variations are not observable. Additionally, in existing spin absorption measurements no two identical SADs are usually measured.

Averaging the final values of α_{CoFe} and λ_{CoFe} extracted from absorbers A and B yields the final results shown in Figure 6.7. The temperature dependence of λ_{CoFe} is roughly what would be expected from the EY mechanism. At low temperatures, where ρ_{CoFe} reaches its residual value, λ_{CoFe} saturates at a maximum of (7.4±0.6) nm at 5 K. Above 50 K, λ_{CoFe} decreases with temperature to a value of (4.4±0.7) nm at 250 K. Although noisy, the general trend of α_{CoFe} is to decay with temperature due to spin mixing within the CoFe. The temperature dependence of the spin polarisation was fitted to a Bloch law $\alpha = \alpha_0(1 - (\frac{\mathrm{T}}{\mathrm{T_C}})^{\frac{3}{2}})$, where α_0 is the intrinsic polarisation and $\mathrm{T_C}$ is the Curie temperature. The Bloch fit is depicted as the dashed black line in Figure 6.7 and yields α_0=0.736 ± 0.003 and $\mathrm{T_C} = 1070 \pm 60$ K. $\mathrm{T_C}$ is a little lower but comparable to that of bulk CoFe [165]. It is interesting that we do not observe a low temperature reduction in α_{CoFe}; as discussed in Chapter 4, this was proposed to be an inevitable feature of shadow deposited devices as a result of Kondo scattering from dilute interdiffused magnetic impurities (MIs) at the FM/NM interfaces [30, 97].

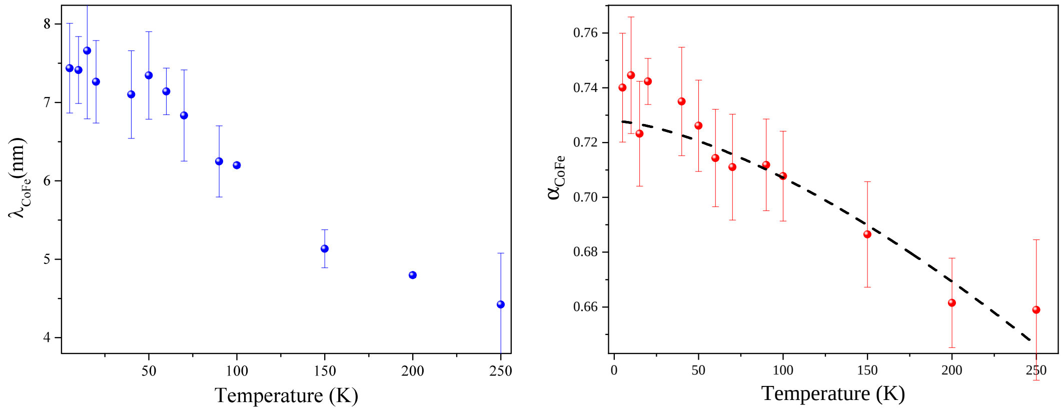

(a) (b)

Figure 6.7: Average λ_{CoFe} (a) and α_{CoFe} (b) calculated from the final values obtained from absorbers A and B. The dashed line in (b) is a fit to a Bloch law, demonstrating that the spin polarisation decays following the spin current polarisation of the CoFe and has no observable low temperature reduction from Kondo scattering at the CoFe/Cu interfaces.

Table 6.1 summarises measured and assumed values of α_{CoFe} and λ_{CoFe} from the literature; other close alloy compositions have been included as only one measurement of our particular composition exists. Note that for the LSV technique, the stated values of λ_{CoFe} are estimates and α_{CoFe} is directly dependent on their estimation. Overall, the average λ_{CoFe} falls within the published range of values of 4 to 12 nm. The spin polarisation of our $\mathrm{Co}_{70}\mathrm{Fe}_{30}$ is roughly 20% higher than values found in spin absorption measurements of $\mathrm{Co}_{60}\mathrm{Fe}_{40}$. This may indicate that ours is a more favourable alloy composition for high spin polarisations, as was previously observed in Giant Tunneling Magnetoresistance [45]. Alternatively, a two-step deposition method was used in [71], where the CoFe was exposed to atmosphere and resists prior to the non-magnetic metal deposition. Consequently, the higher spin polarisation in our case may be a result of the better quality transparent interfaces produced through a shadow depostion method.

The EY mechanism posits that $\lambda_{\mathrm{CoFe}} \propto \frac{1}{\rho_{\mathrm{CoFe}}}$, so the product $\lambda_{\mathrm{CoFe}}\rho_{\mathrm{CoFe}}$ should be a temperature independent constant. As shown in Figure 6.8, $\lambda_{\mathrm{CoFe}}\rho_{\mathrm{CoFe}}$ is constant below 100 K at 1.5 fΩm^2 and decreases only slightly with increasing temperature. Of note, the obtained values are twice that found in a thin film of $\mathrm{Co}_{70}\mathrm{Fe}_{30}$ (see Table

Alloy (Co:Fe)	**Technique**	**T(K)**	ρ_{CoFe} ($\mu\Omega$cm)	λ_{CoFe} **(nm)**	α_{CoFe}	**Group**
70:30	CPP	4.2	6.1±0.4	10.9±0.5	N/A± N/A	C.Ahn et al. [154]
60:40	SA	300	20±1	6.7±0.7	0.48±0.02	G.Zhand et al. [71]
60:40	SA	10	15.0±0.9	8.3±1.8	0.48±0.03	G.Zhand et al. [71]
60:40	LSV	300	23	11.1±0.1	0.45±0.05	G.Bridoux et al. [42]
84:16	LSV	300	20	10	0.2	S.Oki et al. [44]
70:30	SA	5	20.1±0.1	7.4±0.6	0.74±0.02	This work.
70:30	SA	250	23.8±0.1	4.4±0.7	0.658±0.03	This work.

Table 6.1: Summary of CoFe spin transport parameters from the literature. Values have been determined by current-perpendicular to plane (CPP), spin absorption (SA) and lateral spin valve (LSV) techniques.

6.1: C.Ahn et al.) which was approximately 0.6 fΩm^2 at 4.2 K [154]. However, in mesoscopic wires of $\mathrm{Co_{60}Fe_{40}}$ (see Table 6.1: G. Zhand et al.) also measured using spin absorption (SA), products of 1.46 fΩm^2 and 1.246 fΩm^2 at 300 K and 10 K were obtained; which are more comparable to our results.

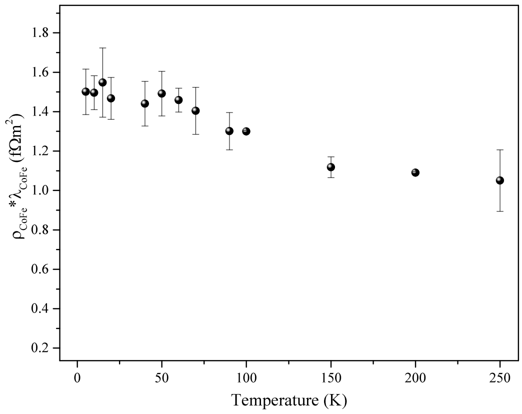

Figure 6.8: The product of the average spin diffusion length and resistivity for CoFe. Overall, the product varies only slightly with temperature suggesting that spin relaxation in our CoFe is dominated by the EY mechanism.

Previous reports have demonstrated a general linear correlation between $\frac{1}{\rho_{\mathrm{FM}}}$ and λ_{FM} for FM metals; with the exception of Co, where λ_{Co} is found to be anomalously long for a given ρ_{Co} [55]. In Figure 6.9, our data is plotted alongside extant literature data for CoFe (red), Py (blue) and Fe (green) taken from SA (star), LSV (triangle) and CPP (pentagon) techniques. There is an overall linear trend, except for the lowest resistivity samples from CPP measurements (which fall below the trend and have lower λ_{FM} than expected) and the estimated values in LSVs (which systemically tend to overestimate λ_{FM}). There is particularly good agreement to the linear trend between SA measurements of Py and CoFe. Similar scaling between $\frac{\lambda_{\text{Co}_{91}\text{Fe}_9}}{\lambda_{\text{Py}}}$ and $\frac{\rho_{\text{Py}}}{\rho_{\text{Co}_{91}\text{Fe}_9}}$ was observed in CPP measurements [200]. Interestingly, there is some incompatibility between CPP and SA techniques; the spin diffusion lengths determined by SA are longer than expected from a linear fit to the CPP results. This may be a consequence of the different dominant defect types in samples measured in SA, which tend to be electron beam evaporated nanowires, compared to the sputtered thin films in CPP techniques. Certain defects can induce strong resistive scattering but weak spin-scattering and vice versa [82].

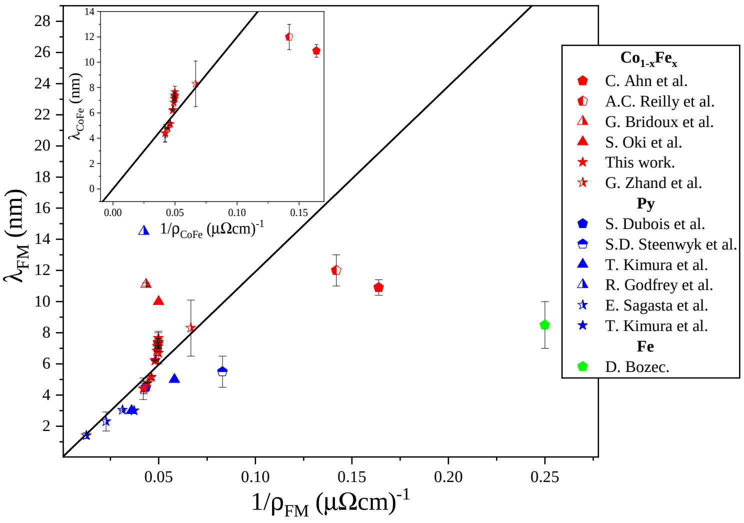

Figure 6.9: Plot of $\frac{1}{\rho_{\text{FM}}}$ versus λ_{FM} taken from SA (star), LSV (triangle) and CPP (pentagon) measurements. The inset shows our data and other CoFe values from the literature. The solid black lines in both figures are a linear fit used to extract the relationship between $\frac{1}{\rho_{\text{FM}}}$ and λ_{FM}. CoFe references are given in Table 6.1. Py: E. Sagasta et al. [10]; T. Kimura et al. [11] (SA), [12] (LSV); S. Dubois et al. [13]; R. Godfrey et al. [14]; S.D. Steenwyk et al. [15]. Fe: D. Bozec [16].

The inset of Figure 6.9 depicts low temperature measurements of CoFe only. Again, this work and the other SA measurement [71] roughly scale with the inverse resistivity, whereas the CPP measurements fall below the linear trend. A linear fit with the intercept fixed at the origin yields: λ_{CoFe}=1.12±0.03 fΩm$^2 \frac{1}{\rho_{\mathrm{CoFe}}}$. This relationship is quite similar to λ_{Py}=0.91±0.04 fΩm$^2 \frac{1}{\rho_{\mathrm{Py}}}$ found recently for Py [10]. Given that the changes to $\lambda_{\mathrm{CoFe}}\rho_{\mathrm{CoFe}}$ with temperature were not too large, and that a linear relationship between $\frac{1}{\rho_{\mathrm{CoFe}}}$ and λ_{CoFe} exists for our data and other published values, there is good evidence for the validity of the EY mechanism in CoFe as suggested by Berger [201].

6.4 Conclusions

In this work, the temperature dependence of λ_{CoFe} and α_{CoFe} for two $\mathrm{Co_{70}Fe_{30}}$ wires were extracted using a spin absorption (SA) technique. Slight variations were observed in the values of α_{CoFe} and λ_{CoFe} obtained from two identical devices, which highlighted that there are inevitable variations between devices even when fabricated alongside one another. The vast majority of studies that employ the SA technique only measure a single device. It would be sensible in future studies to fabricate a large number of geometrically identical absorption devices to quantify and account for these potential variations.

Average spin diffusion lengths of λ_{CoFe}=(7.4±0.6) nm and (4.4±0.7) nm at 5 and 250 K respectively were obtained; close to those previously reported in the literature. The average spin polarisation was 20% higher than values found in a slightly different alloy composition ($\mathrm{Co_{60}Fe_{40}}$) [71], reaching a maximum of $\alpha_{\mathrm{CoFe}} = 0.74 \pm 0.02$ at 5 K. α_{CoFe} did not exhibit the low temperature reduction commonly associated with Kondo scattering from interdiffused MIs at the FM/NM interfaces; which was suprising given the tendency of shadow deposited devices to exhibit this behaviour.

The product of the average CoFe resistivity and spin diffusion length ($\lambda_{\mathrm{CoFe}}\rho_{\mathrm{CoFe}}$) was roughly temperature independent. Moreover, a general linear trend was observed between λ_{CoFe} and $\frac{1}{\rho_{\mathrm{CoFe}}}$ for our data and values from the literature. A linear fit yielded λ_{CoFe}=1.12±0.03 fΩm$^2 \frac{1}{\rho_{\mathrm{CoFe}}}$. These observations suggest that spin relaxation in CoFe is governed by the EY mechanism, as predicted by Berger [201]. Interestingly, values of λ_{CoFe} obtained in SA measurements are longer than expected from published values from CPP-MR techniques. This is either a consequence of the differences in deposition techniques used and subsequent dominant defects types, or related to uncertainties in the techniques; this is important to clarify in future work.

CHAPTER 7

Conclusions and Outlook

7.1 Conclusions

This thesis deals with three interconnected subjects all relevant to the study of spin transport in lateral spin valves (LSV) namely: spin injection and transport; the thermal voltages that accompany spin transport; and, measurements of the spin diffusion length of a ferromagnetic nanowire. Two variations of spintronic devices, the LSV and spin absorption device, were used and fabricated using a shadow deposition method allowing for the entire device to be deposited in situ.

In the first experimental chapter, the temperature dependence of spin injection and transport were investigated in $Co_{70}Fe_{30}$/Cu LSVs for the first time. Two sets of devices were fabricated each with different $Co_{70}Fe_{30}$ thicknesses, namely, 15 nm and 30 nm. Compared to previous $Co_{60}Fe_{40}$/Cu LSVs [43], which used a two-step lithography process, extracted spin polarisations were found to be significantly higher. It was concluded that this was due to the high quality transparent interfaces achieved with a shadow deposition technique; and/or the slightly more Co rich composition being favourable for high spin polarisations. Thus, the potential combination of both factors is promising for achieving high spin signals. However, the work also highlighted one important caveat; that a thin CoFe electrode must be used as the spin diffusion properties of the Cu were strongly affected by the amount of CoFe evaporated. This was due to magnetic impurities (MIs) from the electrode material being incorporated into the Cu channel during shadow deposition. Direct evidence for these dilute bulk MIs was the presence of a Kondo upturn in the Cu resistivity of the 30 nm set. Furthermore, contributions from other MIs, that were not detectable in the resistivity, suppressed and altered the temperature dependence of λ_{Cu} even at room temperature. In contrast, a long λ_{Cu} was obtained in the 15 nm set and was comparable to other clean Py/Cu devices in the literature [78], reaching a maximum of ≈ 870 nm at 25 K. Furthermore, the spin injection efficiency in the 15 nm set was twice that in the 30 nm set. It was concluded that this was a result of a smaller injecting interface area in the 15 nm set, considering that the sides of the CoFe were also in contact with the channel, and potentially the higher CoFe resistivity. Both factors increased the spin resistance of the injecting electrode and decreased the backflow of spins. This study demonstrated that the thickness of the electrode used is an incredibly important parameter in shadow deposited devices; and that MI contamination from increasing the electrode thickness can be as severe as others have observed in heavily annealed devices [81].

In Chapter 5, the thermal background voltages that arise during a non-local measurement of $Co_{70}Fe_{30}$/Cu LSVs were reported and analysed for the first time. Two heating effects were observed: the Peltier heating/cooling at the injecting interface; and, Joule heating in the path of the injection current. Each heating effect was converted into a measurable voltage through the Seebeck effect at the detecting interface. At high temperatures ($T > 100$ K), the Joule and Peltier induced thermal voltages increased with temperature following the rise in power dissipated by each effect and the detection efficiency. Interestingly, the Peltier voltage decreased to a small constant below 100 K, whereas the Joule voltage increased. A simple model based on Fourier's law was applied to extract the thermal conductance of the Cu/SiO_2 interface and the characteristic decay length for each thermal voltage. The limiting factor for heat flow within the devices was shown to be the thermal interface conductance which decreased from ≈ 35 MWm^{-2}K^{-1} at room temperature to ≈ 3 MWm^{-2}K^{-1} at 20 K. Below 20 K, where heat flow into the substrate was greatly reduced, Joule heating induced temperature changes were large enough to change the thermal and spin dependent parameters $\propto I^2$ during a measurement and small higher order voltage responses arose. Moreover, the length dependent decay of the Peltier voltage was significantly different to the Joule voltage below 60 K. It was suggested that the phonon mean free path in the SiO_2 substrate could be comparable to the device dimensions (~ 100 nm) at 60 K, and there was a transition from diffusive to quasi-ballistic heat transport into the substrate. This transition led to the decrease in the thermal interface conductance which manifested differently for the Joule and Peltier induced voltages. This work has demonstrated that even without in situ measurements of the thermal conductivities and thermopower of device elements, which are tricky in nanostructures, some understanding of the device thermal response can be achieved. Additionally, the possibility of quasi-ballistic phonon transport from nanoscale metallic LSVs into dielectric substrates has broad implications. Not only for understanding thermal transport during spin related measurements, but also for heat sinking in future nanoscale devices.

In the final experimental chapter, a spin absorption technique was employed to extract the temperature dependence of the spin diffusion length of $Co_{70}Fe_{30}$ nanowires. Average values of λ_{CoFe} were (7.4 ± 0.6) nm and (4.4 ± 0.7) nm at 5 and 250 K respectively. These values are comparable to those found elsewhere for similar alloy compositions, which tend to fall between 10 to 8 nm at low temperatures. Importantly, the average λ_{CoFe} followed the EY mechanism as predicted by Berger [201] with only small changes to the product $\lambda_{\mathrm{CoFe}}\rho_{\mathrm{CoFe}}$ between 5 and 250 K. Combining our results with other values from the literature the relationship $\lambda_{\mathrm{CoFe}}=1.12\pm0.03\ \mathrm{f\Omega m^2}\frac{1}{\rho_{\mathrm{CoFe}}}$ was yielded.

7.2 Outlook

LSVs are a powerful tool for the study of spin and thermal transport, only a very small aspect of which we have investigated here. A number of interesting questions were raised during this research which warrant further work. Firstly, Chapter 4 raised some interesting questions regarding the weak temperature dependence of the spin lifetime at high temperatures. Specifically, is it a consequence of spin-orbit scattering from MI contaminated regions close to the surfaces in the limit where the dimensions are comparable to (but smaller than) the electronic mean free path; or, is it as a result of Kondo scattering with a high T_K? Both effects had surprisingly similar temperature dependences so, without knowing the location of the impurities we could not distinguish between the two interpretations. Al based devices are ideal to investigate this as the high Fermi energy negates the formation of local moments and Kondo scattering.

Secondly, a basic understanding of thermal transport within LSVs was achieved with our simple model but this work would benefit from actual measurements of nanoscale thermopowers and thermal conductivities; particularly to understand the non-linear behaviour of the Joule induced voltage at low temperatures. Additionally, the possibility of quasi-ballistic heat transport into the substrate warrants further investigation. The onset of quasi-ballistic heat transfer should occur when the dimensions of the nanoscale hotspot are comparable to the average phonon mean free path in the substrate. Further clarification could therefore be achieved by varying the width of the LSV components patterned on the same substrate. Heat transfer from wide devices, that far exceed the mean free paths of the phonons in the substrate, should remain diffusive to a much lower temperature and allow for the intrinsic thermal boundary conductance between the Cu and SiO_2 to be extracted. By decreasing the device dimensions, ballistic transport should become increasingly important at higher temperatures and the thermal boundary conductance extracted should decrease. Similarly, changing the substrate to sapphire, which has an average much longer mean free path of 100 to 150 nm at room temperature [196], should enhance the ballistic effects.

Lastly, the measurements of the spin diffusion length of $Co_{70}Fe_{30}$ in Chapter 6 were only a starting point; curtailed by the onset of the COVID-19 pandemic. In future experiments, using much thinner $Co_{70}Fe_{30}$ would ensure longer Cu spin diffusion lengths and allow a wider array of $Co_{70}Fe_{30}$ widths and thus resistivities to be characterised. The goal here would be to obtain a larger body of measurements for ferromagnetic spin diffusion lengths, as is available for NM metals, to better understand the factors affecting spin diffusion in FMs.

BIBLIOGRAPHY

[1] J. D. Coey. *Magnetism and magnetic materials.* Cambridge University Press, 2009.

[2] M. C. Rosamond, J. T. Batley, G. Burnell, B. J. Hickey, and E. H. Linfield. High contrast 3d proximity correction for electron-beam lithography. *Microelectronic Engineering*, 143(C):5–10, 2015.

[3] J. T. Batley. *Spin Transport in Lateral Spin Valves.* PhD thesis, University of Leeds, 2015.

[4] G. Stefanou, F. Menges, K. A. Moran, M. Ali, M. C. Rosamond, B. Gotsmann, R. Allenspach, G. Burnell, and B. J. Hickey. Scanning thermal microscopy and ballistic phonon transport in lateral spin valves. *manuscript submitted for publication*, 2020.

[5] S. J. Mason, A. Hojem, D. J. Wesenberg, A. D. Avery, and B. L. Zink. Determining absolute seebeck coefficients from relative thermopower measurements of thin films and nanostructures. *Journal of Applied Physics*, 127(8):085101, 2020.

[6] E. Mun, S. L. Bud'ko, M. S. Torikachvili, and P. C. Canfield. Experimental setup for the measurement of the thermoelectric power in zero and applied magnetic field. *Measurement Science and Technology*, 21(5):055104, 2010.

[7] J. Blatt. *Thermoelectric Power of Metals.* Springer US, 1976.

[8] A. V. Gold, D. K. C. Macdonald, W. B. Pearson, and I. M. Templeton. The thermoelectric power of pure copper. *The Philosophical Magazine: A Journal of Theoretical Experimental and Applied Physics*, 5(56):765–786, 1960.

[9] S. Srichandan, S. Wimmer, S. Pöllath, M. Kronseder, H. Ebert, C. H. Back, and C. Strunk. Magnon scattering in the transport coefficients of CoFe thin films. *Physical Review B*, 98:020406, 2018.

[10] E. Sagasta, Y. Omori, M. Isasa, Y. Otani, L. E. Hueso, and F. Casanova. Spin diffusion length of permalloy using spin absorption in lateral spin valves. *Applied Physics Letters*, 111(8):082407, 2017.

[11] T. Kimura, J. Hamrle, and Y. Otani. Estimation of spin-diffusion length from the magnitude of spin-current absorption: Multiterminal ferromagnetic/nonferromagnetic hybrid structures. *Physical Review B*, 72(1), 2005.

[12] T. Kimura, T. Sato, and Y. Otani. Temperature evolution of spin relaxation in a NiFe/Cu lateral spin valve. *Physical Review Letters*, 100, 2008.

[13] S. Dubois, L. Piraux, J. M. George, K. Ounadjela, J. L. Duvail, and A. Fert. Evidence for a short spin diffusion length in permalloy from the giant magnetoresistance of multilayered nanowires. *Physical Review B*, 60:477–484, 1999.

[14] R. Godfrey and M. Johnson. Spin injection in mesoscopic silver wires: Experimental test of resistance mismatch. *Physical Review Letters*, 96, 2006.

[15] S. D. Steenwyk, S. Y. Hsu, R. Loloee, J. Bass, and W. P. Pratt. Perpendicular-current exchange-biased spin-valve evidence for a short spin-diffusion length in permalloy. *Journal of Magnetism and Magnetic Materials*, 170(1):1–6, 1997.

[16] D. Bozec. *Current perpendicular to the Plane Magnetoresistance of Magnetic Multilayers.* PhD thesis, University of Leeds, 2000.

[17] W. Thompson. On the electro-dynamic qualities of metals: Effects of magnetization on the electric conductivity of nickel and of iron. *Proceedings of the Royal Society*, 8:546–550, 1857.

[18] E. H. Hall. Xviii. on the “rotational coefficient” in nickel and cobalt. *The London, Edinburgh and Dublin Philosophical Magazine and Journal of Science*, 12(74): 157–172, 1881.

[19] G. Binasch, P. Grünberg, F. Saurenbach, and W. Zinn. Enhanced magnetoresistance in layered magnetic structures with antiferromagnetic interlayer exchange. *Physical Review B*, 39:4828–4830, 1989.

[20] M. N. Baibich, J. M. Broto, A. Fert, F. Nguyen Van Dau, F. Petroff, P. Etienne, G. Creuzet, A. Friederich, and J. Chazelas. Giant magnetoresistance of (001)Fe/(001)Cr magnetic superlattices. *Physical Review Letters*, 61:2472–2475, 1988.

[21] S. S. P. Parkin. *Spin Dependent Transport in Magnetic Nanostructures*, chapter Applications of Magnetic Nanostructures. Taylor and Francis, 2002.

[22] C. Chappert, A. Fert, and F. N. Van Dau. The emergence of spin electronics in data storage. *Nature Materials*, 6(11):813–823, 2007.

[23] D. E. Nikonov, G. I. Bourianoff, and P. A. Gargini. Power dissipation in spintronic devices out of thermodynamic equilibrium. *Journal of Superconductivity and Novel Magnetism*, 19(6):497–513, 2006.

[24] B. Behin-Aein, D. Datta, S. Salahuddin, and S. Datta. Proposal for an all-spin logic device with built-in memory. *Nature Nanotechnology*, 5(4):266–270, 2010.

[25] S. Datta and B. Das. Electronic analog of the electro-optic modulator. *Applied Physics Letters*, 56(7):665–667, 1990.

[26] M. Johnson and R. H. Silsbee. Interfacial charge-spin coupling: Injection and detection of spin magnetization in metals. *Physical Review Letters*, 55:1790–1793, 1985.

[27] F. J. Jedema, A. T. Filip, and B. J. van Wees. Electrical spin injection and accumulation at room temperature in an all-metal mesoscopic spin valve. *Nature*, 410(6826):345–348, 2001.

[28] G. Mihajlović, D. K. Schreiber, Y. Liu, J. E. Pearson, S. D. Bader, A. K. Petford-Long, and A. Hoffmann. Enhanced spin signals due to native oxide formation in $Ni_{80}Fe_{20}$/Ag lateral spin valves. *Applied Physics Letters*, 97(11):112502, 2010.

[29] F. J. Jedema, H. B. Heersche, A. T. Filip, J. J. A. Baselmans, and B. J. van Wees. Electrical detection of spin precession in a metallic mesoscopic spin valve. *Nature*, 416(6882):713–716, 2002.

[30] L. O'Brien, M. J. Erickson, D. Spivak, H. Ambaye, R. J. Goyette, V. Lauter, P. A. Crowell, and C. Leighton. Kondo physics in non-local metallic spin transport devices. *Nature Communications*, 5(1):3927, 2014.

[31] T. Kimura and Y. Otani. Large spin accumulation in a permalloy-silver lateral spin valve. *Physical Review Letters*, 99, 2007.

[32] G. Salis, A. Fuhrer, R. R. Schlittler, L. Gross, and S. F. Alvarado. Temperature dependence of the nonlocal voltage in an Fe/GaAs electrical spin-injection device. *Physical Review B*, 81, 2010.

[33] S. Toshio, S. Tomoyuki, O. Tohru, S. Masashi, S. Yoshishige, and N. Kiyoshi. Room-temperature electron spin transport in a highly doped Si channel. *Applied Physics Express*, 4(2), 2011.

[34] T. Wakamura, N. Hasegawa, K. Ohnishi, Y. Niimi, and Y. Otani. Spin injection into a superconductor with strong spin-orbit coupling. *Physical Review Letters*, 112:036602, 2014.

[35] T. Wakamura, H. Akaike, Y. Omori, Y. Niimi, S. Takahashi, A. Fujimaki, S. Maekawa, and Y. Otani. Quasiparticle-mediated spin hall effect in a superconductor. *Nature Materials*, 14(7):675–678, 2015.

[36] N. Poli, J. P. Morten, M. Urech, A. Brataas, D. B. Haviland, and V. Korenivski. Spin injection and relaxation in a mesoscopic superconductor. *Physical Review Letters*, 100(13), 2008.

[37] M. Erekhinsky, F. Casanova, I. K. Schuller, and A. Sharoni. Spin-dependent seebeck effect in non-local spin valve devices. *Applied Physics Letters*, 100(21): 212401, 2012.

[38] A. Slachter, F. L. Bakker, J-P. Adam, and B. J. van Wees. Thermally driven spin injection from a ferromagnet into a non-magnetic metal. *Nature Physics*, 6(11): 879–882, 2010.

[39] S. R. Bakaul, S. Hu, and T. Kimura. Thermal gradient driven enhancement of pure spin current at room temperature in nonlocal spin transport devices. *Physical Review B*, 88:184407, 2013.

[40] N. Kuhlmann, C. Swoboda, A. Vogel, T. Matsuyama, and G. Meier. All-metal lateral spin valve operated by spin pumping. *Physical Review B*, 87:104409, 2013.

[41] E. Villamor, M. Isasa, L. E. Hueso, and F. Casanova. Temperature dependence of spin polarization in ferromagnetic metals using lateral spin valves. *Physical Review B*, 88, 2013.

[42] G. Bridoux, M. V. Costache, J. Van de Vondel, I. Neumann, and S. O. Valenzuela. Enhanced spin signal in nonlocal devices based on a ferromagnetic CoFeAl alloy. *Applied Physics Letters*, 99(10):102107, 2011.

[43] G. Zahnd, L. Vila, P. V. Tuong, A Marty, P. Laczkowski, W. Torres, C. Beigné, C. Vergnaud, M. Jamet, and J-P. Attané. Comparison of the use of NiFe and CoFe as electrodes for metallic lateral spin valves. *Nanotechnology*, 27, 2015.

[44] S. Oki, S. Yamada, H. Naoki, M. Masanobu, and T. Kimura. Effect of addition of Al to single-crystalline CoFe electrodes on nonlocal spin signals in lateral spin-valve devices. *Applied Physics Express*, 5(6), 2012.

[45] S. S. P. Parkin, C. Kaiser, A. Panchula, P. M. Rice, B. Hughes, M. Samant, and S. Yang. Giant tunnelling magnetoresistance at room temperature with MgO (100) tunnel barriers. *Nature Materials*, 3(12):862–867, 2004.

[46] H. Zou, X. J. Wang, and Y. Ji. Reduction of spin-flip scattering in metallic nonlocal spin valves. *Journal of Vacuum Science and Technology B*, 28(6):1314–1317, 2010.

[47] F. K. Dejene, J. Flipse, and B. J. van Wees. Verification of the thomson-onsager reciprocity relation for spin caloritronics. *Physical Review B*, 90:180402, 2014.

[48] C. H. Back, G. E. W. Bauer, and B. L. Zink. Special issue on spin caloritronics. *Journal of Physics D: Applied Physics*, 52(23):230301, 2019.

[49] P. Varshney and H. Agrawal. Spintronics technology: A review. 2014.

[50] F. Casanova, A. Sharoni, M. Erekhinsky, and I. K. Schuller. Control of spin injection by direct current in lateral spin valves. *Physical Review B*, 79:184415, 2009.

[51] O. Stejskal, J. Hamrle, J. Pištora, and Y. Otani. Optimization of spin injection and spin detection in lateral nanostructures by geometrical means. *Journal of Magnetism and Magnetic Materials*, 414:132 – 143, 2016.

[52] S. Garzon, I. Zutić, and R. Webb. Temperature dependent asymmetry of the nonlocal spin-injection resistance: Evidence for spin nonconserving interface scattering. *Physical Review Letters*, 94:176601, 2005.

[53] S. Katsuaki and S. Eiji. *Spintronics for Next Generation Innovative Devices.* John Wiley and Sons, 2015.

[54] I. Zutic, J. Fabian, and S. Das Sarma. Spintronics: Fundamentals and applications. *Reviews of Modern Physics*, 76:323–410, 2004.

[55] J. Bass and W. P. Pratt. Spin-diffusion lengths in metals and alloys, and spin-flipping at metal/metal interfaces: an experimentalist's critical review. *Journal of Physics: Condensed Matter*, 19:183201, 2007.

[56] E. Villamor, M. Isasa, L. E. Hueso, and F. Casanova. Contribution of defects to the spin relaxation in copper nanowires. *Physical Review B*, 87, 2013.

[57] R. K. Bennet, A. Hojem, and B. L. Zink. Thermal gradients and anomalous nernst effects in membrane-supported nonlocal spin valves. *Physical Review B*, 100:104404, 2019.

[58] F. L. Bakker, A. Slachter, J. P. Adam, and B. J. van Wees. Interplay of peltier and seebeck effects in nanoscale nonlocal spin valves. *Physical Review Letters*, 105, 2010.

[59] S. Maekawa, S. O. Valenzuela, E. Saitoh, and T. Kimura. *Spin Current.* Oxford University Press, 2012.

[60] P. Mohn. *Magnetism in the Solid State: An Introduction.* Springer, 2003.

[61] C. M. Hurd. *Electrons in Metals.* John Wiley and Sons, 1975.

[62] L. Hodges, H. Ehrenreich, and N. D. Lang. Interpolation scheme for band structure of noble and transition metals: Ferromagnetism and neutron diffraction in ni. *Physical Review*, 152:505–526, 1966.

[63] I. I. Mazin. How to define and calculate the degree of spin polarization in ferromagnets. *Physical Review Letters*, 83:1427–1430, 1999.

[64] N. F. Mott and R. H. Fowler. The electrical conductivity of transition metals. *Proceedings of the Royal Society of London. Series A - Mathematical and Physical Sciences*, 153(880):699–717, 1936.

[65] P. C. van Son, H. van Kempen, and P. Wyder. Boundary resistance of the ferromagnetic-nonferromagnetic metal interface. *Physical Review Letters*, 58(21): 2271–2273, 1987.

[66] F. J. Jedema, M. S. Nijboer, A. T. Filip, and B. J. van Wees. Spin injection and spin accumulation in all-metal mesoscopic spin valves. *Phys. Rev. B*, 67:085319, 2003.

[67] T. Kimura, J. Hamrle, Y. Otani, K. Tsukagoshi, and Y. Aoyagi. Suppression of spin accumulation in nonmagnet due to ferromagnetic ohmic contact. *Applied Physics Letters*, 85(17):3795–3796, 2004.

[68] Y. Ji, A. Hoffmann, J. E. Pearson, and S. D. Bader. Enhanced spin injection polarization in Co/Cu/Co nonlocal lateral spin valves. *Applied Physics Letters*, 88(5):052509, 2006.

[69] T. Nomura, K. Ohnishi, and T. Kimura. Geometrical dependence of spin current absorption into a ferromagnetic nanodot. *Journal of Applied Physics*, 120(14): 142121, 2016.

[70] P. Laczkowski, H. Jaffrès, W. Savero-Torres, J. C. Rojas-Sánchez, Y. Fu, N. Reyren, C. Deranlot, L. Notin, C. Beigné, J. P. Attané, L. Vila, J. M. George, and A. Marty. Evaluation of spin diffusion length of AuW alloys using spin absorption experiments in the limit of large spin-orbit interactions. *Physical Review B*, 92:214405, 2015.

[71] G. Zahnd, L. Vila, V. T. Pham, M. Cosset-Cheneau, W. Lim, A. Brenac, P. Laczkowski, A. Marty, and J. P. Attané. Spin diffusion length and polarization of ferromagnetic metals measured by the spin-absorption technique in lateral spin valves. *Physical Review B*, 98, 2018.

[72] F. Bloch. Nuclear induction. *Physical Review*, 70:460–474, 1946.

[73] H. C. Torrey. Bloch equations with diffusion terms. *Physical Review*, 104:563–565, 1956.

[74] M. Cosset-Chéneau, L. Vila, G. Zahnd, D. Gusakova, V. T. Pham, C. Grèzes, X. Waintal, A. Marty, H. Jaffrès, and J.-P. Attané. Measurement of the spin absorption anisotropy in lateral spin valves. *Physical Review Letters*, 126:027201, 2021.

[75] Z. Zhu, X. Zheng, G. Li, H. Bai, J. Su, Y. Zhang, and J. Cai. Strong spin orientation-dependent spin current diffusion and inverse spin hall effect in a ferromagnetic metal. *NPG Asia Materials*, 12(1):12, 2020.

[76] R. J. Elliott. Theory of the effect of spin-orbit coupling on magnetic resonance in some semiconductors. *Physical Review*, 96:266–279, 1954.

[77] Y. Yafet. g factors and spin-lattice relaxation of conduction electrons. *Solid State Physics*, 14:1 – 98, 1963.

[78] J. T. Batley, M. C. Rosamond, M. Ali, E. H. Linfield, G. Burnell, and B. J. Hickey. Spin relaxation through kondo scattering in Cu/Py lateral spin valves. *Physical Review B*, 92:220420, 2015.

[79] E. Y. Tsymbal and I. Zutic, editors. *Spintronics Handbook: Spin Transport and Magnetism*, volume 1. Taylor Francis, 2019.

[80] P. Monod and F. Beuneu. Conduction-electron spin flip by phonons in metals: Analysis of experimental data. *Physical Review B*, 19:911–916, 1979.

[81] J. D. Watts, L. O'Brien, J. S. Jeong, K. A. Mkhoyan, P. A. Crowell, and C. Leighton. Magnetic impurities as the origin of the variability in spin relaxation rates in Cu-based spin transport devices. *Physical Review Materials*, 3:124409, 2019.

[82] S. Heers. *Effect of spin-orbit scattering on transport properties of low-dimensional dilute alloys.* PhD thesis, Julich, 2011.

[83] M. Gradhand, D. V. Fedorov, P. Zahn, and I. Mertig. Fully relativistic ab initio treatment of spin-flip scattering caused by impurities. *Physical Review B*, 81, 2010.

[84] H. Idzuchi, Y. Fukuma, and Y. Otani. Spin transport in non-magnetic nanostructures induced by non-local spin injection. *Physica E: Low-dimensional Systems and Nanostructures*, 68:239 – 263, 2015.

[85] F. Beuneu and P. Monod. The elliott relation in pure metals. *Physical Review B*, 18:2422–2425, 1978.

[86] P. W. Anderson. Localized magnetic states in metals. *Physical Review*, 124: 41–53, 1961.

[87] J. Kondo. Resistance Minimum in Dilute Magnetic Alloys. *Progress of Theoretical Physics*, 32(1):37–49, 1964.

[88] L. Joly, J. P. Kappler, P. Ohresser, Ph. Sainctavit, Y. Henry, F. Gautier, G. Schmerber, D. J. Kim, C. Goyhenex, H. Bulou, O. Bengone, J. Kavich, P. Gambardella, and F. Scheurer. Kondo screening of the spin and orbital magnetic moments of Fe impurities in Cu. *Physical Review B*, 95:041108, 2017.

[89] G. Gruner and A. Zawadowski. Magnetic impurities in non-magnetic metals. *Reports on Progress in Physics*, 37(12):1497–1583, 1974.

[90] M. D. Daybell and W. A. Steyert. Localized magnetic impurity states in metals: Some experimental relationships. *Reviews of Modern Physics*, 40:380–389, 1968.

[91] J. R. Schrieffer. The kondo effect - the link between magnetic and nonmagnetic impurities in metals? *Journal of Applied Physics*, 38(3):1143–1150, 1967.

[92] M. D. Daybell, W. P. Pratt, and W. A. Steyert. Specific heat of dilute Cu(Fe) alloys far below the kondo temperature. *Physical Review Letters*, 21:353–356, 1968.

[93] J. P. Franck, F. D. Manchester, Douglas L. Martin, and D. Macdonald. The specific heat of pure copper and of some dilute copper + iron alloys showing a minimum in the electrical resistance at low temperatures. *Proceedings of the Royal Society of London. Series A. Mathematical and Physical Sciences*, 263(1315):494–507, 1961.

[94] T. M. Tritt. *Thermal Conductivity: Theory, Properties and Applications.* Springer US, 2004.

[95] W.M. Star, P.C.M. Gubbens, and J.J. de Jong. Lorenz-number and the kondo-effect in copper-iron. *Physics Letters A*, 36(1):15–16, 1971.

[96] A. Kjekshus and W. B. Pearson. Thermoelectricity and electrical resistivity of dilute copper alloys of chromium, manganese, iron and cobalt at low temperatures. *Canadian Journal of Physics*, 40:98, 1962.

[97] J. D. Watts, J. S. Jeong, L. O'Brien, K. A. Mkhoyan, P. A. Crowell, and C. Leighton. Room temperature spin kondo effect and intermixing in Co/Cu non-local spin valves. *Applied Physics Letters*, 110(22):222407, 2017.

[98] K. W. Kim, L. O'Brien, P. A. Crowell, C. Leighton, and M. D. Stiles. Theory of kondo suppression of spin polarization in nonlocal spin valves. *Physical Review B*, 95:104404, 2017.

[99] P. G. Klemens and R. K. Williams. Thermal conductivity of metals and alloys. *International Metals Reviews*, 31(1):197–215, 1986.

[100] A. D. Avery, S. J. Mason, D. Bassett, D. Wesenberg, and B. L. Zink. Thermal and electrical conductivity of approximately 100-nm permalloy, Ni, Co, Al, and Cu films and examination of the wiedemann-franz law. *Phys. Rev. B*, 92:214410, 2015.

[101] R. Adari, T. Patil, M. Murthy, R. Maheshwari, G. Vaidya, S. Ganguly, and D. Saha. Enhanced magnetoresistance in lateral spin-valves. *Applied Physics Letters*, 97(11):112505, 2010.

[102] M. Johnson. Optimized device characteristics of lateral spin valves. *IEEE Transactions on Electron Devices*, 54(5):1024–1031, 2007.

[103] T. Kimura, Y. Otani, and J. Hamrle. Enhancement of spin accumulation in a nonmagnetic layer by reducing junction size. *Physical Review B*, 73:132405, 2006.

[104] Keithley Instruments Inc. *Low level measurements handbook: Precision DC current, voltage and resistance measurements.* Keithley, Cleveland, OH., 2004.

[105] A. Daire, W. Goeke, and M. A. Tupta. White paper: New instruments can lock out lock-ins. *Keithley Instruments Inc*, 2005.

[106] Y. Cai, C. Qin, F. Kandaz, X. Shen, C. Zhou, M. Jia, Y. Luo, Y. Wu, and Y. Ji. Quantifying spin relaxation in mesoscopic cu channels via a multitude of nonlocal spin valves. *Physical Review B*, 100:144419, 2019.

[107] A. Pfeiffer, R. Reeve, K. Elphick, A. Hirohata, and M. Kläui. Revealing the importance of interfaces for pure spin current transport. *arXiv*, 2019.

[108] Y. Fukuma, L. Wang, H. Idzuchi, S. Takahashi, S. Maekawa, and Y. Otani. Giant enhancement of spin accumulation and long-distance spin precession in metallic lateral spin valves. *Nature Materials*, 10(7):527–531, 2011.

[109] H. Idzuchi, S. Karube, Y. Fukuma, T. Aoki, and Y. Otani. Impact of interface properties on spin accumulation in dual-injection lateral spin valves. *Applied Physics Letters*, 103(16):162403, 2013.

[110] X. Wang, Y. Nie, Q. Xia, and G. Guo. Electrical spin injection through dual ferromagnetic electrodes in nonlocal spin valves. *Physical Review B*, 98:184427, 2018.

[111] K. Arvind and P. C. Srivastava. Magnetic, morphological and structural investigations of CoFe/Si interfacial structures. *Journal of Experimental Nanoscience*, 10(10):803–818, 2015.

[112] A. F. Mayadas and M. Shatzkes. Electrical-resistivity model for polycrystalline films: the case of arbitrary reflection at external surfaces. *Physical Review B*, 1: 1382–1389, 1970.

[113] S. Srichandan. *Electrical and thermal transport coefficients of CoFe thin films deposited on a microcalorimeter.* Physik Universitdat Regensberg, 2016.

[114] T. McGuire and R. Potter. Anisotropic magnetoresistance in ferromagnetic 3d alloys. *IEEE Transactions on Magnetics*, 11(4):1018–1038, 1975.

[115] E. H. Sondheimer. The mean free path of electrons in metals. *Advances in Physics*, 1(1):1–42, 1952.

[116] K. Fuchs and N. F. Mott. The conductivity of thin metallic films according to the electron theory of metals. *Proceedings of the Cambridge Philosophical Society*, 34 (1):100, 1938.

[117] M. Haidar and M. Bailleul. Thickness dependence of degree of spin polarization of electrical current in permalloy thin films. *Physical Review B*, 88:054417, 2013.

[118] X. Zhang, H. Xu, B. Lai, Q. Lu, X. Lu, Y. Chen, W. Niu, C. Gu, W. Liu, X. Wang, C. Liu, Y. Nie, and Y. He, L.and Xu. Direct observation of high spin polarization in Co2FeAl thin films. *Scientific Reports*, 8(1):8074, 2018.

[119] Y. Liu, Z. Yuan, R. J. H. Wesselink, A. A. Starikov, M. van Schilfgaarde, and P. J. Kelly. Direct method for calculating temperature-dependent transport properties. *Physical Review B*, 91:220405, 2015.

[120] H. Zou and Yi Ji. The origin of high surface spin-flip rate in metallic nonlocal spin valves. *Applied Physics Letters*, 101, 2012.

[121] L. O'Brien, D. Spivak, J. S. Jeong, K. A. Mkhoyan, P. A. Crowell, and C. Leighton. Interdiffusion-controlled kondo suppression of injection efficiency in metallic nonlocal spin valves. *Physical Review B*, 93, 2016.

[122] O. Újsághy and A. Zawadowski. Spin-orbit-induced kondo size effect in thin films with 5/2-spin impurities. *Physical Review B*, 60(15):10602–10605, 1999.

[123] O. Újsághy and A. Zawadowski. Spin-orbit-induced magnetic anisotropy for impurities in metallic samples. I. surface anisotropy. *Physical Review B*, 57(18): 11598–11608, 1998.

[124] O. Újsághy, L. Szunyogh, and A. Zawadowski. Revised theory of the magnetic surface anisotropy of impurities in metallic mesoscopic samples. *Physical Review B*, 75:064425, 2007.

[125] W. Umrath. *Fundamentals of Vacuum Technology.* Leybold, 2007.

[126] D. Gall. Electron mean free path in elemental metals. *Journal of Applied Physics*, 119:085101, 2016.

[127] J. H. Mooij. Electrical conduction in concentrated disordered transition metal alloys. *physica status solidi (a)*, 17(2):521–530, 1973.

[128] N. Giordano, W. Gilson, and D. E. Prober. Experimental study of anderson localization in thin wires. *Phys. Rev. Lett.*, 43:725–728, Sep 1979.

[129] J. S. Dugdale. *The Electrical Properties of Metals and Alloys.* Edward Arnold, 1977.

[130] A. Bid, A. Bora, and A. K. Raychaudhuri. Temperature dependence of the resistance of metallic nanowires of diameter $\geqslant$ 15 nm: Applicability of bloch-gruneisen theorem. *Physical Review B*, 74(3):035426, 2006.

[131] W. Ma, X. Zhang, and K. Takahashi. Electrical properties and reduced debye temperature of polycrystalline thin gold films. *Journal of Physics D: Applied Physics*, 43(46):465301, 2010.

[132] W. Zhang, S. H. Brongersma, Z. Li, D. Li, O. Richard, and K. Maex. Analysis of the size effect in electroplated fine copper wires and a realistic assessment to model copper resistivity. *Journal of Applied Physics*, 101(6):063703, 2007.

[133] S. Kim, H. Suhl, and I. K. Schuller. Surface phonon scattering in the electrical resistivity on Co/Ni superlattices. *Physical Review Letters*, 78(2):322–325, 1997.

[134] R. A. Matula. Electrical resistivity of copper, gold, palladium, and silver. *Journal of Physical and Chemical Reference Data*, 8(1147), 1979.

[135] Y. P. Timalsina, A. Horning, R. F. Spivey, K. M. Lewis, T. S. Kuan, G. Wang, and T. M. Lu. Effects of nanoscale surface roughness on the resistivity of ultrathin epitaxial copper films. *Nanotechnology*, 26(7):075704, 2015.

[136] Z. Cheng, L. Liu, S. Xu, M. Lu, and X. Wang. Temperature dependence of electrical and thermal conduction in single silver nanowire. *Scientific reports*, 5: 10718–10718, 2015.

[137] Y. P. Timalsina, X. Shen, G. Boruchowitz, Z . Fu, G. Qian, M. Yamaguchi, G. Wang, K. M. Lewis, and T. M. Lu. Evidence of enhanced electron-phonon coupling in ultrathin epitaxial copper films. *Applied Physics Letters*, 103(19): 191602, 2013.

[138] T. A. Costi, A. C. Hewson, and V. Zlatic. Transport coefficients of the anderson model via the numerical renormalization group. *Journal of Physics: Condensed Matter*, 6(13):2519–2558, mar 1994.

[139] M. S. R. Chari, N. S. Natarajan, and R. G. Sharma. Variation of the kondo temperature with the nature and concentration of the solute metal. *Journal of Low Temperature Physics*, 10(3):309–315, 1973.

[140] W. Wei and G. Bergmann. CuCo: A new surface kondo system. *Physical Review B*, 37(10):5990–5993, 1988.

[141] B. Surer, M. Troyer, P. Werner, T. O. Wehling, A. M. Läuchli, A. Wilhelm, and A. I. Lichtenstein. Multiorbital kondo physics of Co in Cu hosts. *Physical Review B*, 85:085114, 2012.

[142] H. Shiba. On the de haas-van alphen effect in dilute copper alloys containing transition-metal impurities. *Progress of Theoretical Physics*, 50(6):1797–1823, 12 1973.

[143] T. Nishizawa and K. Ishida. The co-cu (cobalt-copper) system. *Bulletin of Alloy Phase Diagrams*, 5(2):161–165, 1984.

[144] T. S. Hutchison and J. Reekie. The room temperature solubility of iron in copper. *Physical Review*, 83:854–855, 1951.

[145] G. Apostolopoulos and C. Papastaikoudis. The influence of thickness on the kondo effect in Cu(Fe) thin films. *Solid State Communications*, 99(4):277–281, 1996.

[146] M. A. Blachly and N. Giordano. Kondo effect in systems of reduced dimensionality. *Physical Review B*, 51:12537–12550, 1995.

[147] T. M. Jacobs and N. Giordano. Kondo size effect in thin Cu(Mn) films. *Europhysics Letters*, 44(1):74–79, 1998.

[148] T. Jacobs and N. Giordano. Kondo behavior of multilayers: Local-moment physics near surfaces. *Physical Review B*, 62:14145–14148, 2000.

[149] T. A. Costi, L. Bergqvist, A. Weichselbaum, J. von Delft, T. Micklitz, A. Rosch, P. Mavropoulos, P. H. Dederichs, F. Mallet, L. Saminadayar, and C. Bäuerle. Kondo decoherence: Finding the right spin model for iron impurities in gold and silver. *Physical Review Letters*, 102:056802, 2009.

[150] D. Goldhaber-Gordon, J. Göres, M. A. Kastner, Hadas Shtrikman, D. Mahalu, and U. Meirav. From the kondo regime to the mixed-valence regime in a single-electron transistor. *Physical Review Letters*, 81:5225–5228, 1998.

[151] W. M. Star, F. B. Basters, G. M. Nap, E. de Vroede, and C. Van Baarle. Toward simple powers of T in the kondo effect: I. low-temperature electrical resistivity of dilute Cu–Fe alloys. *Physica*, 58(4):585 – 622, 1972.

[152] B. Knook. *Thesis*. PhD thesis, University of Leiden, 1962.

[153] G. J. Van Den Berg. Chapter IV anomalies in dilute metallic solutions of transition elements. In C.J. Gorter, editor, *Progress in Low Temperature Physics*, volume 4, pages 194 – 264. Elsevier, 1964.

[154] C. Ahn, K. H. Shin, R. Loloee, J. Bass, and W. P. Pratt. Current-perpendicular-to-plane spin transport properties of CoFe alloys: Spin diffusion length and scattering asymmetry. *Journal of Applied Physics*, 108(2), 2010.

[155] M. Erekhinsky, A. Sharoni, F. Casanova, and I. Schuller. Surface enhanced spin-flip scattering in lateral spin valves. *Applied Physics Letters*, 96:022513–022513, 2010.

[156] G. Mihajlović, J. E. Pearson, S. D. Bader, and A. Hoffmann. Surface spin flip probability of mesoscopic ag wires. *Physical Review Letters*, 104:237202, J 2010.

[157] M. Grobis, I. G. Rau, R. M. Potok, H. Shtrikman, and D. Goldhaber-Gordon. Universal scaling in nonequilibrium transport through a single channel kondo dot. *Physical Review Letters*, 100:246601, 2008.

[158] P. Monod and S. Schultz. Conduction electron spin-flip scattering by impurities in copper. *Journal De Physique*, 43:393–401, 1982.

[159] N. Néel, J. Kröger, R. Berndt, T. O. Wehling, A. I. Lichtenstein, and M. I. Katsnelson. Controlling the kondo effect in CoCu$_n$ clusters atom by atom. *Physical Review Letters*, 101:266803, 2008.

[160] P. Monod. Magnetic field dependence of the kondo resistivity minimum in CuFe and CuMn alloys. *Physical Review Letters*, 19:1113–1117, 1967.

[161] A. López, R. Andrés, J. Pedro, M. Ipatov, J. A. González, J. González, V. Zhukova, and A. Zhukov. Magneto-transport properties of Co–Cu thin films obtained by co-sputtering and sputter gas aggregation. *Nanomaterials*, 11(1), 2021.

[162] X. Shen and Y. Ji. Unusual scaling of kondo spin relaxation. *arXiv*, 2020.

[163] J. Souiete and R. Tournier. Interaction effects on the magnetic properties of transition metal impurities in noble metals. *J. Phys. Colloques*, 32(C1), 1971.

[164] C. Zhou, F. Kandaz, Y. Cai, C. Qin, M. Jia, Z. Yuan, Y. Wu, and Y. Ji. Anisotropic spin relaxation induced by surface spin-orbit effects. *Physical Review B*, 96:094413, 2017.

[165] J. M. MacLaren, T. C. Schulthess, W. H. Butler, R. Sutton, and M. McHenry. Electronic structure, exchange interactions, and curie temperature of FeCo. *Journal of Applied Physics*, 85(8):4833–4835, 1999.

[166] M. Johnson and R. H. Silsbee. Calculation of nonlocal baseline resistance in a quasi-one-dimensional wire. *Physical Review B*, 76:153107, 2007.

[167] S. Kasai, S. Hirayama, Y. K. Takahashi, S. Mitani, K. Hono, H. Adachi, J. Ieda, and S. Maekawa. Thermal engineering of non-local resistance in lateral spin valves. *Applied Physics Letters*, 104(16):162410, 2014.

[168] David Sánchez and Rosa López. Nonlinear phenomena in quantum thermoelectrics and heat. *Comptes Rendus Physique*, 17(10):1060–1071, 2016.

[169] F. R. Fickett. Magnetoresistivity of copper and aluminum at cryogenic temperatures. *eConf*, C720919:539, 1972.

[170] K. Schröder and M. Otooni. Effect of magnetic fields on the absolute seebeck coefficient and the resistivity of thermocouple wires. *Journal of Physics D: Applied Physics*, 4(10):1612–1616, 1971.

[171] A. Kobs, S. Heße, H. P. Oepen, and P. Weinberger. Anisotropic interface magnetoresistances in Pt(111)/Con/Pt(111). *Philosophical Magazine*, 92:2835, 2012.

[172] O. Reimer, D. Meier, M. Bovender, L. Helmich, J. Dreessen, J. Krieft, A. S. Shestakov, C. H. Back, J. Schmalhorst, A. Hütten, G. Reiss, and T. Kuschel. Quantitative separation of the anisotropic magnetothermopower and planar nernst effect by the rotation of an in-plane thermal gradient. *Scientific Reports*, 7(1):40586, 2017.

[173] T. McGuire and R. Potter. Anisotropic magnetoresistance in ferromagnetic 3d alloys. *IEEE Transactions on Magnetics*, 11(4):1018–1038, 1975.

[174] A. Nagarjuna, A. Taisei, and K. Takashi. Asymmetric nonlocal signal induced by thermoelectric effects in a lateral spin valve. *Physica E: Low-dimensional Systems and Nanostructures*, 117:113738, 2020.

[175] A. P. Thakoor, R. Suri, S. K. Suri, and K. L. Chopra. Electron transport properties of copper films. II. thermoelectric power. *Journal of Applied Physics*, 46 (11):4777–4783, 1975.

[176] *Fundementals of Thermoelectricity.* OUP Oxford, Kamran Behnia.

[177] N. Stojanovic, D. H. S. Maithripala, J. M. Berg, and M. Holtz. Thermal conductivity in metallic nanostructures at high temperature: Electrons, phonons, and the wiedemann-franz law. *Physical Review B*, 82:075418, 2010.

[178] P. Nath and K. L. Chopra. Thermal conductivity of copper films. *Thin Solid Films*, 20(1):53 – 62, 1974.

[179] Z. Tong, S. Li, X. Ruan, and H. Bao. Comprehensive first-principles analysis of phonon thermal conductivity and electron-phonon coupling in different metals. *Physical Review B*, 100:144306, 2019.

[180] D. Kojda, R. Mitdank, M. Handwerg, A. Mogilatenko, M. Albrecht, Z. Wang, J. Ruhhammer, M. Kroener, P. Woias, and S. F. Fischer. Temperature-dependent

thermoelectric properties of individual silver nanowires. *Physical Review B*, 91: 024302, 2015.

[181] X. Liang and F. Dai. Reduction of the lorenz number in copper at room temperature due to strong inelastic electron scattering brought about by high-density dislocations. *The Journal of Physical Chemistry Letters*, 10(3):507–512, 2019.

[182] M. N. Ou, T. J. Yang, S. R. Harutyunyan, Y. Y. Chen, C. D. Chen, and S. J. Lai. Electrical and thermal transport in single nickel nanowire. *Applied Physics Letters*, 92(6):063101, 2008.

[183] D. G. Cahill, W. K. Ford, K. E. Goodson, G. D. Mahan, A. Majumdar, H. J. Maris, R. Merlin, and S. R. Phillpot. Nanoscale thermal transport. *Journal of Applied Physics*, 93(2):793–818, 2003.

[184] Q. G. Zhang, B. Y. Cao, X. Zhang, M. Fujii, and K. Takahashi. Influence of grain boundary scattering on the electrical and thermal conductivities of polycrystalline gold nanofilms. *Physical Review B*, 74:134109, 2006.

[185] S. Yoneoka, J. Lee, M. Liger, G. Yama, T. Kodama, M. Gunji, J. Provine, R. T. Howe, K. E. Goodson, and T. W. Kenny. Electrical and thermal conduction in atomic layer deposition nanobridges down to 7 nm thickness. *Nano Letters*, 12 (2):683–686, 2012.

[186] D. Cougnon, F. G. Depla. The seebeck coefficient of sputter deposited metallic thin films: The role of process conditions. *Coatings*, 9(5):299, 2019.

[187] M. Kockert, D. Kojda, R. Mitdank, A. Mogilatenko, Z. Wang, J. Ruhhammer, M. Kroener, P. Woias, and S. F. Fischer. Nanometrology: Absolute seebeck coefficient of individual silver nanowires. *Scientific Reports*, 9(1):20265, 2019.

[188] M. Kockert, R. Mitdank, A. Zykov, S. Kowarik, and S. F. Fischer. Absolute seebeck coefficient of thin platinum films. *Journal of Applied Physics*, 126(10): 105106, 2019.

[189] C. Monachon, L. Weber, and C. Dames. Thermal boundary conductance: A materials science perspective. *Annual Review of Materials Research*, 46:433–463, 2016.

[190] E. Pop. Energy dissipation and transport in nanoscale devices. *Nano Research*, 3(3):147–169, 2010.

[191] Z. Yu, T. Ohara, Y. He, and Patrick E. Hopkins. Thermal transport across solid interfaces with nanoscale imperfections: Effects of roughness, disorder, dislocations, and bonding on thermal boundary conductance. *ISRN Mechanical Engineering*, 2013:682586, 2013.

[192] R. J. Stoner and H. J. Maris. Kapitza conductance and heat flow between solids at temperatures from 50 to 300K. *Phys. Rev. B*, 48:16373–16387, 1993.

[193] R. C. Zeller and R. O. Pohl. Thermal conductivity and specific heat of noncrystalline solids. *Physical Review B*, 4:2029–2041, 1971.

[194] R. A. Richardson, S. D. Peacor, C. Uher, and F. Nori. YBa2Cu3O7-δ films: Calculation of the thermal conductivity and phonon mean free path. *Journal of Applied Physics*, 72(10):4788–4791, 1992.

[195] X. Liu, J. L. Feldman, D. G. Cahill, R. S. Crandall, N. Bernstein, D. M. Photiadis, M. J. Mehl, and D. A. Papaconstantopoulos. High thermal conductivity of a hydrogenated amorphous silicon film. *Physical Review Letters*, 102:035901, 2009.

[196] M. E. Siemens, Q. Li, R. Yang, K. A. Nelson, E. H. Anderson, M. M. Murnane, and H. C. Kapteyn. Quasi-ballistic thermal transport from nanoscale interfaces observed using ultrafast coherent soft x-ray beams. *Nature Materials*, 9(1):26–30, 2010.

[197] W. Sun, H. Liu, W. Gong, L. Peng, and S. Xu. Unexpected size effect in the thermopower of thin-film stripes. *Journal of Applied Physics*, 110(8):083709, 2011.

[198] P. Zolotavin, C. I. Evans, and D. Natelson. Substantial local variation of the seebeck coefficient in gold nanowires. *Nanoscale*, 9:9160–9166, 2017.

[199] J. Bass. CPP magnetoresistance of magnetic multilayers: A critical review. *Journal of Magnetism and Magnetic Materials*, 408:244–320, 2016.

[200] A. C. Reilly, W. Park, R. Slater, B. Ouaglal, R. Loloee, W. P. Pratt, and J. Bass. Perpendicular giant magnetoresistance of $Co_{91}Fe_9$/Cu exchange-biased

spin-valves: further evidence for a unified picture. *Journal of Magnetism and Magnetic Materials*, 195(2):269–274, 1999.

[201] L. Berger. Spin relaxation in metallic ferromagnets. *Physical Review B*, 83: 054410, 2011.

[202] D. Bozec, M. A. Howson, B. J. Hickey, S. Shatz, N. Wiser, E. Y. Tsymbal, and D. G. Pettifor. Mean free path effects on the current perpendicular to the plane magnetoresistance of magnetic multilayers. *Physical Review Letters*, 85: 1314–1317, 2000.

[203] A. C. Reilly, W. Chiang, W. Park, S. Y. Hsu, R. Loloee, S. Steenwyk, W. P. Pratt, and J. Bass. Giant magnetoresistance of current-perpendicular exchange-biased spin-valves of Co/Cu. *IEEE Transactions on Magnetics*, 34(4):939–941, 1998.

[204] L. Piraux, S. Dubois, and A. Fert. Perpendicular giant magnetoresistance in magnetic multilayered nanowires. *Journal of Magnetism and Magnetic Materials*, 159(3):287–292, 1996.

[205] D. Tian, Y. Li, D. Qu, S. Y. Huang, Xiaofeng Jin, and C. L. Chien. Manipulation of pure spin current in ferromagnetic metals independent of magnetization. *Physical Review B*, 94:020403, 2016.

[206] Y. Li, W. Cao, and W. E. Bailey. Characterization of spin relaxation anisotropy in Co using spin pumping. *Physical Review B*, 94:174439, 2016.

[207] K. Ko and G. Choi. Optical method of determining the spin diffusion length of ferromagnetic metals. *Journal of Magnetism and Magnetic Materials*, 510: 166945, 2020.

[208] N. Artunc and Z. Z. Ozturk. Influence of grain-boundary and surface scattering on the electrical resistivity of single-layered thin copper films. *Journal of Physics: Condensed Matter*, 5(5):559–566, 1993.

[209] M. Nguyen, D. C. Ralph, and R. A. Buhrman. Spin torque study of the spin hall conductivity and spin diffusion length in platinum thin films with varying resistivity. *Physical Review Letters*, 116, 2016.

[210] A. Asami, H. An, A. Musha, T. Gao, M. Kuroda, and K. Ando. Spin absorption at a ferromagnetic-metal/platinum-oxide interface. *Physical Review B*, 99:024432, 2019.

[211] M. Isasa, E. Villamor, L. E. Hueso, M. Gradhand, and F. Casanova. Temperature dependence of spin diffusion length and spin hall angle in Au and Pt. *Physical Review B*, 91:024402, 2015.

[212] E. Sagasta, Y. Omori, S. Vélez, R. Llopis, C. Tollan, A. Chuvilin, L. E. Hueso, M. Gradhand, Y. Otani, and F. Casanova. Unveiling the mechanisms of the spin hall effect in Ta. *Physical Review B*, 98:060410, 2018.